# MATRIX-ASSISTED LASER DESORPTION/IONISATION COLLISIONS OF BIO-MOLECULES

Anastassios E. Giannakopulos

*Submitted for the qualification of Doctor of Philosophy*

University of Warwick

Department of Chemistry

August 1994

## Contents

## Chapter 3 : Instrumentation, ion optical calculations and experimental design

## Chapter 4 : Energy-resolved time-of-flight mass spectrometry



## Chapter 5 : Charge exchange in large ions

## LIST OF FIGURES

**Acknowledgements**

I would like to thank my academic supervisor Professor Peter Derrick, for his guidance and assistance throughout the course of this work.

For his practical help in the design of the mechanical parts developed during this study and for suggestions and solving numerous problems with the experiment, many thanks to Alex Colburn.

Dr. Dominic Chan, Dr. Desmond Yau, Dr. David Reynolds, Dr Caroline Bradley, Dr Su Chen, Emmanuel Raptakis, Jonathan Haywood, Helen Cooper, Elaine Scrivener and Dr. John Christie have been good companions inspiring helpful discussions.

Many thanks to the University of Warwick for the financial support during part of the work presented in this thesis.

Thanks also to the members of the University mechanical workshop for their constant help and their willingness in solving various problems.

My family and friends have been a constant source of support throughout my research. I particularly wish to thank my parents for their continuous encouragement throughout my education.

## Declaration

I hereby declare that this thesis is my own work and that, to the best of my knowledge and belief, it contains no material previously published or written by another person, nor material which to a substantial extent has been accepted for the award of any other degree or diploma of a university or of other institute of higher learning, except where due acknowledgement is made in the text.

Anastassios E. Giannakopulos

*We shall not cease from exploration*
*And the end of all our exploring*
*Will be to arrive where we started*
*And know the place for the first time.*

T. S. Eliot, "Four Quartets"

## ABBREVIATIONS

| | |
|---|---|
| Å | Angstrom |
| $\alpha$ | "over relaxation parameter" |
| $\alpha_e$ | mean circular radius |
| $A^*$ | energised molecule |
| $A^{\neq}$ | activated complex |
| B | magnetic induction |
| BE | magnetic sector -electrostatic sector mass analyser |
| $\beta$ | velocity spread |
| CID | collision induced dissociation |
| CW | continuous wave |
| CMCE | centre-of-mass collision energy |
| $\gamma$ | mass spread |
| DAC | digital to analog conversion |
| Da | Daltons |
| deg. | degree |
| DHB | 2,5-dihydroxybenzoic acid |
| $\delta_k$ | small difference in kinetic energy |
| $\Delta t$ | difference in time |
| E | electric field strength |
| $E^*$ | non-fixed energy |
| $E_v^*$ | vibrational non-fixed energy |
| $E_r^*$ | rotational non-fixed energy |
| $E_o$ | critical value for classical reaction |
| EB | electrostatic-magnetic sector mass analyser |
| $E_{lab}$ | laboratory frame kinetic energy |
| $E_{cm}$ | centre-of-mass kinetic energy |

| | |
|---|---|
| ER-TOF | energy resolved time-of-flight |
| ESA | electrostatic analyser |
| e | electron charge |
| eV | electron volts |
| F | force |
| FAB | fast atom bombardment |
| FD | field desorption |
| FT | Fourier transform |
| FT-ICR | Fourier transform ion cyclotron resonance |
| FT-MS | Fourier transform mass spectrometry |
| FWHM | full width at half maximum |
| $\phi_e$ | included angle at the electrostatic analyser |
| ICR | ion cyclotron resonance |
| ICT | impulse collision transfer |
| IFF | impulse focusing field |
| IR | infra red |
| IVR | intramolecular vibrational energy redistribution |
| k | Boltzmann constant |
| KD*P | potassium dieduterium phosphate |
| keV | kilo electron volt |
| $K_e$ | coefficient of velocity dispersion in a radial electric field |
| L | length of the field free region |
| $L$ | average distance between collisions |
| $l_e^*$ | distance from the exit boundary of the field to the point of focus |
| LD | laser desorption |
| LDI | laser desorption ionisation |
| LSIMS | liquid secondary ion mass spectrometry |

| | |
|---|---|
| $\lambda$ | mean number of collisions |
| M | molar |
| *M* | number of molecules per unit volume |
| MMM | the large scale reverse geometry mass spectrometer at Warwick university |
| $m_a$ | mass of atom |
| $m_f$ | mass of fragment |
| $m_g$ | mass of gas |
| $m_{ion}$ | mass of ion |
| $m_p$ | mass of precursor |
| MALDI | matrix-assisted laser desorption/ionisation |
| MCP | micro channel plates |
| MS | mass spectrometer |
| MS-I | first mass spectrometer of a tandem instrument |
| MS-II | second mass spectrometer of a tandem instrument |
| MS/MS | tandem mass spectrometer |
| NBA | 3-nitrobenzyl alcohol |
| Nd:YAG | Neodymium:Yttrium Aluminium Garnet |
| PA | proton affinity |
| PAD | post acceleration detector |
| PD | plasma desorption |
| PEEK | polyetheretherketone |
| R | mass resolution |
| $R_0$ | residual of the difference equation |
| $r_e$ | zero potential surface in electrostatic analyser |
| RF | radio frequency |
| RRKM | Rice-Ramsperger-Kassel-Marcus |
| SIMS | secondary ion mass spectrometry |
| $\sigma$ | cross section |

| | |
|---|---|
| T | temperature in Kelvin |
| TI | thermospray ionisation |
| TOF | time-of-flight |
| TSER | time-selected energy resolved |
| UV | ultra violet |
| v | velocity of the ion |

## ABSTRACT

During this study the effect of electrostatic analysers on the time-of-flight of ions was studied theoretically, and it was shown that small energy spreads in the ion packet do not affect seriously the time-of-flight of an ion. The initial angle of an ion upon entering the electrostatic analyser does affect the time-of-flight of the ion. A C-shape configuration with two electrostatic analysers has been proposed as a solution eliminating time broadening due to spread in initial angle.

An energy resolved time-of-flight mass (ER-TOF) spectrometer was constructed. Metastable fragmentation and collision-induced dissociation experiments were carried out with different molecular-mass proteins and 3-nitrobenzyl alcohol as matrix. It has been shown that in matrix-assisted laser desorption/ionisation (MALDI) there is a substantial number of ions that decay after acceleration and prior to detection. The energy resolved time-of-flight spectra show that there is a peak broadening resulting from the lack of stability of the high-mass ions during their flight through a time-of-flight instrument.

The effect of the electric field above the target on the kinetic energy of the ions when 3-nitrobenzyl alcohol was used as matrix has been studied, and the energy spreads explained as being predominately energy deficits arising from the combination of high electrostatic fields, the liquid nature of the matrix and the inherent characteristics of the desorption / ionisation process.

Collision experiments with different molecular-mass proteins ranging from 3496 Da to 18300 Da and different collision gases over a wide range of kinetic energies showed that there is a decrease in the analyte signal with respect to the matrix signal for specific collision gases and collision energies. The ions were collected with an off-axis post acceleration detector. The decrease in the analyte signal has been explained as loss of the charge possessed by the analyte ion through charge exchange with the collision gas.

# CHAPTER 1

## INTRODUCTION

### 1.1 BACKGROUND TO MACROMOLECULES AND MASS SPECTROMETRY

The recognition and study of large molecules has been one of the great developments in chemistry in the last thirty years. In biochemistry, the importance of studies of proteins and nucleic acids continually increases, creating demand for new methods of determining accurate molecular masses and molecular structures. For many years when very small depressions of freezing points and small osmotic pressures were observed for particular colloidal solutions, now known to have contained macromolecules, chemists preferred either to regard these results as being due to formation of aggregates or to suppose that Raoult's and van't Hoff's law did not apply to colloidal solutions. The recognition that such substances exist intrinsically as giant molecules and can not have a simpler form came during the 1920's. Staudinger et al[1] pointed out that polymers such as poly-isoprene and natural rubber maintain their high molecular weight in all solvents, in contrast to dispersion colloids which are the result of physical association and which generally exist as such in selected solvents. The crystallisation of urease and pepsin by Sumner[2] and Northrop[3] respectively and the subsequent crystallisation of other proteins and the fact that the unit cell weight of a protein crystal was always a multiple of the molecular weight determined in solution and not some small fraction, were the two most important pieces of evidence in support of their macromolecular nature. Once

the existence of large molecules had been recognised, the need for new methods to study them became very apparent.

Mass spectrometry is a method used to measure the molecular masses of gaseous ions using electric and/or magnetic fields. The molecular mass can be deduced from the behaviour of the ion under the above fields and structural information concerning the ion can be obtained from the masses of fragments of the ion produced either directly as a result of ionisation or using various methods of excitation such as collisional activation and photodissociation. The first step in any mass spectrometric experiment is the production of gaseous ions. The formation of gas-phase ions from gaseous or volatile samples can be achieved with various methods. Some of these methods are electron bombardment, chemical ionisation[4,5] , field ionisation[6,7] and photoionisation[8,9]. Unfortunately most molecules with masses of more than some hundreds of Daltons are involatile with vapour pressures not sufficient to produce detectable ions with the above techniques. Such kinds of molecules are often also thermally labile, a fact which makes the desorption of intact large molecules even more difficult. In the last two decades, a number of desorption/ionisation techniques have been developed to transform these thermally labile and involatile substances from their liquid or solid phases into the gas phase. The most important of these techniques are field desorption(FD)[10,11] , thermospray ionisation(TI)[12], secondary ion mass spectrometry (SIMS)[13,14], fast atom bombardment (FAB)[15,16,17,18], plasma desorption (PD)[19,20], electrospray[21,22] and laser desorption (LD)[23,24].

Thermospray ionisation was developed by Vestal and coworkers[12], and was originally intended as an alternative means of rapidly vaporising involatile

analytes by heating the tip of a stainless steel tube through which the effluent from a liquid chromatograph flowed. The spray of vapours and droplets from the tube was directed against a heated probe to complete vaporisation of the droplets, and an electron beam from a hot filament bombarded the vapour. Later it was discovered that ions were produced even when the filament was not hot, which showed that the electron beam was not needed for thermospray ionisation. The explanation is that as the droplets become smaller through evaporation, appreciable electric fields build up which lead to ionisation of the analyte. Minimal electronic excitation is expected, which might in turn be expected to lead to minimal fragmentation. Examination of the spectra produced by thermospray indicate that it is a "soft" ionisation technique.

Electrospray ionisation of proteins was introduced by Fenn and co-workers[21,22] . The basic principles involve spraying a solution from a capillary needle which is floated at a high potential. The droplets produced carry a net charge and are accelerated toward a nozzle plate at ground potential. As the droplets become smaller, the electric field strength builds and a free jet of multiply charged ions is formed. Electrospray ionisation has become enormously important in recent years in mass spectrometric analysis, and therefore a separate section (1.2) is given for more detailed explanation of the technique.

Fast atom bombardment (FAB) is a technique which was described by Barber et al[15,17,18] in 1981. Fast atom bombardment (FAB) is an offshoot of secondary ion mass spectrometry (SIMS). In FAB the surface of a liquid matrix containing the analyte molecules is bombarded with high-energy (keV) neutral atoms, rather than with fast (keV) ions as in secondary ion mass spectrometry (SIMS). The neutral gas, typically either argon or xenon, is ionised in an electric discharge and the ions are accelerated to 5-10 keV. Charge exchange between the

ions and the neutral atoms takes place in the high-pressure region of the ion "gun". The original ions become neutral and continue on as a beam of fast atoms with almost the original kinetic energy. Ion deflectors eliminate any residual ions from the beam. After colliding with the matrix/analyte mixture, gaseous analyte ions are produced.

In field desorption (FD), non-volatile organic molecules are desorbed as ions from activated emitters under the influence of a strong electrostatic field[10,11]. The sample is loaded onto an emitter as a thin film. The emitters typically consist of 10 μm tungsten wires covered by carbon dendrites approximately 20-30 μm in length. The emitter is placed at 8-10 kV potential and heated. In the strong electric field, the ions are desorbed into the gas phase with little internal energy. Field desorption[25] is the method of choice for non-polar molecules such as polymers and hydrocarbons.

In plasma desorption (PD) the sample is deposited as a film on thin aluminised mylar and placed in the path of $^{252}Cf$ fission fragments[26] with MeV energies. The fission fragments enter from the back of the target to desorb both ions and neutrals from the sample. Typically several thousand fission fragments pass through the sample per second, each producing about 10 ions.

The upper limits of the mass ranges of the above ionisation methods are of the order of $10^3$ Da for fast atom bombardment(FAB), field desorption (FD), and laser desorption (LD), $10^4$ Da for plasma desorption (PD) and $10^5$ Da for matrix-assisted laser desorption/ionisation (MALDI) and electrospray ionisation.

## 1.2 ELECTROSPRAY IONISATION

The idea of using electrospray ionisation in mass spectrometry was put forward by Dole et al[27] in the 1960's. The significant development was made by Fenn and coworkers in Yale University in the 1980's. Many of the early applications of electrospray mass spectrometry took place in the group of Smith et al of Pacific Northwest Laboratories[28] and in Henion's group at Cornell University[29].

Electrospray ionisation mass spectrometry can be considered to take place in three steps.

### 1.2.1 Spray formation

The liquid which contains the analyte is sprayed from the tip of a hypodermic needle held at a few kV. The spray produces small highly charged droplets. To establish a stable spray in electrospray ionisation, it is important to control the influence of parameters such as solution composition, with regards to conductivity and surface tension, and liquid flow rate. Although the instrumentation used for spray formation is very simple, the production of the right kind of spray and a stable ion current is not so easy and the process involves a lot of trial and error in order to establish the right conditions for electrospray production.

### 1.2.2 Ion desorption in electrospray

There are two main mechanisms proposed about the formation of the analyte ion. One is that a single analyte molecule is present in a small droplet, which is the remains of an original droplet following evaporation. The other mechanism is that daughter droplets are produced by asymmetric Rayleigh division or hydrodynamic instability of an original droplet[30], which contained many analyte

molecules. The model according to which the small droplet is the remains of an original droplet following evaporation was proposed by Dole and co-workers. Field-induced ion evaporation from charged droplets has been discussed by Iribarne and Thomson[31]. When the size of a droplet reaches a certain radius the droplet may become disrupted due to Rayleigh instability[32]. Schemelzeisen-Redeker and co-workers[33] suggest that an electrohydrodynamic disintegration induced by the removal of an ion with part of its solvation sphere from the highly charged surface is also probable. As in other "soft ionisation" techniques, a large number of unknowns makes the development of a realistic model for electrospray difficult. The state of the droplet at the final stage when desorption occurs is not well known, and evaporation of the final droplets may proceed through "Coulombic explosions"[34] for which the mechanisms are not well understood. Another difficulty is that very little is known about the liquid-gas interface in strong electric fields especially when electrolyte is taken into consideration. The experience in Fenn's and other laboratories has been that preformed ions "work better" with electrospray[30]. Polar molecules work well, but non-polar molecules such as hydrocarbons do not. Large molecules seem to need at least one site with sufficient affinity for the charge carrier per 1000-2000 Da.

### 1.2.3 Mass spectrometric analysis with electrospray.

A great advantage of electrospray mass spectrometry is that the m/z range of the mass analyser need not to be large, because as a result of extensive multiple charging a range of m/z 2000 is often adequate. So far most work has been carried out on quadrupole mass spectrometers, which are relatively cheap and easy to use. The different numbers of charges appearing on the same molecule can make difficult the interpretation of the spectra of mixtures of compounds. Computer

software is very often employed for the interpretation of the spectra. Mixtures with broad distributions of masses can pose problems for interpretation in electrospray mass spectrometry, because the mass and the charge distribution have to be separated from each other. In such cases, other methods such as field desorption(FD) or matrix-assisted laser desorption/ionisation (MALDI) may be more adequate.

## 1.3 LASER DESORPTION

Since the 1960's lasers have been used to generate ions, including those of organic molecules, for analysis in mass spectrometers[35,36]. Considering the large variation in basic parameters, different results have been obtained from the different combinations of lasers and mass spectrometers. Researchers have used a variety of lasers with vastly different wavelengths, ranging from far-UV to far-IR, and pulse widths ranging from femtoseconds to continuous-wave (CW) irradiation. The different types of lasers have been combined with virtually every kind of mass spectrometer. Applications such as trace analysis of organic and inorganic samples and microprobe analysis with submicrometer-level spatial resolution have been performed.

The first systematic attempts to generate gaseous ions of organic molecules with lasers date back to the early 1970's. Efficient energy transfer to the sample requires resonant absorption by molecules at the laser wavelength. The electronic states of the molecules can be excited with lasers emitting in the UV, whereas the rotational and vibrational states can be excited by IR lasers. Lasers with pulse widths in the 1-100 ns range, such as Q-switched Nd:YAG , nitrogen or excimer lasers, have been extensively used, and it has been possible to avoid thermal decomposition of the thermally labile molecules. The short pulse-duration and

the ability to focus the laser beam to very small spot sizes has made the above lasers useful tools for time-of-flight mass spectrometry. Good time-resolution in time-of-flight instruments can be obtained, when the spatial and temporal spreads of the ion packet are small. The experiments with direct laser desorption revealed an upper limit to the size of molecules that could be desorbed as intact molecule-ions. Biopolymers of 1000 Da and synthetic polymers up to some thousand Da were desorbed with various laser parameters. When resonant desorption is used, the wavelength is selected precisely and a certain amount of energy should be deposited into the molecule. Less well-controlled energy transfer delivers energy into photodissociation channels, breaking the molecule into smaller pieces. In non-resonant multiphoton experiments, the photon density needed for efficient ionisation is high and the necessary irradiances can be close to plasma generation conditions which would destroy large organic molecules.

### 1.3.1 Matrix-assisted laser desorption/ionisation

Many different types of sample preparation have been used in laser desorption, but until 1987 laser desorption was not regarded by the analytical community as a viable technique for examining high molecular-mass molecules. Until the discovery by Tanaka et al[37] of the effective use of a matrix, laser desorption had an upper mass-limit of approximately 1000 Da. The laser used in the experiments of Tanaka et al was a nitrogen laser (337 nm), but it was the sample preparation method which was the key to the new technique. The polypeptide of interest was dissolved in glycerol and the glycerol solution was mixed with a finely divided metal powder. A droplet of this solution was irradiated with the laser and the ions were analysed with a reflectron time-of-flight mass spectrometer. The

glycerol was totally transparent to the wavelength used and the light was absorbed by the metal powder. The ultra-fine metal powder has high photo-absorption, low heat capacity and extremely large surface area per unit volume. Spectra of lysozyme obtained by Tanaka et al show the singly- and doubly-charged cluster ions of lysozyme. A metal particle that has dimensions smaller than the wavelength of the irradiating laser is heated by currents induced by the rapidly varying and spatially coherent electric field of the laser light. Because of their ability to produce thermal excitation in response to laser irradiation, the metal particles are the coupling between the light and the liquid matrix. The connection between the heating of the metal particles and the ejection of intact protein ions has not been established. The method of sample preparation explored by Karas and Hillenkamp was conceptually different. They believed that it was the substrate under a layer of organic material on the surface that absorbed the light and not the organic molecules themselves. In 1985, Hillenkamp et al began to publish papers[38,39] containing the hypothesis that large molecule ions could be produced by mixing the analyte with a matrix material that was chosen for its ability to absorb the laser light. This matrix material would absorb the light, resulting in its ablation and hopefully in a coupled ablation of analyte molecule ions. The intimate role of the matrix in driving the desorption process has led to the proposed name "matrix assisted laser desorption".

The breakthrough for matrix-assisted laser desorption as applied to biochemical samples came with the discovery that nicotinic acid had special properties for large polypeptide analytes[40]. The wavelength used was 266 nm, generated as the fourth harmonic of a Q-switched Nd:YAG laser. Nicotinic acid is a solid at room temperature, with low vapour pressure and a high absorption coefficient at 266 nm. When aqueous solutions of a protein and nicotinic acid were mixed and a

droplet of this mixture was dried, the deposit gave large signals of protein molecule ions in a reflectron time-of-flight mass spectrometer when the sample was irradiated. The major difference between the results of the Tanaka method of sample preparation and those of the Hillenkamp-Karas method was sensitivity. Tanaka's method required nanomoles of protein sample, while the Hillenkamp-Karas method required picomoles. The signals obtained with the latter method had also a higher signal-to-noise ratio.

Most of the work to date in matrix-assisted laser desorption/ionisation studies has been concerned with the method proposed by Hillenkamp et al in 1988, in which organic molecules are used as matrices. Typically, analyte of concentration $10^{-5}$ M, is mixed with 1000 to 10000 molar excess of matrix in solution. A few microliters of the matrix-analyte solution are dried on to a metal target before being introduced in to the mass spectrometer. Studies have shown that matrix to analyte ratios ranging from a few hundreds to a few hundred thousands can be used[41]. The signal-to-noise ratios of matrix spectra generated with MALDI have been found to be high, and sensitivities are high as well. Femtomole-level sample loadings can give clear molecule-ion signals with MALDI[42]. Depending on the matrix material, different amounts of contaminants can be tolerated. Salts, detergent or buffer concentrations in the millimolar range do not significantly reduce the quality of the spectra[43,44]. Matrix-assisted laser desorption/ionisation spectra of proteins generally consist of two regions, the analyte region and the matrix region which very often appears very strong. The matrix signal is comprised of molecule ions, fragments and higher-mass ions formed from photochemical reactions. The analyte region signals comprise molecule ions and sometimes singly and doubly charged analyte ions. When the concentration of the analyte is high, high-mass cluster ions can be also observed.

With the correct sample preparation and the laser energy set to threshold energy for analyte-ion production, a near-elimination of the low-mass ion peaks can be achieved by using certain matrices such as nicotinic acid[45,46] and 2,5-dihydroxybenzoic acid[47,48]. The relative intensities of the molecule-ion signals of different charge states depend on the nature of the matrix and analyte molecules. Generally the intensities of the multiply charged ions increase with the mass of the analyte molecule. Adduct ions of low intensities are observed as satellite peaks. The adduct peaks are caused by salts or by small fragments of the matrix. The chemical adduction has been found to increase with increase in the mass of the ion. The adduct formation can also explain the broadening of the ion peak at high masses, when the adduct peaks can not be resolved from the molecule-ion peak.

### 1.3.2 Matrices

Reviewing the matrices that have been discovered, some common qualities can be identified. Certain conditions should be met, in order to identify a compound as a good candidate as a matrix for MALDI. These conditions are the solubility of the matrix in the appropriate solvents, the absorption spectrum of the matrix, the reactivity of the matrix and the sublimation rate in vacuo.

Solubility is necessary so that the protein and the matrix material can be dissolved in the same solution. Solvent systems for proteins are acidified water, water:acetonitrile mixtures, water:alcohol mixtures and 70% formic acid.

Absorption allows the energy to be deposited in the matrix and not the analyte. The value of this parameter is not as easily obtained as might be imagined. The absorption coefficient of a material in solution is easily measured,

but it is much more difficult to measure accurately the absorption coefficient for a solid used in matrix-assisted laser desorption. The absorption curves for most compounds are red-shifted to some extent in the solid phase (compared to their solution values), but the extent of that shift varies from one compound to another. Using the solution absorption coefficients as a guide, the range of values for the better matrices at the appropriate laser wavelengths is very restricted, and in practice has limited the choice of matrices to aromatic compounds with electron-withdrawing groups on the ring.

The third condition, namely absence of reactivity, is required for obtaining useful analytical results. Matrices that covalently modify proteins or other analytes cannot be used. Oxidising agents must be avoided with proteins, because of the lability of disulphide bonds and the tendency of cysteine groups and methionine groups to oxidise[49]. The N-terminal amino group of a protein and ε-amino groups of lysines are very susceptible to modifications, such as Schiff base or amide formation. Aldehydes cannot be used for this reason. Nicotinic acid which was used extensively in early experiments is no longer widely used, because of undesirable photochemical reactions producing numerous satellite peaks in the mass spectrum[44].

Low sublimation rates are required for both liquid and solid matrices, for various reasons. The sample should be able to remain under vacuum for several minutes without considerable changes to the ratio of matrix to analyte. It has been observed that for certain matrices there is a fine balance in the matrix-to-analyte molar ratio in order to obtain good quality spectra[45,46]. The ratio of matrix-to-analyte molecules should not change during the analysis of the sample, as this would lead to inconsistencies in the intensities of the ion signals.

If a candidate matrix has passed these requirements, it is still necessary to test the material in a laser desorption mass spectrometer. Most of the materials that meet the criteria do not produce analyte ions.

The first successful MALDI spectra of proteins were recorded by Karas and Hillenkamp using nicotinic acid matrix and the laser source was a frequency quadrupled Nd:YAG laser irradiating at 266 nm. A number of new matrices were introduced by Beavis and Chait[44] in 1989, mainly aromatic carboxylic acids, such as 2-pyrazinecarboxylic acid and 4-hydroxy-3-methoxybenzoic acid (vanillic acid). Other compounds were also observed to give strong molecule-ion signals from proteins. Beavis and Chait[50] later introduced several derivatives of cinnamic acid, such as 3,4 dihydroxycinnamic acid (cafeic acid), 3-methoxy-4-hydroxy cinnamic acid ( ferulic acid) and 3,5-dimethoxy-4-hydroxy cinnamic acid (sinapic acid).

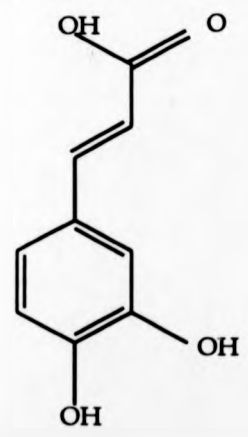


3,4-dihydroxy cinnamic acid

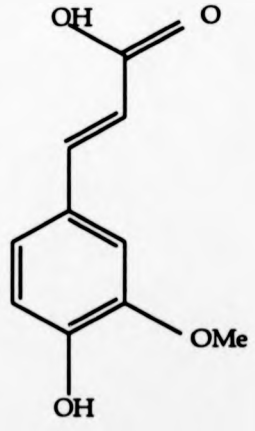


3-methoxy-4-hydroxy cinnamic acid

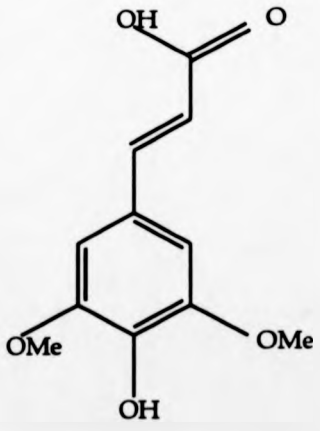


3,5-dimethoxy-4-hydroxy cinnamic acid

These matrices gave improved sensitivities and somehow reduced the formation of adduct ions. Cinnamic acid derivatives, of higher molecular

masses, permitted more accurate molecular-mass measurements of proteins below 30 kDa, because the photoadduct ions could more easily be resolved from the $[M+H]^+$ ion of the analyte. Cinnamic acid derivatives work at least as well at the third harmonic of the Nd:YAG (355 nm) as they do at the fourth harmonic (266 nm). Thus the use of the cheaper and simpler nitrogen laser emitting at 337 nm became of common use.

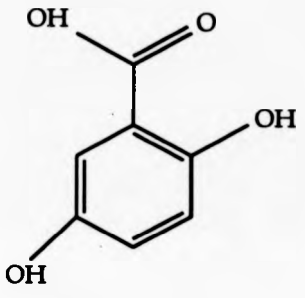


2,5-dihydroxybenzoic acid

The introduction of 2,5-dihydroxybenzoic acid (DHB) by Karas and co-workers[47] was a further important step in matrix development. This matrix, which is useful at 337 and 355 nm, offers very good sensitivity for peptides and small proteins. With DHB as matrix, very good results have also been observed for carbohydrates[51] and glycolipids[52], in addition DHB is an excellent choice for profiling enzymatic digests[53]. With the introduction of the use of IR lasers by the Munster group [54,55], the range of possible matrix compounds was extended to the large class of materials containing OH or $NH_2$ groups which absorb at approximately 3 μm.

The most commonly used matrices currently are ferulic acid[50] , sinapic acid[50], gentistic acid[56], 2,5-dihydroxybenzoic acid (DHB) and α-cyano-4-hydroxycinnamic acid[57]. These materials can be used with protein samples containing buffers and many other types of common contaminants. The qualities that separate most matrix candidates from the few that work well are obscure. It can be imagined that the matrix must have some special affinity for proteins that allows them to be incorporated into the solid matrix material during the drying process. Such an interaction is difficult to measure and even more difficult to predict. Closely related compounds, for example, 3-hydroxycinnamic acid (meta-coumaric acid) and 4-hydroxycinnamic acid (para-coumaric acid), have very different properties as matrices. These compounds have very similar solubilities and absorption spectra, but only para-coumaric acid is a good protein matrix. Picolinic acid (2-pyridinecarboxylic acid) is a very poor matrix, while nicotinic acid has good properties. Attempts have been made to correlate microscopic observations of the deposit with the efficiency of the matrix[58]. Additional factors that may affect the performance of a matrix material are its volatility and its photostability.

A parameter that has been proven to be less critical is the wavelength of the laser light. Many different pulsed UV lasers have been used to produce protein ions. The main constraint on the laser wavelength is the absorption properties of the matrix. The matrix must absorb on the frequency emitted by the laser. Secondarily the analyte should be transparent to the light, so that unwanted photochemical reactions are not produced by the irradiation. For proteins, absorption in the amino acid sidechains becomes important below 270 nm. Proteins that contain covalently attached chromophores(e.g. the heme group in cytochrome C) may require longer wavelengths to avoid absorption.

Matrices, formed by combining two or more compounds and which can have properties that can be adjusted for specific experimental conditions, have also been investigated by various workers. Recent work from Hillenkamp et al has shown that, for 2,3-dihydroxybenzoic acid, the MALDI performance in the high-mass region (>50 kDa ) is improved when the matrix is combined with a structurally similar compound, presumably by lowering the energy required to disrupt the crystal lattice[59]. Cornett et al[60] have showed that 532 nm radiation can be efficiently coupled into the liquid matrix 3-nitrobenzyl alcohol by preparing mixtures with the strongly adsorbing laser dye rhodamine 6G.

## 1.4 MASS SPECTROMETRIC TECHNIQUES

### 1.4.1 Sector instruments

**1.4.1.1 Electrostatic analysers.** By placing voltages on a pair of concentric electrodes a beam of ions fired into the entrance of the electrostatic analyser can be made to follow a circular trajectory by balancing the centrifugal force due to the motion of the particle against the electrostatic force exerted by the radial electric field. The radius of curvature of the flight path is given by the following equation:

$$r = \frac{2V}{E}$$ where V= accelerating potential

E= electric field strength

Ion sources produce ion beams with inherent energy spreads. The electrostatic analyser acts effectively as an energy filter, and in the early days of mass spectrometry it was used as such in order to provide a monoenergetic beam. The common use of the electrostatic analyser nowadays is as one of the sectors in double focusing mass spectrometers.

1.4.1.2 **Magnetic sector analysers.** A flight tube is placed between the poles of a magnet. The ion beam generated in the ion source is aimed through the flight tube and hence through the magnetic field. The ions are forced to follow a curved trajectory. The radius of curvature depends upon the velocity of the ion and the strength of the magnetic field. Force F is exerted on the ions when they enter a magnetic field B. The force is orthogonal to the lines of the magnetic field.

$$F = Bzv$$

where B= magnetic induction
z= charge of ion
v= velocity of the ion

Ions will describe a circular trajectory of radius r, where

$$r = \frac{mv}{Bz}$$

or $$\frac{m}{z} = \frac{Br}{v}$$

If all the ions in this beam have the same kinetic energy where $v = \sqrt{\frac{2zV}{m}}$ and where V is the potential used for the acceleration of the ions, the m/z ratio can now be described as $\frac{m}{z} = \frac{B^2r^2}{2V}$

The magnetic sector is not a mass analyser. It is a momentum analyser. The deflection of the ions to different trajectories is a function of the mass and the velocity of the ion. Typical magnetic field strengths used in conventional magnetic sector mass spectrometers range from 1000 to 10000 gauss.

### 1.4.1.3 Double-focusing mass spectrometer

The double-focusing mass spectrometer[61] consists of an electric and a magnetic sector in series. The electrostatic analyser acts as an energy analyser and also as a lens for ions of the same energy. If a very narrow beam of ions with the same m/z but different energies and no angular divergence enters the electric field of a radial electrostatic analyser, it undergoes velocity dispersion. If this diverging beam is allowed to enter a homogenous magnetic field, the ions with the same m/z but different energy can be made to recombine at a single point after emerging from the magnetic field ( figure 1.4.1.3.(1) ). This point is the point of velocity focusing. If the initial ion beam contains different masses then the ions will undergo mass analysis by the magnetic field. The location of the points, where different masses are velocity focused, lies on a curve which is called the velocity focusing curve.

If now an initial monoenergetic beam of ions with the same m/z but with small angular divergence enters a radial electrostatic field, it is brought to a focus after

**Figure 1.4.1.3.(1)** Velocity focusing by a combination of electrostatic and magnetic sector fields of a collimated beam of ions with the same m/z but different kinetic energies.

emerging from the electrostatic field. When these ions are allowed to enter a homogenous magnetic field, they can be brought again to a directional focus after emerging from the magnetic field( **figure 1.4.1.3.(2)** ). If the beam consists of ions of different masses, the ions undergo mass analysis and all the directionally focused masses lie in different points on the direction focusing curve.

For a beam of ions of the same m/z with a small angular divergence and a small energy spread entering a radial electrostatic field, there are direction focusing points for ions of different velocities. These direction focusing points for ions of different velocities lie at the same distance from the exit boundary of the electrostatic field but are laterally displaced from one another. After entering the homogenous magnetic field, the ions will be velocity focused on a point on the velocity curve and directionally focused on a point on the direction focusing curve. When ions with different m/z, a small energy dispersion and a small angular dispersion are used, the magnetic field will offer mass separation. For every different mass the velocity focusing point and the directional focusing point will be two different points, which will lie on the velocity focusing curve and the direction focusing curve respectively. With a suitable combination of the electrostatic and magnetic fields, the two curves can be made to intersect or even overlap over extended regions.

Several different geometries of double-focusing mass spectrometers have been described with one of the most commonly used being the standard Nier-Johnston geometry, where the electrostatic analyser (ESA) is located between the ion source and the magnetic sector. The reverse geometry places the magnetic sector between the ion source and the ESA, and presents some advantages for special types of experiments such as the mass-analysed ion kinetic energy (MIKE) experiment.

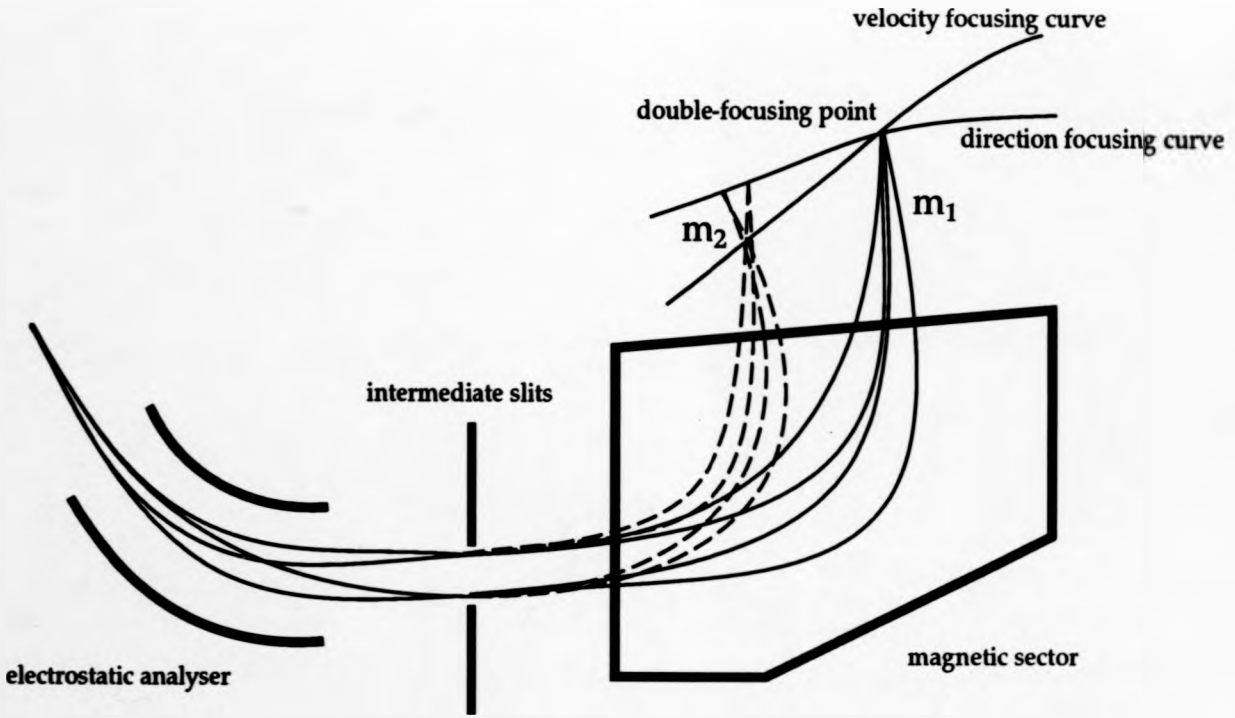


**Figure 1.4.1.3.(2)** Schematic diagram of a double-focusing apparatus. For a beam of ions of the same m/z with a small angular divergence and a small energy spread, the position of the velocity focusing will be in different points for directionally focused ions.

### 1.4.2 Fourier transform ion cyclotron resonance (FT-ICR) mass spectrometer

The fourier transform ion cyclotron resonance (FT-ICR) mass spectrometer uses the principles of an ion cyclotron resonance (ICR) experiment to make mass measurements[62].

The basic concepts of FT were developed many years ago, because the idea of ion cyclotron resonance was introduced by Lawrence in the 1930's for use as a charged particle accelerator. Ions are constrained to move in a circular orbit by a strong homogenous magnetic field. The frequency of the circular motion w is equal to qB/m, where B is the magnetic field strength and q/m is the charge-to-mass ratio. Fourier transform mass spectrometry (FT-MS) was first demonstrated in 1974 by Comisarow and Marshall[63,64]. They called their method fourier transform ion cyclotron resonance (FT-ICR), given the relationship to the ion cyclotron resonance technique already widely used to study ion molecule reactions in the gas phase[65]. The fourier transform method retains all the capabilities of the ICR, but it has the advantage of being able to acquire a mass spectrum much faster. All ions are accelerated and detected at the same time. Fourier transform is different from other mass spectrometric techniques, because it detects the image current induced by the coherent cyclotron motion of ions stored in the analyser cell.

The fourier transform mass spectrometer (FT-MS) requires a fast computer for the fourier transformations. Most of the technology is similar to that used in fourier transform nuclear magnetic resonance experiments. The main advantages of fourier transform mass spectrometry are the high resolution and fast scan rates.

### 1.4.3 Ion trap mass spectrometer

The ion trap was first described by Paul[66] and it has been used since then for the storage and mass analysis of ions. The device (**figure 1.4.3.(1)** ) consists of a chamber formed by two hyperbolic surfaces and a central ring electrode. Potentials corresponding to radio frequencies are applied to the ring electrode. Under specific conditions certain ions have stable trajectories within the chamber and can be trapped for many seconds. The stability of motion of an ion within the trap is determined by a parameter proportional to the radio frequency (RF) potential applied to the ring electrode and the m/z ratio of the ion. As the radio frequency (RF) potential value increases, ions with greater m/z develop unstable trajectories and are ejected through a small hole on one of the hyperbolic electrodes and are detected with an electron multiplier. The resolution and sensitivity are increased when a buffer gas (millitorr pressures) is used. The buffer gas damps the motion of the ions causing them to oscillate closer to the centre of the ion trap where the electric field is more homogeneous.

### 1.4.4 Time-of-flight mass spectrometry of large ions with matrix-assisted laser desorption/ionisation (MALDI).

#### 1.4.4.1 Background

The mass of an ion can be measured by using its velocity to determine the mass-to-charge ratio (m/z). In a time-of-flight (TOF) spectrometer, the ions are accelerated to a fixed kinetic energy by an electrostatic field. The velocity of the ions will then be propotional to $(m/z)^{-1/2}$, where m/z is the mass-to-charge ratio of a particular ion species. The ions are allowed to fly through a field-free region, where they separate into a series of spatially discrete packets, each travelling with

**Figure 1.4.3.(1)** Ion trap electrodes shown in cross section. An RF field is applied between the two end caps and the ring electrode.

a velocity characteristic of their mass-to-charge. The time-of-flight through the field free region is given by:

$$t = L\sqrt{\frac{m}{2qeV}}$$

L is the length of the field-free region, q is the number of charges of the ion, e is the electronic charge and V is the accelerating potential. A recording of the detector signal as a function of time is a TOF mass spectrum. The difference between the start time, common to all ions, and the arrival time at the detector, characteristic of each ion, can be used to calculate the ion's mass. Such a calculation can be used to convert the time axis of the spectrum into a mass-to-charge ratio axis. This simple, linear time-of-flight configuration was first used for large-molecule mass spectrometry by MacFarlane and Torgerson[67], with a plasma desorption ion source. Many investigators have used similar configurations with a variety of electrode configurations, ion sources and detectors. The accelerating potentials are usually between 1 and 30 kV with positive or negative polarity, and the flight path lengths range from some centimetres to a few meters.

There are three basic parameters defining the performance of a time-of-flight configuration.

(i) Mass resolution $m/\Delta m$ is a measure of an instrument's capability to produce separate signals from ions of similar masses. It can be expressed as the mass of a given ion signal divided by the full width of the signal $\Delta m$. In time-of-flight instruments, the mass resolution depends on the time resolution and can be defined as $t/(2\Delta t)$. In this definition of resolution, t is the total time of flight of

an ion of a specific mass/charge, and $\Delta t$ is the full time-width of the ion packet at half-maximum intensity. In linear time-of-flight mass spectrometers, the upper limit on resolution is imposed by experimental factors such as initial energy distribution, delayed ion formation and finite frequency response of the detector and associated signal processing electronics. The initial energy distribution of the ion packet can be influenced by space charge effects when the numbers of ions produced during ionisation are high, or can arise when ions are produced in a spatially not well defined region of the ion source. Another form of energy distribution can arise from the desorption process itself.

(ii) Mass accuracy is a measure of the error involved in assigning a mass to a given ion signal. It is expressed as the ratio of mass assignment error divided by the mass of the ion and is frequently quoted as a percentage. Space charge effects again can play a significant role in the accuracy of mass assignment in time-of-flight, as they tend to produce asymmetrical ion peaks and as a result make the accurate positioning of the mass peak difficult. During the desorption/ionisation process in MALDI, a large number of ions, most of them being matrix ions, are concentrated in a well-defined volume. As the ions are accelerated, analyte ions are left behind because of their high molecular masses. As a result different molecular-mass molecules experience different space-charge fields, making the accurate mass determination even more difficult. The solution could be lower laser irradiance and low sample concentrations. Another factor making accurate mass-determination difficult in MALDI is the low mass-resolution offered by time-of-flight instruments for high molecular-mass molecules, given the broad isotopic envelope and the extensive adduct formation.

(iii) Sensitivity is the ability to give mass spectrometric information with very small amounts of sample. There are three main factors affecting the sensitivity of an instrument.

(a) One factor is the ability of the desorption and ionisation technique used to produce a large number of gas-phase ions. It is a subject to which lot of effort has been devoted for decades, and astonishing results have been produced during the last ten to twenty years.

(b) The second factor is the ability of the mass spectrometer to give mass and structural information when small numbers of ions are used.

(c) The ability of the detector to detect efficiently the ions produced.

#### 1.4.4.2 Resolution in time-of-flight mass spectrometers

If an ion's flight time depended only on its mass-to-charge ratio, the TOF mass spectrometer (MS) would have unlimited resolution. In fact, an ion's time-of-flight depends on a number of factors besides the mass-to-charge ratio.

Space-charge effects affect the resolution, appearing as an increased initial velocity spread due to the coulombic repulsions between charged ions. These effects can be decreased by using low laser powers or low sample pressures. The use of high-frequency pulse-counting techniques can extend the resolution of the detection signal processing electronics to the picosecond regime. Under normal experimental conditions, the variation in ion flight-time is dominated by the initial ion velocity and spatial distribution of ion formation. Molecule ions with the same m/z ratio are formed in the source with an initial velocity distribution resulting from the neutral precursors. Under normal experimental conditions

this distribution is Maxwellian in nature. This distribution is a one-dimensional normal distribution with a mean of zero and a standard deviation given by $(kT/m)^{1/2}$, where m is the mass of the atom or molecule, T is the absolute temperature and k is Boltzmann's constant.

Another source of energy spread is the production of ions not in a point in space but in a finite spatial volume. Ions formed at different positions are accelerated to different final kinetic energies. The ionisation over a finite spatial volume can result from the finite dimensions of the laser beam and from the possible delay in ion formation after the desorption.

Over the past few decades many methods have been proposed to increase the mass resolution in TOF mass spectrometry by compensating for these initial variations in ion velocity and position. Wiley and McLaren[68] introduced the two-step acceleration time-of-flight mass spectrometer, a space focusing condition that makes flight time independent of initial position to a first order. Further improvement to the time resolution of the time-of-flight instruments with the basic Wiley and McLaren configuration came with the impulse-field focusing (IFF), which involves the application of a time-dependent ion-drawout field as opposed to time-independent fields employed in conventional TOF spectrometers[69,70]. Post-source pulse focusing[71,72] is another procedure for mass-resolution enhancement, where an electric field pulse is applied to a short region containing the ions after they have been accelerated. The trailing ions of the same ion-mass packet will be accelerated slightly more than the leading ions and eventually catch up. The combination of electric or magnetic sectors with linear drift regions has also led to increased resolution[73,74,75]. Finally, a reflectron TOF MS was introduced by Mamyrin et al[76] and was later used by Boesl et al [77] with a laser ionisation ion source. In reflectron time-of-flight instruments, the ion's

flight time becomes independent of energy differences by using a homogenous electrostatic retarding field. An arbitrary ion of mass m, kinetic energy K and charge q can be described relative to a reference ion of mass $m_o$, kinetic energy $K_o$ and charge $q_o$ as:

$$\frac{K}{q} = \frac{K_o}{q_o}(1+\delta_k) \text{ and } \frac{m}{q} = \frac{m_o}{q_o}(1+\delta_m)$$

In a reflectron TOF MS (**Figure 1.4.4.2.(1)**), a field of strength $E_o$ is applied behind a field-free region of length $l_1$. Ions of energies $K_o$ and K will penetrate into this field to a depth $l_o=K_o/E_o$ and $l=K/E_o$ respectively before they turn around. The ions under consideration have then moved over distances $2(l_1+l_o)$ or $2(l_1+l)$ with flight times of $T_{o1}=2(l_1+2l_o)/u_o$ or $T_1=2(l_1+2l)/u$ where the factor of two results from the linearity of the electrostatic field. For an ion of mass m and energy $K_o(1+\delta_k)$ the calculated flight time is:

$$T_t = \frac{2\sqrt{\frac{m}{m_o}}}{u_o\sqrt{1+\delta_k}}\left[l_1 + 2\frac{K_o}{E_o}(1+\delta_k)\right] =$$

$$= \frac{2}{u_o}\sqrt{\frac{m}{m_o}}\left[\left(l_1 + 2\frac{K_o}{E_o}\right) + \left(l_1 - 2\frac{K_o}{E_o}\right)\delta_k + \left(\frac{l_1}{6} - \frac{2K_o}{3E_o}\right)\delta_k^2 + \cdots\right]$$

Choosing $l_1=2K_o/E_o=2l_o$, the linear term in $\delta_k$ vanishes so that to the first order the ion flight times are independent of energy deviations. When choosing $l_1=4K_o/E_o=4l_o$ the quadratic term of $\delta_k$ vanishes. The ion flight times become independent of energy deviations to first and second order simultaneously,

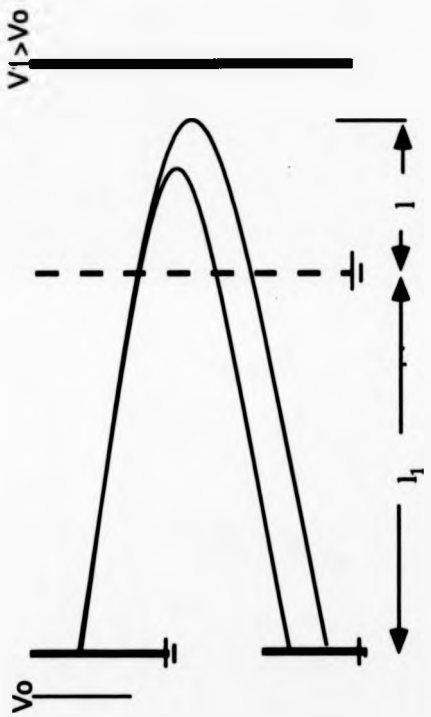


**Figure 1.4.4.2.(1)** By using a deflecting homogenous electrostatic field combined with a field-free region, equal arrival times for ions of equal mass-to-charge ratios but different velocities can be achieved.

when two retarding fields of different strengths are placed in series[78], or if especially designed grid-free retarding fields are used[79,80]. Using the above approach, mass resolutions of about 10000 has been achieved. In spite of the developments in time-of-flight mass spectrometry and the improvement in resolution, the early MALDI time-of-flight spectra suffered from very poor mass resolution. Resolution ($m/\Delta m$) at full width at half maximum (FWHM) of less than 100 was achieved for ions in the high-mass range, although ions in the low mass range could have much better resolution. The mass-dependent initial kinetic energy distributions[81] and the effect of adduct ion formation[82] were the reasons for the poor resolution. The detection process for the high-mass region ions also played an important role in the poor mass resolution. The large-ion to small-ion conversion phenomenon[83,84], at the surface of the conversion dynode upon the impact of high-mass ions, contributed to the low mass resolution.

## 1.5 TANDEM MASS SPECTROMETRY

For decades tandem mass spectrometers have been designed and used for fundamental studies in gas phase ion chemistry[85,86]. However the full potential of tandem mass spectrometry (MS/MS) has been recognised only in recent years, when it has been realised that this is a powerful technique for direct mixture-analysis.

In a tandem mass spectrometer primary ions of a given compound or a mixture of compounds are generated in the ion source. If the conventional electron impact ionisation is used, a large variety of fragment ions is produced. When "softer" ionisation methods are used, molecule ions are primarily formed. The primary ions are mass-selected at the first stage (MS-I) of the tandem mass

spectrometer. A given ion, after being selected by the first stage of the mass spectrometer (MS-I), can undergo secondary decomposition before entering the second stage of the mass spectrometer (MS-II), where mass analysis of these secondary ions is performed. Tandem mass spectrometry became a useful analytical tool for the structural determination of molecules after the introduction of the collision induced dissociation (CID) technique. The "low" (1-100 eV) and "high" (>100 eV) laboratory frame kinetic energy regions in collision-induced dissociation (CID) are usually treated separately. Conservation of energy and momentum in a collision requires that only a fraction of the laboratory frame kinetic energy $E_{lab}$ is available for the excitation of the ion[87]. This fraction is the collision energy ($E_{cm}$) in a coordinate system moving with the centre of mass of the collision partners and for a stationary target gas is:

$$E_{cm} = E_{lab} \frac{m_g}{(m_p + m_g)}$$

$m_p$ and $m_g$ are the mass of the ion and the neutral gas respectively.

The distinction between "low" and "high" energy CID becomes less marked when discussed in terms of centre-of-mass collision energy.

The unique features of double-focusing mass spectrometers allow the use of a number of different types of scans of the basic parameters of the instrument, in order to perform tandem mass spectrometry experiments[88] (MS/MS). In double-focusing magnetic deflection mass spectrometer, the three important parameters which control the type of mass spectrum recorded are V the accelerating voltage, E the electric sector field strength and B the magnetic sector field strength.

In a forward-geometry instrument where the electric sector precedes the magnetic sector, if $m_1^+$ decomposes to give $m_2^+$ in the field region between the two sectors, low intensity diffuse peaks are observed at an apparent mass $m^*$ where $m^* = m_2^2 / m_1$. Such peaks are absent in a reverse-geometry instrument. Alternative methods of scanning V, E, or B or two of them simultaneously have been developed in order to investigate the decomposition products in the first or second field-free regions of instruments of either geometry.

An easy form of tandem mass spectrometry experiment (MS/MS) is accessible by using reverse-geometry magnetic sector double-focusing mass spectrometers. In this geometry, the magnetic sector precedes the electrostatic analyser and the ions are activated in the region between the magnetic sector and the electrostatic analyser. The fragment ions will have different energies from the parent ion and their masses can be obtained by measuring the kinetic energy of the ions. Such mass-analysed ion kinetic energy spectra have been applied in a variety of studies[89,90,91]. If ion $m^+_2$ is formed from ion $m^+_1$ and if $E_1$ and $E_2$ are the electric field strengths necessary for the parent ion ($m_1$) and the fragment ion ($m_2$) respectively to be transmitted, the mass of the daughter ion $m_2$ can be calculated as:

$$m_2 = m_1 \frac{E_2}{E_1}$$

Extension of these concepts has lead to three-[92] and four- sector instruments with unique advantages especially in resolution.

Recently, there have been attempts by various groups to combine sector instruments with time-of-flight instruments. Russell's group[93] have combined a magnetic sector (Kratos MS-50), used as the MS-I, with a reflectron time-of-flight

mass spectrometer used as the MS-II. When magnetic sector instruments are used as MS-I the upper mass-range of the instrument is limited by the analysis capabilities of the magnetic sector which actually are quite low (1000-10000 Da), compared with the molecular masses of many biological molecules (5000-300000 Da).

Neutral-ion correlation methods can be used with the reflectron time-of-flight instrument as MS-II to define the mass of the fragment ion. A particular advantage of the neutral-ion correlation experiment is that either continuous or pulsed ionisation can be used for the time-of flight measurements. Dissociation of the mass-selected ion in the field-free region between MS-I and the reflectron produces a fragment ion and a neutral. The velocity of the fragment ion and the neutral are the same as that of the precursor ion and they could not be separated by a linear time-of-flight instrument. Two detectors are used for this kind of experiment. One of the detectors is used to detect the ions when the time-of-flight analyser is used in the reflectron mode, and the other detector is located behind the reflectron. The neutral fragment will not experience any force due to the reflectron and will strike the detector behind the reflectron, while the charged fragment will be decelerated upon entering the reflectron eventually reaching zero velocity until its direction is reversed. The charged fragment is reaccelerated back to its initial velocity. The time an ion spends in the reflectron depends upon the rate of deceleration and reacceleration which is proportional to m/z of the charged fragment. For the neutral-ion correlation experiment the neutral signal is used as the start for the time-of-flight measurement and the arrival time of the ion is measured. A special requirement for this kind of experiment is the need for a low beam current-density of the order of $10^3$-$10^4$ ions/s in order to minimise the number of false correlations. There are two

major sources of noise associated with neutral-ion correlation experiments, one is the dark current of the detector and the other the noise associated with the ion beam. The sources of noise associated with the ion beam are ions penetrating through the reflectron and being detected by the neutral detector, neutrals created by charge transfer reactions or secondary ions produced by the ions colliding with the surfaces of the reflectron. There are also some other factors making the use of the neutral-ion correlation experiment difficult when matrix-assisted laser desorption/ionisation is used, in particular the extended arrival time distribution of the ion packet which complicates tandem mass spectrometry experiments in two ways. First the start signal for the time-of-flight experiment is not sufficiently defined for high mass-resolution and, second, to achieve reasonable mass resolution it is necessary to pulse the ion beam entering the MS-II in a way that a small slice of the arrival distribution is selected. Although such an experiment can achieve the desired result, the sensitivity is reduced because a large portion of the ions produced is not analysed.

Reflectron time-of-flight mass spectrometers can be also used as MS-II in tandem mass spectrometry without neutral-ion correlation detection. In reflectron time-of-flight mass spectrometers, the ion flight times become independent of energy deviations only for ions of the same m/z. Ions of different m/z that enter the reflectron with the same kinetic energy, penetrate to the same depth in the retarding field regardless of their mass. As discussed before, after fragmentation of the parent ion, all the fragment ions and the parent ion have the same velocity. When ions of different m/z enter the reflectron all having the same velocity, the depth of penetration and the time of residence in the reflectron is directly proportional to the mass of the ion. The time-of-flight for ions of the same m/z will still be independent of small energy deviations after emerging

from the reflectron. Fragment ions do not penetrate into the retarding field of the reflectron as deeply as their parents. Thus the fragments' turn-around times are shorter and they arrive at the detector sooner than their non-fragmented precursors. For single stage reflectrons[94] with a homogeneous deceleration field, the relationship between the flight times of the precursor ion $t_p$ and the fragment ion $t_f$ is:

$$2\left(\frac{t_f}{t_p}\right) = \left(\frac{m_f}{m_p}\right) + 1$$

$m_p$ and $m_f$ are the masses of the precursor and fragment ions respectively.

Tandem time-of-flight mass spectrometry has also been performed by various workers by using linear or reflectron[95] time-of-flight mass spectrometers as MS-I and MS-II. The tandem mass spectrometers using two linear time-of-flight instruments were either in series with a floated collision cell[96] in order to provide time-of-flight separation between the parent ion and the fragment ions, or at normal angle one with the other[97]. In the 90 degree configuration linear time-of-flight tandem mass spectrometer, ions were dissociated by surface induced dissociation (SID) and the fragments were then reaccelerated at 90 degrees to the second time-of-flight mass analyser used as MS-II.

## 1.6 RICE-RAMSPERGER-KASSEL-MARCUS (RRKM) THEORY

In order to describe unimolecular dissociation and activation, various theories have been developed to treat how the energy a molecule possesses is distributed in the molecule. All modern theories of unimolecular reactions are based on an

idea suggested by Lindemann[98] which can be expressed in the following way. When a collision occurs between two molecules, one of them may acquire a critical amount of energy sufficient to enable it to become a product molecule. If the conversion of such energised molecules into products is slow compared with the rate at which they are deenergised by collisions, an equilibrium concentration of energised molecules will be rapidly established. The rate of reaction is proportional to the concentration of energised molecules and thus proportional to the concentration of normal molecules and the reaction will be therefore of first order. At low pressures this situation will not exist. The collisions can not maintain a supply of energised molecules and the rate of reaction will depend upon the rate of energisation and therefore be proportional to the square of the concentration of the reactant molecules.

According to the statistical theory of Rice and Ramsperger[99] and of Kassel[100], the molecule is assumed to be a system of loosely coupled oscillators. The oscillators are assumed to be loosely coupled in order to allow a flow of energy between the normal modes without destroying the separateness of the normal modes.

The Rice-Ramsperger-Kassel-Marcus (RRKM) theory is an extension by Marcus[101] of the Rice-Ramsperger-Kassel theory and the essence of the theory is that the individual vibrational frequencies and activated complexes are considered explicitly. The theory relates to the reaction scheme

$$A^* \xrightarrow{k_a} A^{\ddagger} \rightarrow \text{products}$$

where $A^*$ represents an energised molecule and $A^{\ddagger}$ an activated complex. Energy is allowed to flow freely among normal modes. The energised molecule is a molecule having enough energy to react. It contains in its active degrees of

freedom a non-fixed energy $E^*$ greater than a critical value $E_o$ below which classical reaction can not occur. This critical energy may be defined as the difference between the ground-state energies of A* and A. The energy $E^*$ may include both vibrational and rotational non-fixed energy $E^* = E_v^* + E_r^*$. The energy distribution will not usually be such that reaction occurs immediately. The energised molecules thus have lifetimes with respect to decomposition which are much greater than the periods of their vibrations.

The activated complex A* is recognisable as being between reactant and products and its energy configuration corresponds to the top of the barrier between reactant and products. In figure 1.6.(1) the energy levels of the reacting molecule are presented. The total non-fixed energy[102] of a given activated complex A* is noted as $E^*$. The amount of energy $E_o$ has been used to overcome the energy barrier and has become fixed.

According to the RRKM theory a molecule is assumed to be a system of loosely coupled oscillators. These oscillators are regarded as being equivalent to the normal modes of vibration of the molecule or alternatively as individual vibrating bonds. Energy is allowed to flow among normal modes. The greater the energy a molecule possesses, the greater the possibility that sufficient energy will pass into the bond that is to be broken and the higher the rate for decomposition.

A theoretical study of intramolecular vibrational energy redistribution (IVR) by Oxtoby and Rice[103] showed that energy flow will take place when resonances overlap, and for the resonances to overlap their effective coupling need to be strong. At typical realistic molecular potentials small anharmonicities occur to harmonic systems and resonances do not overlap[104] at low levels of excitation per oscillator[103,105,106]. States with a very uneven distribution of the energy tend

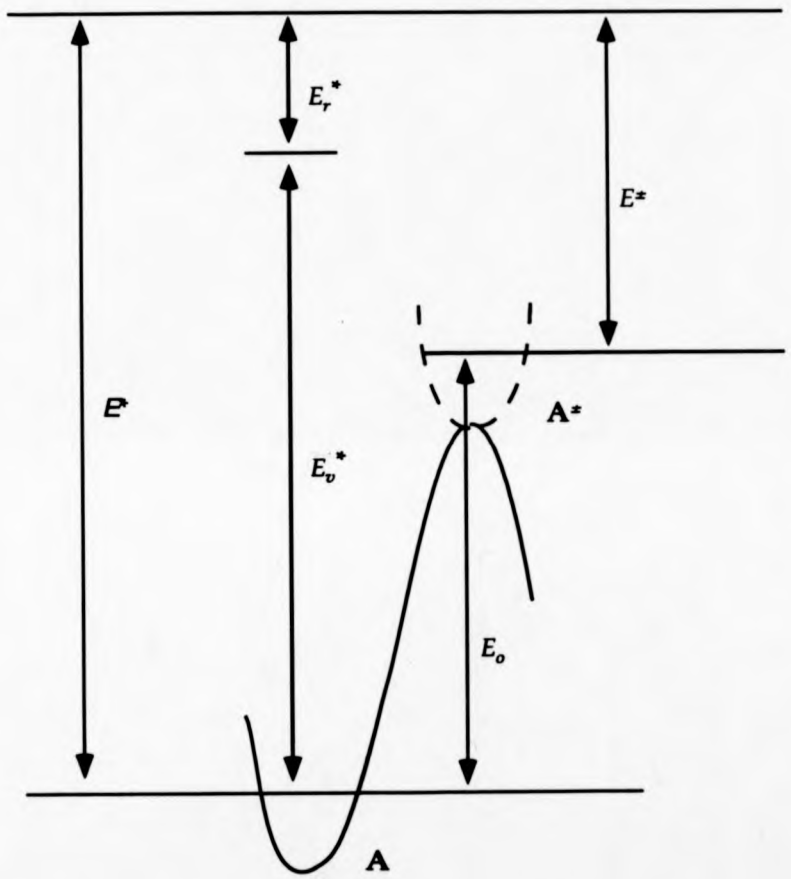


**Figure 1.6.(1) Energy levels of the reacting molecule.**

to be less strongly coupled even at high total energies. The above situation is known as local mode behaviour[107].

Another attempt to explain unimolecular reactions was Slater's theory[108,109], which is a purely dynamical one and takes explicit account of the vibration of the reacting molecules. Slater's theory, in contrast with RRKM, does not permit energy flow among the normal modes during the course of vibration. This theory regards reaction as occurring when different modes of vibration come suitably into phase and a critical coordinate becomes extended to a certain extent. Gill and Laidler[110,111] tried to remove Slater's assumption that there is no energy flow among the different modes of vibration and suggested the reaction scheme:

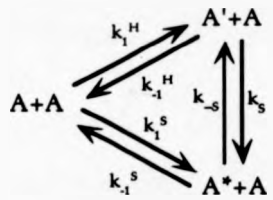


$$A^{\cdot} \rightarrow A^{*} \rightarrow \text{PRODUCTS}$$

The $A^{\cdot}$ molecules contain enough energy for reaction, which is distributed among the normal modes in a way that when vibrations come into phase reaction will occur. The A' molecules contain the critical energy but do not have it suitably distributed for reaction to occur without free flow of energy.

At very low pressures most of the $A^{\cdot}$ may be formed from A' and practically every A' will eventually become $A^{\cdot}$.

Going back to Slater's theory, k(E) is the rate constant for a particular distribution of energy amongst the s oscillators. In Slater's model $\mu_i^2$ are the normalised

weights of the $i$ th normal mode in the linear combination that represents the reaction coordinate. Where:

$$\sum_i \mu_i^2 = 1.$$

The average value of $\mu_i^2$ is 1/s (where s is the number of oscillators), but there can be large variations[112] of the average and the magnitude of the rms deviation of $\mu_i^2$ from 1/s with increasing s. In Slater's model in other words it is quite possible to have different decay rates for different initial depositions of the excess energy. For very large molecules and in particular when the $\mu_i^2$ 's are not uniform in size, it is possible to prepare initial states with fragmentation rates rather higher than RRKM predictions.

## 1.7 OUTLINE OF THE PRESENT WORK

Matrix-assisted laser desorption is a method producing molecule ions in the mass range up to hundreds of thousands Daltons. Desorption of fragment ions is generally not observed in matrix-assisted laser desorption/ionisation. For mass spectrometry, this behaviour has advantages and disadvantages. Analysis of complex mixtures is much easier with mass spectra showing only molecule-ion signals. Because of the lack of prompt fragmentation, however, structural information can not be achieved directly with this method. One of the targets of the present work was to develop a time-of-flight mass spectrometer with which kinetic energies of parent and fragment ions could be measured. For that reason, an energy resolved time-of-flight mass spectrometer was designed and constructed inside the grand-scale reverse-geometry mass spectrometer (see Chapter 2). Computer-simulation programs were developed to allow precision in the design of the ion optical components and to study the effect of the electrostatic analyser on the times-of-flight of the ions. Energy resolved time-of-flight experiments and time-selected energy-resolved time-of-flight experiments, were performed with the constructed instrument. Metastable decay was able to be measured with the energy-resolved time-of-flight experiments, and collision-induced dissociation experiments were also performed showing that collision induced dissociation can offer structural information for large molecular-mass ions. Loss of charge of ions as a result of collision was observed. Collision experiments, in which the total ion current was measured and compared with the total ion current without collision gas, were carried out, showing that charge exchange could account for the loss of charge of a portion of the analyte ions.

# CHAPTER 2

## AN ELECTROSTATIC SECTOR AS PART OF A TIME-OF-FLIGHT MASS SPECTROMETER

### 2.1 INTRODUCTION

Development of mass spectrometric methods for analysis of polar, thermally labile compounds at the picomole to femtomole level is now a realistic objective[113]. In the case of proteins and peptides molecular mass determination is a primary objective of mass spectrometric analysis, however complete or partial sequence information on peptides is also very useful for many biological applications. Because the yield of intact molecule ions relative to fragment ions is very high in matrix-assisted laser desorption/ionisation, structural information is not easily available. Collision-induced dissociation and metastable decay in principle could be used to provide sequence information.

Tandem mass spectrometry is not a routine experiment with time-of-flight (TOF) or other pulsed instruments, and pulse-ionisation methods are not generally compatible with conventional analytical tandem mass spectrometers such as magnetic-sector and quadrupole instruments[114]. In terms of the mass resolution required for selection of the analyte ion by the first analyser of a tandem mass spectrometer (MS-I), high-performance magnetic-sector instruments are advantageous for studies of complex biomolecules. If with a magnetic sector mass spectrometer in which the magnetic sector is scanned, the mass resolution is $R=m/\Delta m$, the ratio of recorded to rejected ions is $<1/(3R)$ and often $<1/(5R)$. Thus for R=100 or 10 000, magnetic-sector mass spectrometers are

theoretically at least 300 or 30 000 times less sensitive than time-of-flight instruments[115]. In time-of-flight (TOF) mass analysers, all ions that are formed initially can in principle be collected at the detector. The ions of different mass-to-charge ratios arrive in rapid sequence at different times, so that a mass spectrum is recorded in perhaps 100 μs. Another advantage of TOF mass analysers is the absence of a limit to the masses of the ions under investigation. This characteristic should be seen in contrast to the performance of magnetic-sector or quadrupole mass analysers, in which only ions below certain mass-to-charge ratios can be recorded. A further advantage of TOF mass analysers is the fact that a complete mass spectrum is recorded in a very short time, so that intensity variations from the sample material can be observed.

## 2.2 AN ELECTRIC SECTOR AS A PART OF AN ENERGY-RESOLVED TIME-OF-FLIGHT MASS SPECTROMETER.

Different configurations for tandem mass spectrometers involving electric sectors have been proposed by various workers. An approach, adopted by Russell et al, involved a double-focusing mass spectrometer, in which the electric sector preceeded the magnetic sector (EB), as the first mass analyser of the tandem mass spectrometer (MS-I) and a reflectron time-of-flight analyser as the second mass analyser (MS-II)[116]. With an instrument such as this, mass resolution of some thousands can be easily achieved for MS-I. The resolution of the second mass analyser (MS-II) of such a tandem mass spectrometer depends mostly on the characteristics of the ion packet coming out of the first mass analyser (MS-I). The magnetic sector in MS-I, imposes a maximum limit to the largest-mass molecule ion that can be selected. The detection efficiency reported by Russell et al for this

instrument was at the femtomole level, but up to 10 000 laser shots had to be accumulated at a repetition rate of 3 Hz. A simplified form of the above instrument, where the first mass analyser of the tandem mass spectrometer (MS-I) was a 15" radius electrostatic analyser acting as a time-of-flight (TOF) instrument, and the second mass analyser (MS-II) was the reflectron time-of-flight instrument, has been described by Russell et al[95]. Although on the instrument described by Russell et al the laser pulse-width was 3 ns, the arrival-time distribution of the ions from MS-I extended to 50-70 μs, and the resolution in the overall tandem time-of-flight experiments was poor. Energy spread of the ion packet can not account for this observed arrival-time distribution, because the ion packet was filtered in energy by the electric sector. Possible sources of the observed spread in arrival-times are the desorption process and the electrostatic fields the ions have travelled through. In the energy-resolved time-of-flight (ER-TOF) mass spectrometer described in this thesis, essentially similar although smaller arrival-time distributions were observed (see below). An examination of the effects of electrostatic analysers on the times-of-flight of ions has been made as part of this study.

## 2.3 RESULTS

The most commonly employed electrostatic field for kinetic energy measurements is the radial field between two coaxial cylindrical electrodes. First-order directional focusing for ions emerging from the entrance slit of the electric sector with small angular divergence is offered by such a field in the horizontal plane, and there is no focusing at all in the vertical plane. The distance between the two cylindrical electrodes is usually small compared with their mean radius $\alpha_e$. If an ion enters normal to the electric field, it will describe a circular path

through the field, only if it has the correct energy to make the centripetal force balance the electrostatic force acting upon it. An ion with vector of velocity v, entering an electrostatic field $E_r$, will experience a coulombic force F in the direction of the field lines. The vector of velocity remains normal to the field lines only when the ion enters the field at the normal angle, and the kinetic energy of the ion is appropriate to make the centripetal force balance the electrostatic force. In any other case, the magnitude of the velocity vector will change and the ion will describe a more complicated trajectory.

In order to understand and evaluate the factors affecting the times-of-flight of ions travelling through the electrostatic sector, a numerical integration, computer simulation program was developed. The computer simulation program was written in FORTRAN and run on an IBM-compatible 486 computer. Monte Carlo statistics were incorporated to allow the use of distributions in initial angle and energy.

The equations of motion of ions through the electrostatic sector can be expressed more easily in cylindrical polar coordinates $(r,\phi,z)$, and can be written as:

$$m(\ddot{r} - r\dot{\phi}^2) = eE_r$$

$$m\frac{d}{dt}(r^2\dot{\phi}) = 0$$

$$m\ddot{z} = 0$$

The cylindrical polar coordinate system used to describe the trajectories of ions through the electrostatic analyser is shown in figure 2.3.(1).

The potential at any distance r between the two plates of the electrostatic analyser can be calculated using the Laplacian of the electric field, by using as boundary conditions the potentials $+V_1$ and $-V_1$ at the one and the other plate.

The Laplacian of the potential in cylindrical co-ordinates can be written as:

$$\nabla^2 V = \frac{1}{r}\frac{\partial}{\partial r}\left(r\frac{\partial V}{\partial r}\right) + \frac{1}{r^2}\frac{\partial^2 V}{\partial \theta^2} + \frac{\partial^2 V}{\partial z^2} = 0$$

Because of the symmetry of the problem, the electric field changes only in the r direction and hence the terms $\frac{1}{r^2}\frac{\partial^2 V}{\partial \theta^2}$ and $\frac{\partial^2 V}{\partial z^2}$ equal zero. As a result

$$\frac{1}{r}\frac{\partial}{\partial r}\left(r\frac{\partial V}{\partial r}\right) = 0 \Rightarrow \frac{\partial}{\partial r}\left(r\frac{\partial V}{\partial r}\right) = 0 \Rightarrow r\frac{\partial V}{\partial r} = C \Rightarrow V = C_o + C \ln r$$

By applying the boundary conditions, $V=+V_1$ at r=a, where a is the radius of the outer electrode, and $V=-V_1$ at r=b, where b is the radius of the inner electrode, and by considering the potential to be zero outside these field boundaries, the following relationships are obtained:

$$+V_1 = C_o + C \ln a$$
$$-V_1 = C_o + C \ln b$$

Elimination of variables gives:

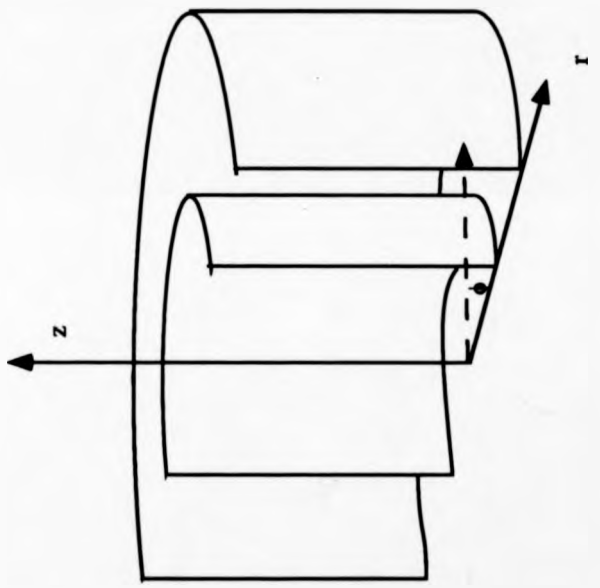


**Figure 2.3.(1)** The cylindrical polar coordinate system ($r,\phi,z$) used to describe trajectories of ions in the radial field between two coaxial cylindrical electrodes.

$$C_o = -V_1 \frac{\ln(ab)}{\ln\left(\frac{a}{b}\right)} \text{ and } C = \frac{2V_1}{\ln\left(\frac{a}{b}\right)}$$

The electric field $E_r$ can be calculated from the first derivative of the potential. The zero potential surface can be calculated by solving the equation $V = C_o + C \ln r_e$ for $r_e$ with potential V=0 at $r_e$

$$0 = -V_1 \frac{\ln(ab)}{\ln\left(\frac{a}{b}\right)} + \frac{2V_1}{\ln\left(\frac{a}{b}\right)} \ln r_e \Rightarrow \ln(ab) = 2\ln(r_e) \Rightarrow r_e = \sqrt{ab}$$

All the other equipotentials are surfaces coaxial with the electrodes. Ions entering the field at any radius other than $r_e = \sqrt{ab}$ will lose or gain an amount of energy equal to eV, where V is the potential at the equipotential surface with radius r.

The potential and the field vector were calculated analytically. The position and the velocity of the ion were calculated numerically, assuming that the forces acting on the ion remained constant for very small time intervals. Outside of the field boundaries, the field vector and potential were assumed to be zero. The study was based on a hypothetical 0.33 m radius electric sector with an electrode separation of 1.1 cm. The object slit and the collector slit in these simulations had a width of 0.165 mm. The object slit was positioned on the ion optical axis 0.1742 m from the electrostatic sector. The collector-slit was positioned at a distance x" from the electrostatic sector, where the lateral displacement y" of the beam would be a minimum. The position of the collector slit was calculated analytically from:

$$y'' = \alpha_e\left[\delta + \frac{\alpha_e(\rho_1-\rho_0)}{\sqrt{2}l_e'}\sin\sqrt{2}\phi_e + (\rho_1-\delta)\cos\sqrt{2}\phi_e\right]$$

$$+x'\left[\frac{\alpha_e(\rho_1-\rho_0)}{l_e'}\cos\sqrt{2}\phi_e - \sqrt{2}(\rho_1-\delta)\sin\sqrt{2}\phi_e\right] \qquad (7)$$

It was assumed that the ions started from a point A' (**figure 2.3.(2)**) with co-ordinates $x'=l_e'$ and $y'=\alpha_e\rho_0$, and entered the field at $x'=0$ and $y'=\alpha_e\rho_1$, where $\alpha_e$ was the mean circular radius of the electric sector[117] and $\phi_e$ is the included angle of the electrostatic analyser. The coordinates of a point at the exit of the electric sector are x", y". The parameter $\delta=\beta+\gamma/2$ is a combination of the spreads in velocity and mass of the ions existing in the ion beam. $\beta$ and $\gamma$ are the velocity and mass spreads respectively, where $\beta=(\upsilon-\upsilon_0)/\upsilon_0$ and $\gamma=(m-m_0)/m_0$ . $\upsilon_0$ and $m_0$ are the velocity and the mass of those ions which when entering the field normal to the field boundary at $r=\alpha_e$ describe a circular path within this field.

Positions towards the outer electrode of the electric sector were considered to be positive, whilst those towards the inner electrode were considered to be negative. The same notation was also used for the angles. Gaussian distributions were assumed for initial values of ion energy, position and angle.

In order to investigate the effect of the energy range transmitted by the electrostatic sector upon the times-of-flight of the ions travelling through the electrostatic sector, a number of trajectories of singly charged ions of different masses between 5000 Da and 5010 Da with different kinetic energies were traced. The ions were started from the object slit of the electrostatic analyser and at three different positions along the y-axis. One group of ions was started from the centre of the object slit, which coincides with the zero potential surface of the

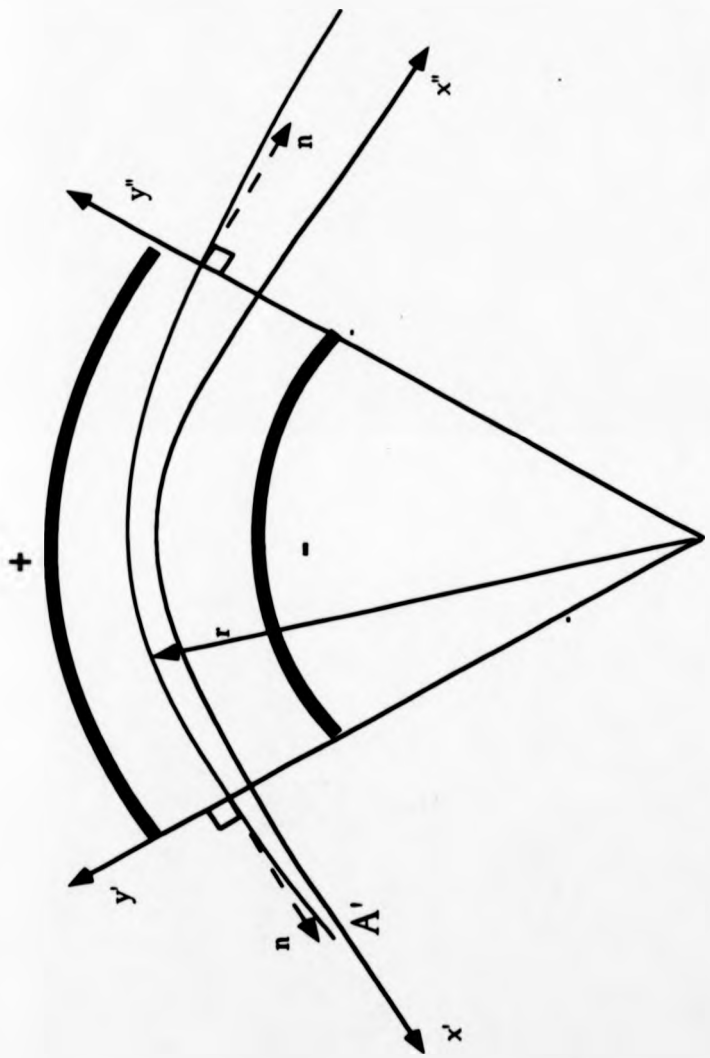


**Figure 2.3.(2)** Diagram of the trajectories of ions in an electrostatic analyser. The ions start from a point A' with position coordinates x' and y' before entering the electrostatic sector. The coordinates of a point at the exit of the electrostatic sector are x", y".

electrostatic sector, and two other groups of ions from either sides of the slit. The ions entered the 81.5 degree electrostatic sector at an angle normal to the field. The results for transmitted ions are presented in figure 2.3.(3) with the times of flight being from the object slit to the collector slit, which was positioned 0.1232 m from the electric sector. Given the range of energies (12 eV) transmitted, the theoretical resolution $t/(2\Delta t)$ was found to be better than 2000.

Ions with m/z 5000 and with the same kinetic energy but different initial entry angles into the field of the electrostatic sector were started from the centre of the object slit, which coincides with the zero potential surface of the electrostatic sector. The initial entry angles varied from -0.5 deg. to +0.5 deg., which represent the limits set by the maximum entry angle transmitted by the electrostatic sector. A time spread of 0.7 μs appeared in an overall flight of 43.64 μs (figure 2.3.(4)), giving a resolution $t/(2\Delta t)$ of not better than 31. A comparison of the time spreads, shown in figures 2.3.(3) and 2.3.(4), demonstrates how critically the initial angle of the ion upon entering the electrostatic sector affects the total times-of-flight of ions of the same energy and mass originating from the centre of the object slit. Ions of a particular mass and energy following trajectories towards the inner electrode of the electrostatic sector are first accelerated and then decelerated, while the ions of the same energy following trajectories towards the outer electrode are first decelerated and then accelerated. The result is different times-of-flight. Apertures could be used to restrict the angular divergence of the ions, creating a well-collimated ion beam. A system of two apertures could be easily implemented on existing instruments, but such an approach would result in great losses of sensitivity. The need to create a well-collimated ion beam and increase the ion signal intensity by increasing the number of ions transmitted by the electric sector implied that some kind of

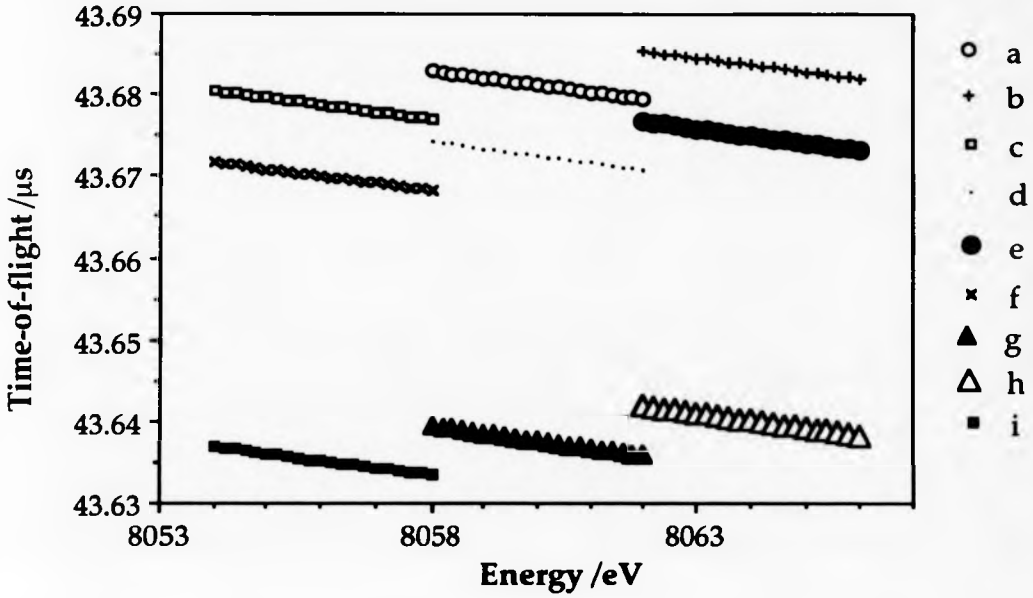


**Figure 2.3.(3)** Times-of-flights of ions with m/z between 5000 and 5010 starting from the centre and from either sides of the object slit.

(a),(b),(c) ions with m/z 5010 starting from the centre, outer and inner side of the slit respectively.

(d),(e),(f) ions with m/z 5008 starting from the centre, outer and inner side of the slit respectively.

(g),(h),(i) ions with m/z 5000 starting from the centre, outer and inner side of the slit respectively.

Figure 2.3.(4) Times-of-flight for ions of the same energy and same starting position,at different initial angles.

focusing would have to be used, in order to allow a larger number of ions to pass through the object slit.

The effect of different deflection angles in electrostatic sectors on the maximum detectable initial angular divergence of monoenergetic ions, originating from the middle of the object slit, is represented in figure 2.3.(5) . The total flight path was 2 m, the object slit was placed 0.175 m from the entrance of the electrostatic sector and the position of the collector slit was adjusted each time for the specific electrostatic sector. The collectors slit positions were adjusted in a way that they would always be at the focal point on the exit-side of the electrostatic sector. The hypothetical detector used in the above calculations had a diameter of 1 cm.

Electrostatic sectors with small angles of deflection possess higher initial angles of acceptance into the electric sector for monoenergetic ions, resulting in higher transmissions. On the other hand, a large initial angle of acceptance increases the time spread and, as a consequence, decreases the time resolution. If a group of ions of the same mass but with a small energy spread is considered, the velocity dispersion can be shown to be $K_e(\upsilon-\upsilon_0)/\upsilon_0$, where $K_e$ is the coefficient of velocity dispersion in a radial electric field and is given by[117]:

$$K_e = \alpha_e\left(1-\cos\left(\sqrt{2}\phi_e\right)\right)+\sqrt{2}l_e''\sin\left(\sqrt{2}\phi_e\right)$$

$l_e''$ is the distance from the exit boundary of the field to the point of focus. This equation giving the coefficient of velocity dispersion shows that a better energy resolution is achieved, when the deflection angle of the electrostatic sector becomes larger for a given radius electrostatic sector.

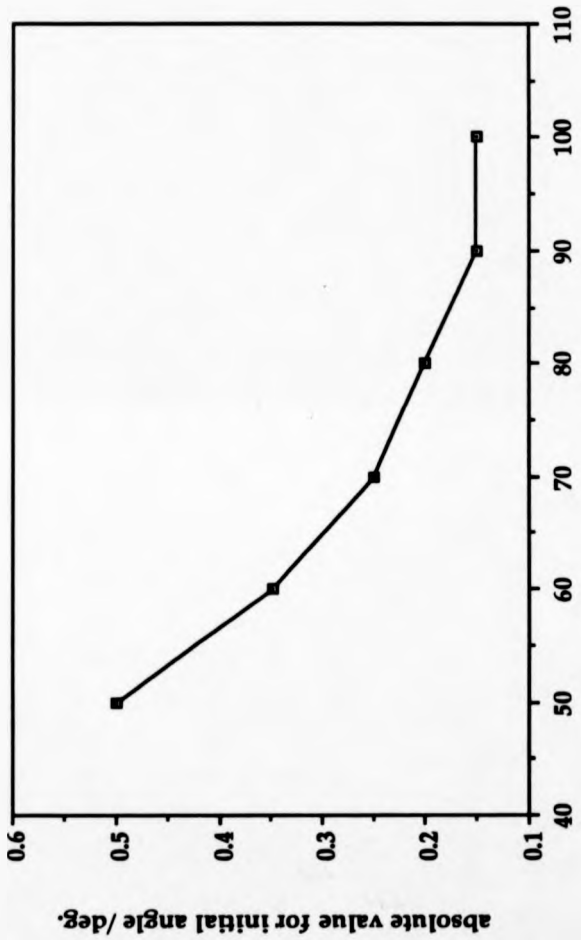


**Figure 2.3.(5)** Initial angle of acceptance for monoenergetic ions for different angles of deflection in electrostatic sectors

To see whether it was possible to improve mass-resolution by some post-sector treatment, an ion packet was generated with distributions of initial angle, energy and position. The standard deviation in angle was 0.3 deg, in energy 3 eV and in position 1/3 of the width of the object slit, with the object slit being 0.33 mm. This packet was run through the simulated instrument subject to the constraint that the angular dispersion dominated the temporal resolution. It was found that the faster ions arrived at the collector slit with positive angles and the slower with negative angles (figure 2.3.(6)). This indicated that the time spread at the collector slit arising from the initial angular distribution could be corrected, if the ions were forced to follow trajectories in a two electrostatic sector system. The ions, which followed trajectories towards the outer electrode of the first electrostatic sector, would follow trajectories towards the inner side of the second electrostatic sector, and vice versa, compensating for the different times-of-flight. The proposed system, figure 2.3.(7), consists of two identical electrostatic sectors in a C configuration, with a slit equidistant from the end of the first sector and the beginning of the second sector. A similar arrangement has previously been considered for energy compensation and beam steering [118,119].

Ions of different energies were transmitted through both electrostatic sectors of the proposed system via the common object and collector slits. The resulting time spreads after both electric sectors for singly charged ions of mass 5000 Da are shown in figure 2.3.(8). Again Gaussian distributions of initial ion conditions were used. The ions were assumed to have an average energy of 8064 eV with a standard deviation of 3 eV, a mean angle of 0 degrees with a standard deviation of 0.3 degrees, and a standard deviation in position of 1/3 the width of the object

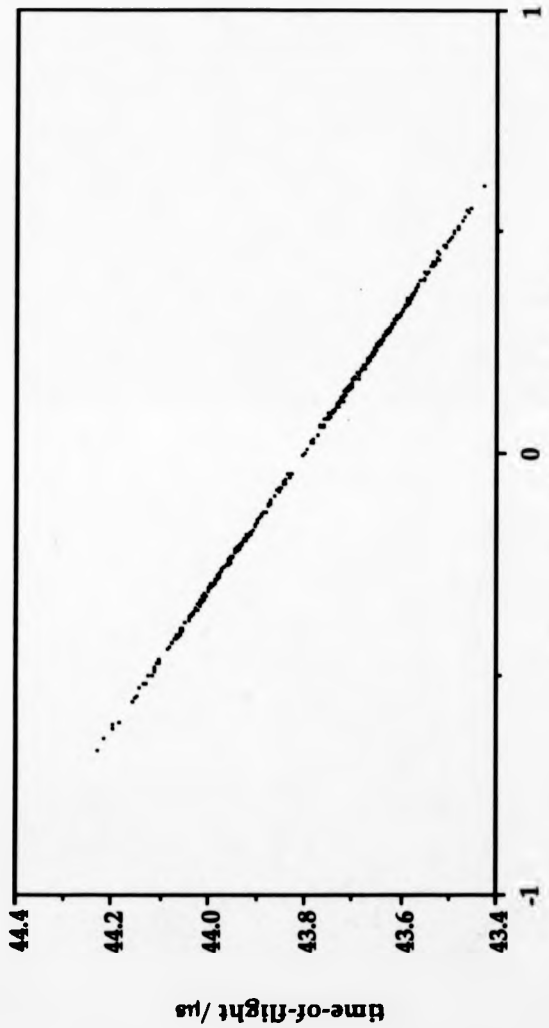


Figure 2.3.(6) Relation between the time-of-flight and the angular distribution upon arrival at the collector slit of ions of the same mass created from a distribution in initial angle, energy and position.

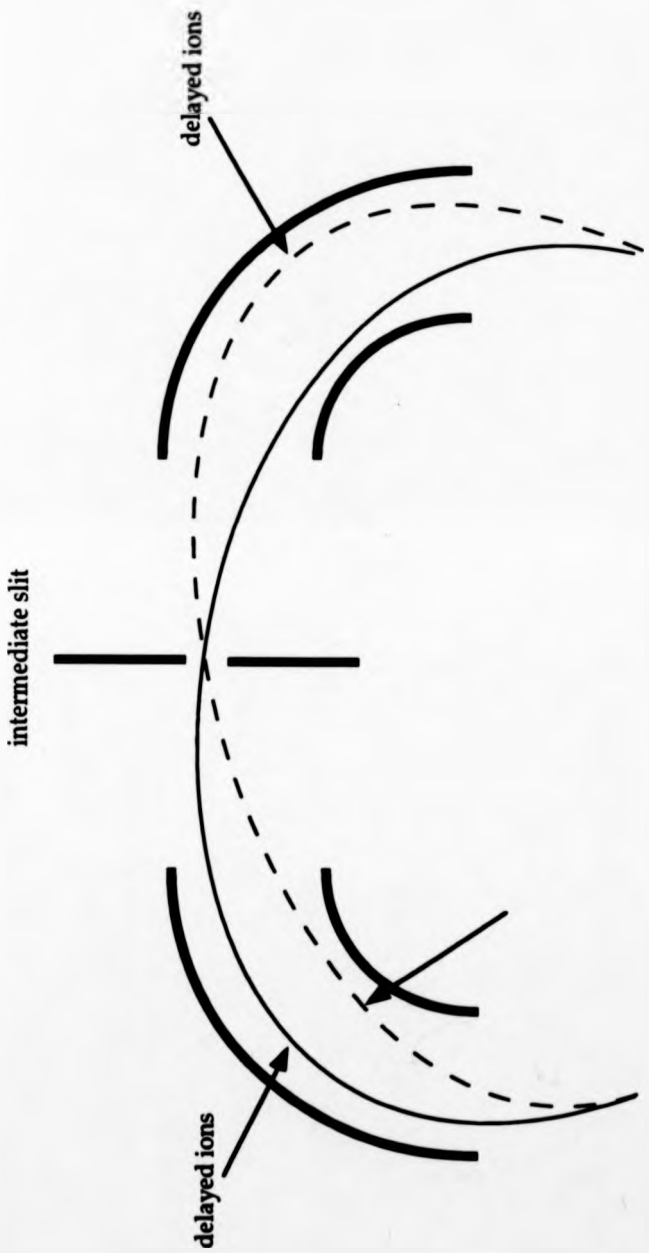


**Figure 2.3.(7)** System of two electric sectors in a C configuration and a slit equidistant from the end of the first sector and the begining of the second sector.

Figure 2.3.(8) Total time-of-flight of ions of different energies in the two electric sector configuration, plotted against the initial angular dispersion for ions of the same mass.

slit. After the second electric sector, the width of the ion packet was 0.015 μs at an overall time-of-flight of 87.61 μs, thus resulting in a theoretical resolution $t/(2\Delta t)$ of approximately 3000. Using one electric sector, the theoretical resolution would be no more than 60.

## 2.4 CONCLUSION

The study of electrostatic sectors and their characteristics as parts of time-of-flight instruments shows that great care should be taken in the design of the ion source and collision cell optics in order to provide a beam with little angular dispersion. As was shown, the major source of time spread of an ion packet when travelling through an electrostatic analyser is the initial angular distribution of the ion packet. Small energy spreads of the ion packet do not affect very much the time resolution. If the solution of two electrostatic analyser system proposed in the above study were used, the initial angular divergence of the ion packet would not play any role in the final time resolution, thus permitting wider angles of entrance and as a result increasing the transmission of the instrument.

# CHAPTER 3

## INSTRUMENTATION, ION OPTICAL CALCULATIONS AND EXPERIMENTAL DESIGN

### 3.1 THE MASS SPECTROMETER (MMM)

The large-scale double focusing mass spectrometer (MMM) (figures 3.1.(1a) and (1b)) was originally designed and constructed at La Trobe University (Victoria, Australia) and was subsequently moved to the University of New South Wales (New South Wales, Australia) in 1981. A second transfer took place in 1987 in which the instrument was air lifted to the University of Warwick ( Coventry, U. K.). The construction of the instrument has been described elsewhere [120,121]

#### 3.1.1 Electric sector

The electric sector (figure 3.1.1.(1a), (1b)) consists of a pair of curved parallel aluminium plates of height 149.5 mm, separated by a gap of 33.5 mm. The radius of the central path (zero potential) through the electric sector is 1000 mm and the sector has an included angle of 81.510°. Herzog shunts[122] shape the field at the entrance and the exit of the sector. The function of the Herzog shunts fitted to the entrance and exit of the electric sector is to reduce the effects of fringing fields, which would lead to defocusing if not corrected for[123]. Matsuda plates[124] improve the field homogeneity in the z-direction.

A control signal generated from the computer through a 16-bit digital-to-analogue converter[125] (DAC) was fed into a high-voltage differential amplifier

**Figure 3.1.(1a)** **Photograph of the large-scale double-focusing mass spectrometer.**

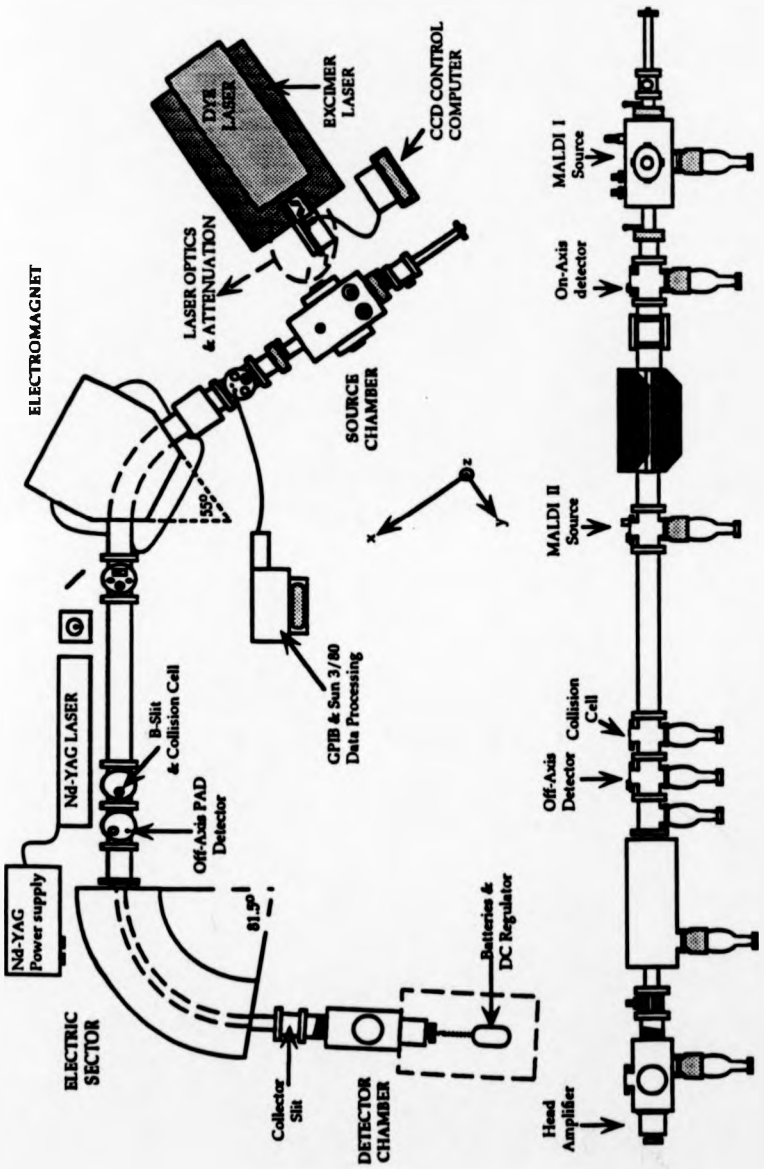


**Figure 3.1.(1b)** Diagram of the large-scale double-focusing mass spectrometer (MMM)

**Figure 3.1.1.(1a)** Photograph of the electric sector.

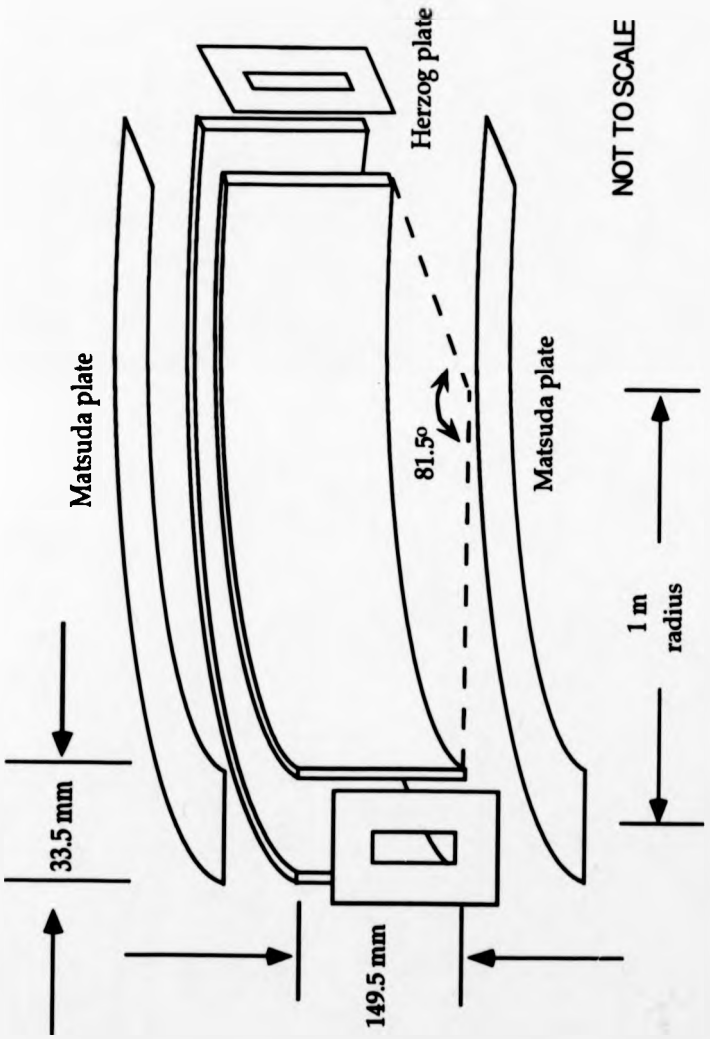


**Figure 3.1.1.(1b)** Schematic diagram of the electrostatic sector used for the energy-resolved time-of-flight experiments.

. This produced two equal voltages of opposite polarities with maximum values of +/-1500 V connected to the sector plates. Potential was delivered to the amplifier by means of two 3 kV power supplies[126].

### 3.1.2 Collision cell

The collision cell (**figure 3.1.2.(1)**) was located just in front of the β-focal plane between the magnet and the electric sector, and supported on the underside of a T-piece flange. The collision cell consisted of two cylindrical stainless steel plates of 64 mm diameter, which formed the ends of a 10 mm long cavity[127] machined from polyethylene. Slits of height 10 mm and width 2 mm in these plates restricted the out-flow of collision gas and allowed adequate transmission of the ion beam. An inert gas could be allowed to leak into the collision cell from the gas inlet via a precision leak valve mounted in the supply line. A variable slit (β-slit) was located at the rear side of the collision cell and could be used to adjust the ion transmission and the energy resolution of the electric sector. In order to contain the collision gas and keep the path of the ion beam in regions of low pressure, the collision cell T-piece was fitted with baffles at either end. The 6 mm wide by 20 mm high aperture in each baffle plate created a pressure difference between the collision cell T-piece and the rest of the instrument. The use of differential pumping to evacuate escaping gas resulted in lower average system pressures, reducing the effects of unwanted collisions[128],[129].

### 3.1.3 Detector

The final image of the ion beam was adjusted by a variable collector slit located at the third focal point of the instrument. The ions were post-accelerated prior to detection in order to increase the detection efficiency[130]. Two deep-cycle lead acid

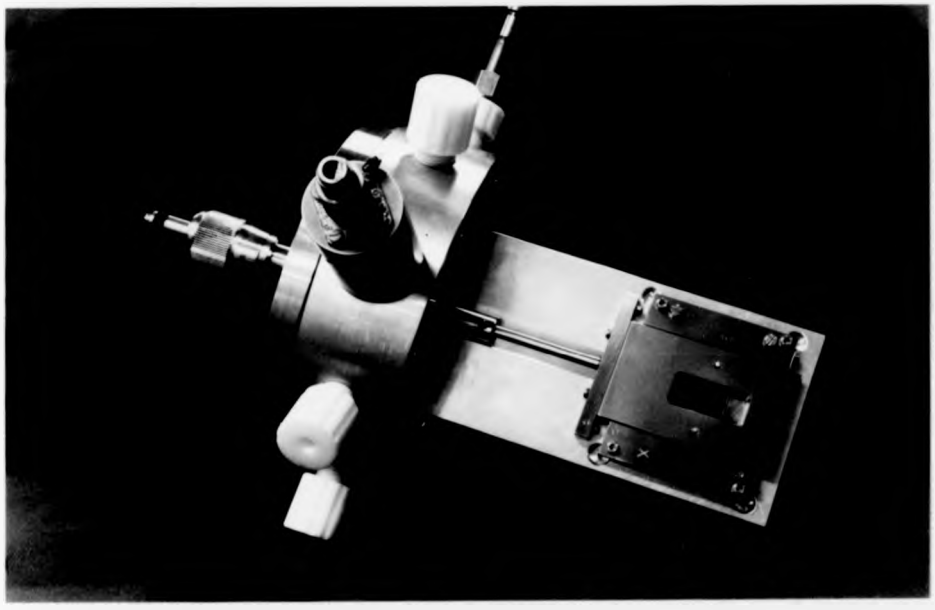

**Figure 3.1.2.(1)** **Photograph of the collision cell.**

accumulators supplied power for the channel plates and also for the ion counting electronics. The electronics consisted of an amplifier/discriminator and associated logic to drive a fibre optic link. The electronics and power supplies were located within a Faraday cage mounted on the top of a large ceramic insulator (figure 3.1.3.(1)). The channel plates, electronics and power supplies were floated at negative 30 kV in normal operation with positive ions. This post-accelerating potential was derived from a 100 kV power supply[131].

### 3.2 LASER SYSTEM

In all of the experiments, the fourth harmonic of a Nd-YAG laser (SL 401 Spectron Laser Systems) was used[132]. The active component of a Nd-YAG laser is a $Y_3Al_5O_{12}$ crystal (YAG is the acronym of Yttrium Aluminium Garnet), where $Nd^{3+}$ ions have taken the place of some of the $Y^{3+}$ ions (<1%). The Nd-YAG lasers have quite a few spectral lines, with one of the stronger and thus most commonly used being the one with wavelength 1.06 μm. A simplified energy diagram is shown in figure 3.2.(1). The $\lambda$=1.06 μm laser transition is the strongest of all the $^4F_{3/2}$-> $^4I_{11/2}$ transitions . The two most important bands appear at 0.73 μm and 0.8 μm respectively. These two bands are coupled through a non-radiative decay with the $^4F_{3/2}$ level, while the lower $^4I_{11/2}$ level is coupled through a fast non-radiative decay with the $^4I_{9/2}$ level. The energy difference between levels $^4I_{11/2}$ and $^4I_{9/2}$ is almost one order of magnitude higher than kT. In other words the $Nd^{3+}$ laser works as a four level system[133]. For the production of the fourth harmonic, a KD*P (potassium dideuterium phosphate) type I crystal was used. This is a frequency doubling process, where the input wavelength is the second harmonic. For the second harmonic a KD*P type II crystal was used.

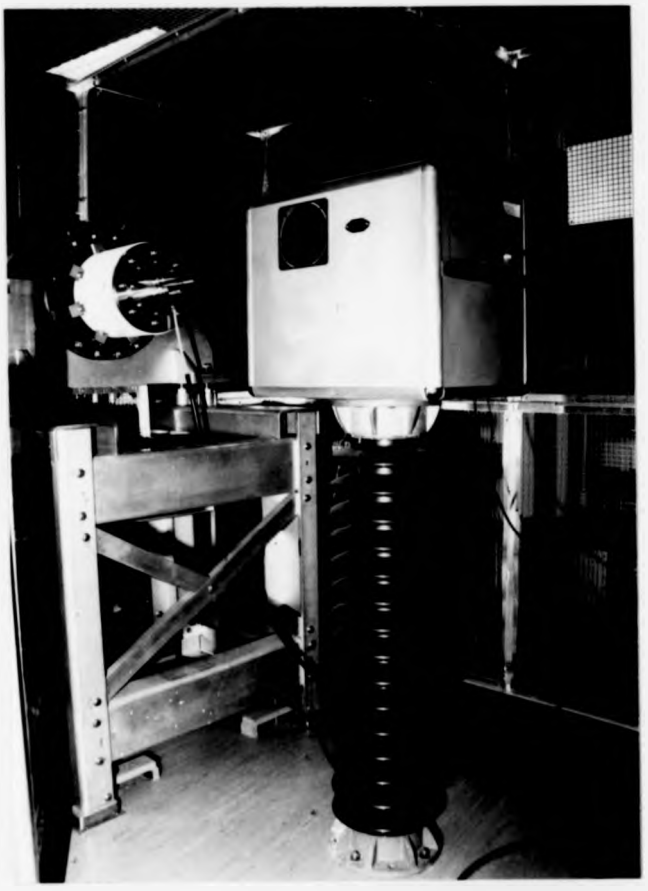

**Figure 3.1.3.(1)** **Photograph of the Faraday cage at the end of the ER-TOF instrument**

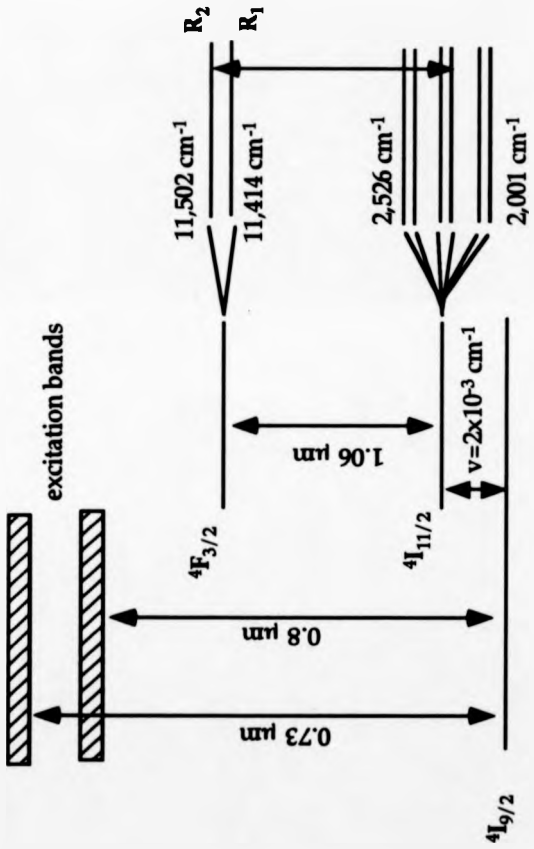


**Figure 3.2.(1)** Simplified energy diagram of Nd:YAG

The laser light was focused and directed to the sample probe (see section 3.4) by using a 50 cm focal length spectrasil lens and a mirror reflecting at the laser frequency used. The intensity of the laser beam was adjusted by means of a Newport high power/UV variable attenuator, model 935-5. The optical arrangement is shown in figure 3.2.(2).

### 3.3 COMPUTER SIMULATIONS

The use of computer simulation programs was dictated by the need to design a laser desorption ion source and an ion detector, which matched the requirements of both the time-of-flight system and the electrostatic sector of the large-scale mass spectrometer. Computer simulation is believed to be the most effective way of designing and testing the theoretical performance of complicated ion optical devices. The set of programs used for ion optical simulations consists of two parts: programs for calculating the potential distribution for the system to be modelled and programs for calculating the ion trajectories[134]. Different programs exist for each part for two dimensions and for three dimensions. Modifications were made to the programs to enable to work under the existing operating system. The three-dimensional ion trajectory computer simulation program was rewritten during this study in FORTRAN programming language and support from graphics and statistical libraries[135] has been added to both the two- and three-dimensional ion trajectory computer simulation programs. Monte Carlo statistics for the initial kinetic energy, initial angular divergence and initial position have been added to give a more realistic approach to the problem.

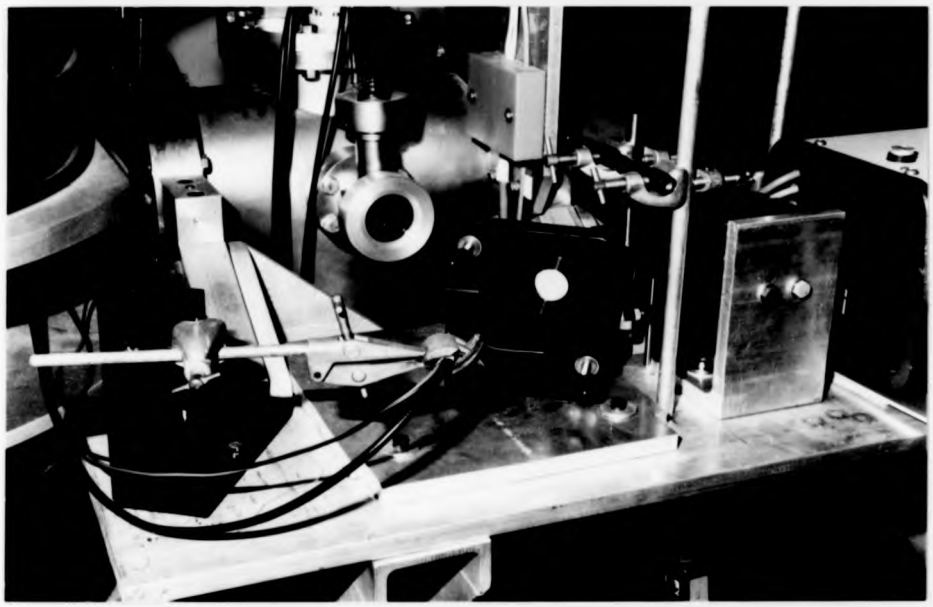

**Figure 3.2.(2)** **Photograph of the optical setting for the matrix-assisted laser desorption/ionisation ion source.**

The programs used in this study are based upon the theory described in the thesis of Rogers[120] and Davis[134], and a small part of this theory is described in the following pages.

### 3.3.1 Potential distribution program

The potential distribution program solves the Laplace equation for the electric field in the region to be modelled, using the method of finite differences. The system to be modelled is superimposed upon a two-dimensional or three-dimensional mesh for the two-dimensional and three-dimensional programs respectively. Iterations are used in order to adjust the potentials at the mesh points, so that the Laplace equation is satisfied. The program uses a method of asymmetric stars to calculate with better accuracy mesh points close to electrode positions[136]. Asymmetric stars give the right contribution of the electrode potential to the potential of mesh points which lie at distances smaller than the mesh point-to-mesh point unit.

Consider a two-dimensional coordinate system and a potential function $\phi(x,y)$ describing the potential at every point x,y. If the field is Laplacian, the potential function satisfies the following differential equation in two dimensions

$$\frac{\partial^2\phi}{\partial x^2} + \frac{\partial^2\phi}{\partial y^2} = 0$$

In three dimensions, the equation becomes:

$$\frac{\partial^2\phi}{\partial x^2} + \frac{\partial^2\phi}{\partial y^2} + \frac{\partial^2\phi}{\partial z^2} = 0$$

In figure 3.3.1.(1), there are four different points with potentials $\phi_1, \phi_2, \phi_3, \phi_4$, where their distance from the point with potential $\phi_0$ is smaller than the mesh point-to-mesh point distance h. If $p_1$, $p_2$, $q_3$, $q_4$ are fractions of that distance h, the distance $\phi_1\phi_0 = p_1h$, $\phi_2\phi_0 = q_1h$, $\phi_3\phi_0 = p_2h$, $\phi_4\phi_0 = q_2h$.

The potentials $\phi_1$ to $\phi_4$ can be expressed as a Taylor series expansion around potential $\phi_0$. Neglecting terms in the expansion higher than two gives:

$$\phi_1 = \phi_0 + p_1h\left(\frac{\partial\phi}{\partial x}\right)_0 + \frac{1}{2!}p_1^2h^2\left(\frac{\partial^2\phi}{\partial x^2}\right)_0$$

$$\phi_2 = \phi_0 + q_1h\left(\frac{\partial\phi}{\partial y}\right)_0 + \frac{1}{2!}q_1^2h^2\left(\frac{\partial^2\phi}{\partial y^2}\right)_0$$

$$\phi_3 = \phi_0 + p_2h\left(\frac{\partial\phi}{\partial x}\right)_0 + \frac{1}{2!}p_2^2h^2\left(\frac{\partial^2\phi}{\partial x^2}\right)_0$$

$$\phi_4 = \phi_0 + q_2h\left(\frac{\partial\phi}{\partial y}\right)_0 + \frac{1}{2!}q_2^2h^2\left(\frac{\partial^2\phi}{\partial y^2}\right)_0$$

In three dimensions there are two more points with potentials $\phi_5$ and $\phi_6$ lying in the z axis .

Consider the two-dimensional case. Combining now the equations for points in x and y gives:

$$h^2\left[\left(\frac{\partial^2\phi}{\partial x^2}\right)_0 + \left(\frac{\partial^2\phi}{\partial y^2}\right)_0\right] = 2\left[\frac{\phi_1}{p_1(p_1+p_2)} + \frac{\phi_3}{p_2(p_1+p_2)} + \frac{\phi_2}{q_1(q_1+q_2)}\right.$$


Figure 3.3.1.(1) Application of asymmetric stars in two- and three-dimensions.

$$+\frac{\phi_4}{q_2(q_1+q_2)}-\phi_0\left(\frac{1}{q_1q_2}+\frac{1}{p_1p_2}\right)\Bigg]$$

It has been assumed that the electric field is Laplacian so that:

$$2\left[\frac{\phi_1}{p_1(p_1+p_2)}+\frac{\phi_3}{p_2(p_1+p_2)}+\frac{\phi_2}{q_1(q_1+q_2)}+\frac{\phi_4}{q_2(q_1+q_2)}-\phi_0\left(\frac{1}{q_1q_2}+\frac{1}{p_1p_2}\right)\right]=0$$

If the potentials $\phi_0$ to $\phi_4$ do not satisfy the Laplace equation, the right hand side of the above equation is not zero but some quantity $R_0$ known as the residual of the difference equation at the point of potential $\phi_0$.

The residual for two dimensions has the value

$$R_0 = x_1\phi_1 + x_2\phi_2 + x_3\phi_3 + x_4\phi_4 - x_5\phi_0$$

and for three dimensions

$$R_0 = x_1\phi_1 + x_2\phi_2 + x_3\phi_3 + x_4\phi_4 + x_6\phi_5 + x_7\phi_6 - x'_5\phi_0$$

where :

$$x_1 = \frac{2}{p_1(p_1+p_2)} \qquad x_2 = \frac{2}{q_1(q_1+q_2)} \qquad x_3 = \frac{2}{p_2(p_1+p_2)}$$

$$x_4 = \frac{2}{q_2(q_1+q_2)} \qquad x_5 = 2\left(\frac{1}{q_1q_2}+\frac{1}{p_1p_2}\right) \qquad x_6 = \frac{2}{v_1(v_1+v_2)}$$

$$x_7 = \frac{2}{v_2(v_1 + v_2)} \qquad x'_5 = x_5 + \frac{2}{v_1 v_2}$$

At any particular point in any iteration the new potential is changed according to

$$\phi_{0new} = \phi_{0old} + \propto \frac{R_0}{x_5}$$

The constant $\alpha$ is called "over relaxation parameter" and is used to decrease the number of iterations used for the potential refinement.

The optimum value for $\alpha$ is different for different problems and also changes from one stage of the computation to another. In **figure 3.3.1.(2)**, values of maximum residuals are plotted against the number of iterations. The A curve is the optimum value for the over relaxation parameter, and although the rate of convergence in the initial stage is not so good it reaches the minimum value for the maximum residual quite quickly. When most of the residuals in one region of the array are of the same sign, higher values of $\alpha$ can be used. If positive and negative residuals are uniformly distributed, a smaller value of $\alpha$ is better.

As has been said, the system to be modelled is superimposed upon a mesh square of side-length h. The potential at any point is kept constant if the node falls within an electrode. The potentials of all the other nodes are modified in every iteration until the preset acceptable accuracy is achieved.

**Figure 3.3.1.(2)** The value of the largest residual (Rm) plotted against the number of iterations (N).

### 3.3.2 Ion trajectory program

After the use of the potential distribution program, the potential of any node is known. In order to calculate the trajectory of the ion, it is necessary to know the potential of any point. The potential is interpolated between mesh nodes with a polynomial, using the nearest nine nodes for the two-dimensional case and the nearest twenty seven for the three-dimensional case.

The polynomial for two dimensions is

$$\phi(x,y) = \omega(1)x^2 + \omega(2)x + \omega(3) + \omega(4)x^2y + \omega(5)xy^2 + \omega(6)x^2y^2 + \omega(7)y + \omega(8)xy + \omega(9)y^2$$

and for three dimensions

$$\begin{aligned}\phi(x,y,z) = {} & \omega(1)x^2y^2z^2 + \omega(2)x^2y^2z + \omega(3)x^2yz^2 + \omega(4)xy^2z^2 + \omega(5)x^2yz \\ & + \omega(6)xy^2z + \omega(7)xyz^2 + \omega(8)xyz + \omega(9)x^2y + \omega(10)xy^2 + \omega(11)xy \\ & + \omega(12)x^2y^2 + \omega(13)x^2z^2 + \omega(14)x^2z + \omega(15)xz^2 + \omega(16)xz + \omega(17)y^2z^2 \\ & + \omega(18)y^2z + \omega(19)yz^2 + \omega(20)yz + \omega(21)x + \omega(22)y + \omega(23)z \\ & + \omega(24)x^2 + \omega(25)y^2 + \omega(26)z^2 + \omega(27)\end{aligned}$$

The $\omega$'s are the coefficients for the interpolation and are calculated by solving the simultaneous equation involving the positions and the potentials of the nearest nine or twenty seven nodes.

By differentiating the polynomial representing the potential function with respect to x and y ( and z for the three dimensional case), the electric field function in the x and y ( and z ) directions is obtained. In that way the forces of the charged particle in the component directions can be calculated at the

particular point of the array. To trace the trajectory of the particle through the array, a small time interval is selected, so that the acceleration during that period remains constant. After that time interval the particle will be in a new position and a new velocity and acceleration are calculated.

### 3.3.3 Milne's and Weddle's rules

To improve the accuracy in regions where the potential is steep, numerical integration methods are used[137]. These integration methods take into account data from previous six positions to calculate the next position.

The first six positions in the beginning of the program are calculated by using Newton's equations of motion. To calculate the next position Milne's method is used, which uses the previous six positions and previous five accelerations to calculate the next position.

$$s_{i+6} = s_{i+5} + s_{i+1} - s_i + \frac{t^2}{48}\left(67a_{i+5} - 8a_{i+4} + 122a_{i+3} - 8a_{i+2} + 67a_{i+1}\right)$$

The acceleration at this new point is obtained by differentiating the potential function at that point.

Weddle's rule uses that acceleration to obtain the velocity at that point.

$$v_{i+6} = v_i + \frac{3t}{10}\left(a_i + 5a_{i+1} + a_{i+2} + 6a_{i+3} + a_{i+4} + 5a_{i+5} + a_{i+6}\right)$$

In every step the total energy of the ion (potential energy and kinetic energy) is calculated, and this value is compared against the initial total energy. The percentage difference in energy between the total energy of the ion at any point

and the initial total energy is used to define the accuracy of the trajectory. If the time interval is large or the mesh size is large compared with the potential gradient, the accuracy of the trajectory is limited. In the case of large mesh size, error derives mostly from the interpolation between mesh points.

## 3.4 ION SOURCE FOR MATRIX-ASSISTED LASER DESORPTION/IONISATION

A primary consideration for the combination of a linear time-of-flight and an electric sector is the ion source optics[138,139,140]. Most types of electric sectors require astigmatic focusing lenses. A well collimated beam is required in the vertical plane of the instrument (XZ direction), to ensure high transmission through the instrument by avoiding collisions with the walls of the spectrometer. In the horizontal plane (YZ direction), focusing is required to achieve high transmission through the slits.

### 3.4.1 Calculations

The spatial asymmetry of the ion source demanded the use of the three-dimensional potential distribution and ion trajectory program for accurate modelling. The laser desorption ion source is shown in figures 3.4.1.(1a) and (1b) and the supporting mechanism of the ion source is shown in figure 3.4.(1c).

Simulated ion trajectories within the ion source together with the electrode potentials used are shown in figure 3.4.1.(2). The trajectory calculation computer simulation program used for these trajectories is the three-dimensional computer simulation program written during the present study. The projection

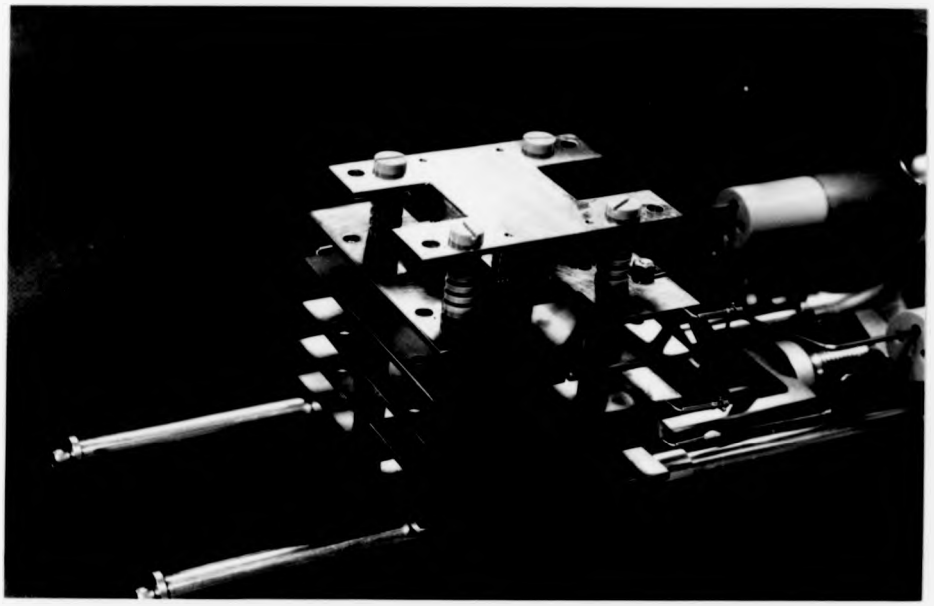

**Figure 3.4.1.(1a)** Photograph of the laser desorption/ ionisation ion source.

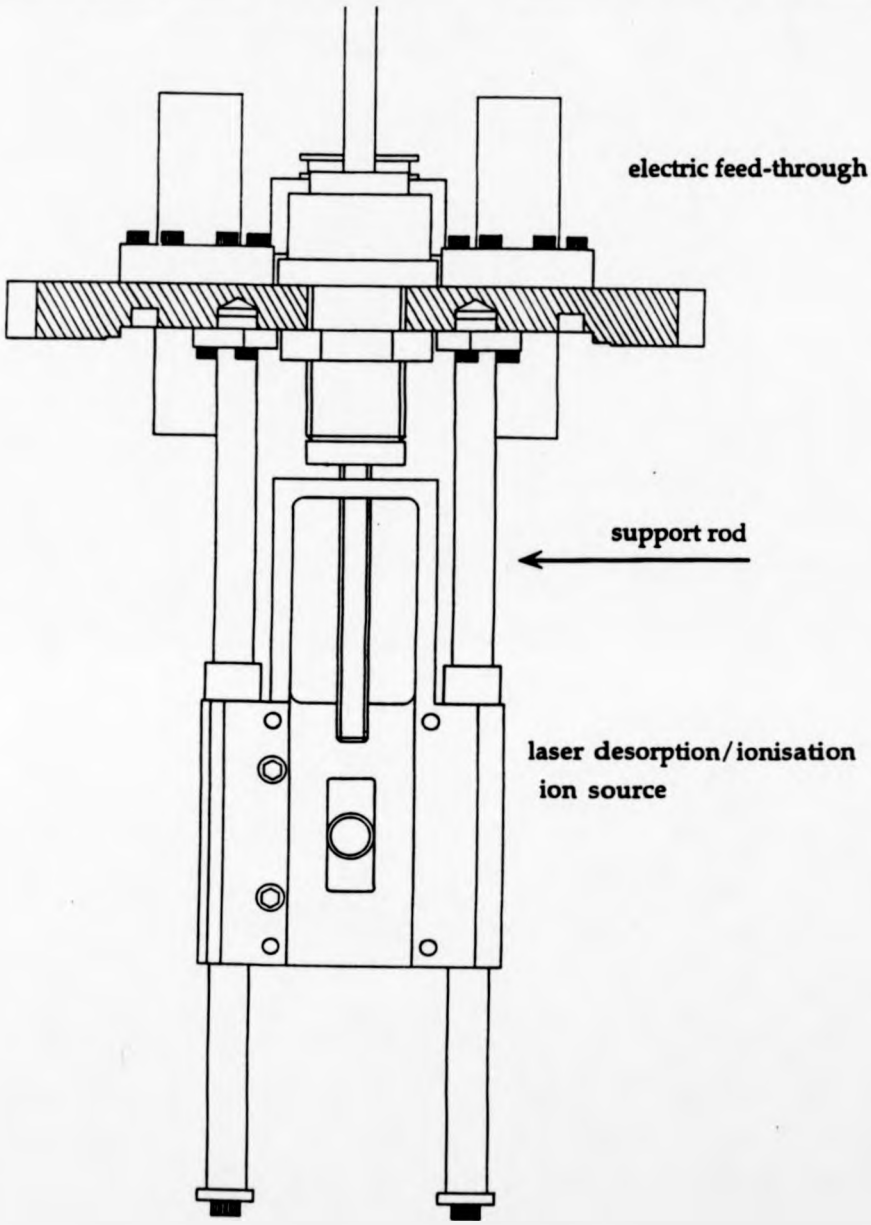


**Figure 3.4.1.(1b)** Diagram of the laser desorption/ionisation ion source

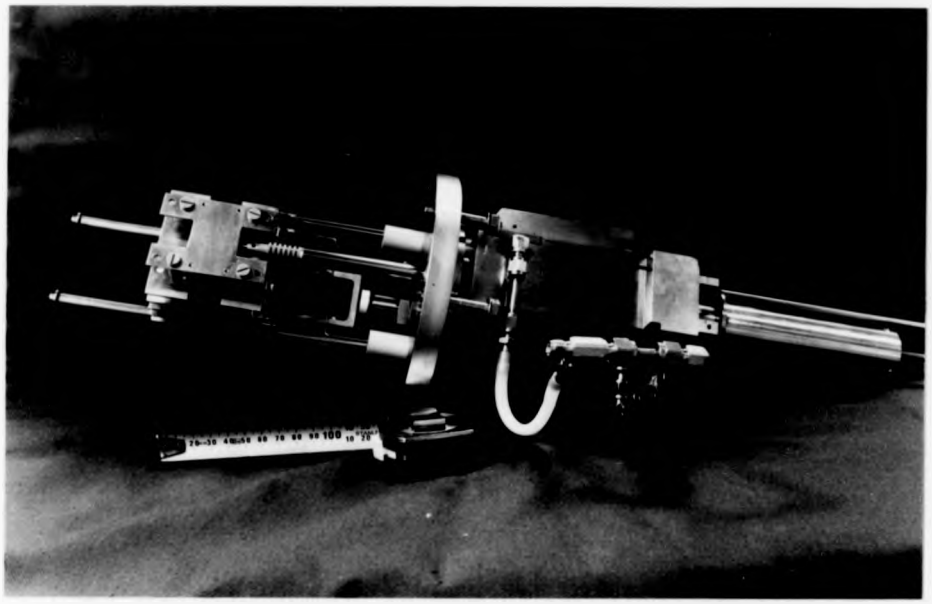

**Figure 3.4.1.(1c)** **Photograph of the supporting mechanism of the laser desorption/ionisation ion source.**

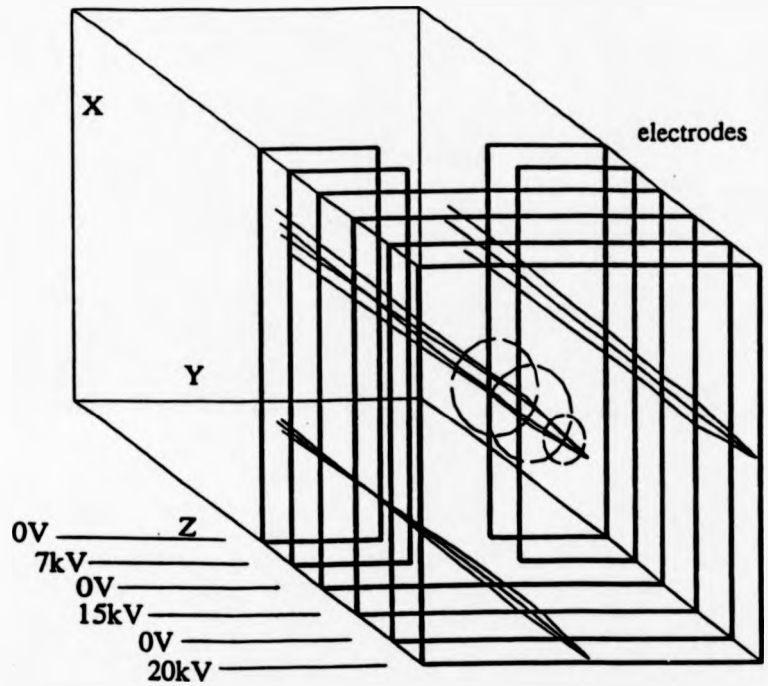


**Figure 3.4.1.(2)** Three dimensional trajectory diagram of the ion source.

a) Projection of the ion trajectory in the xz plane shows that the beam is collimated.

b) Projection of the ion trajectory in the yz plane shows that the beam is focussed.

of the ion trajectory in the xz plane shows that the ion beam is collimated in that plane, while the projection in the yz plane shows that the beam is focused in that plane. In figure 3.4.1.(3) the calculated times-of-flight of an ion are shown as a function of the initial angular divergence. A two-dimensional ion optical computer simulation program written by Davis[134] was used. Ions with different initial kinetic energies ranging from 5 to 20 eV were considered in this calculation. The flight path of the simulated time-of-flight instrument was 2m and the hypothetical detector had a diameter of 2 cm. The accelerating potential was 20 kV and the times-of-flight were calculated for m/z = 5736 (bovine insulin). From figure 3.4.1.(3) it can be seen that ions with higher initial kinetic energy have a smaller cut-off angle in terms of initial angle of divergence. The cut-off angle arises because above this angle ions, after emerging from the acceleration region, travel very close to the high potential electrode of the einzel lens and thus are strongly deflected. Low initial kinetic energy ions need high initial angles of divergence to travel close to the high potential electrode of the einzel lens and be strongly deflected. In the low and high region of initial kinetic energies it can also be observed that there is a "hump" at high initial angle of divergence in the time-of-flight versus initial angle of divergence plot. Such kinds of results mean that ions are decelerated and then accelerated again, thus resulting in larger times-of-flight. The above time-delay happens for a certain combination of initial kinetic energy and initial angle of divergence, when the ions travel close to the electrodes of the einzel lens but are still transmitted to the detector.

In figure 3.4.1.(4) calculated time-of-flight peaks for bovine insulin (m/z= 5736) are shown. The initial parameters of initial kinetic energy and angle were created by using the statistical (Monte Carlo) routines incorporated in the beginning of

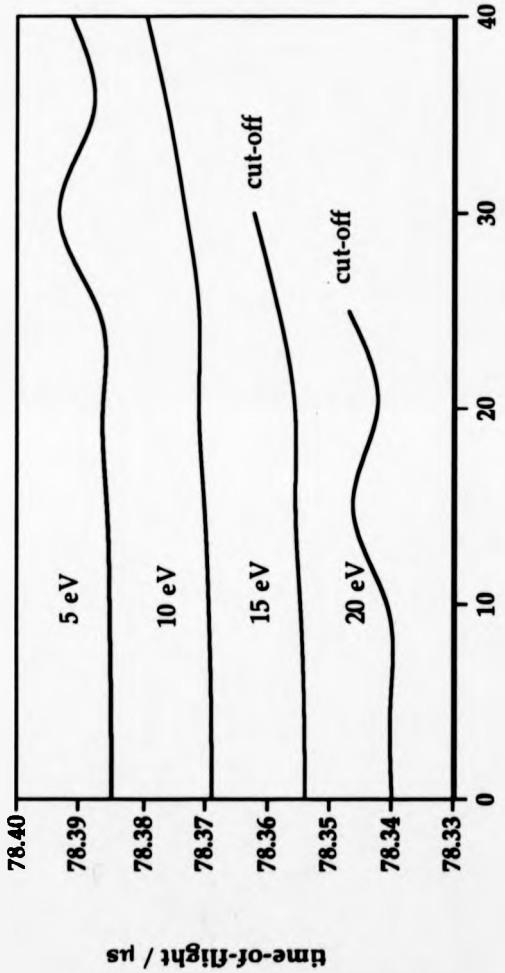


**Figure 3.4.1.(3)** Time dispersion as a function of angular divergence calculated for the laser desorption/ionisation ion source.

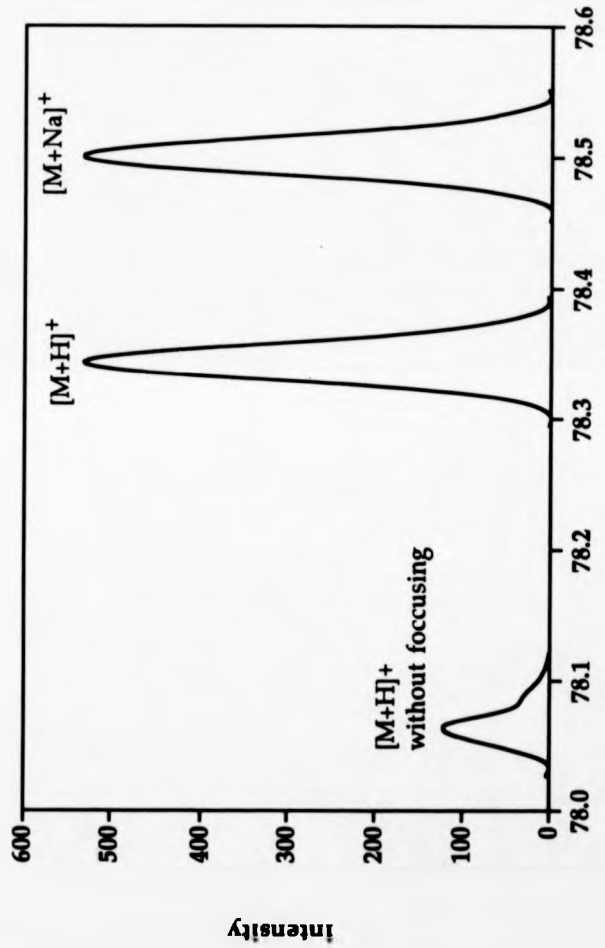


**Figure 3.4.1.(4)** Calculated peaks from the laser desorption/ionisation source for bovine insulin.

this study into the two-dimensional ion trajectory computer simulation program. The flight path was 2m, the accelerating potential 20 kV and the angular dispersion had a mean value of 0° and standard deviation of 20°. The initial kinetic energy had a mean value of 20 eV and standard deviation of 5 eV. From the figure, it can be seen that when the beam was focused the collection efficiency was increased without any significant increase in the time spread.

The use of grids in the construction of the lens of the ion source was considered to be an inappropriate solution, because high precision in steering and focusing of the ion beam was necessary. When grids are used, ions experience an electric field strongly dependent on the spacing of the grid wire. As a result, when a collimated ion beam is transmitted through grids the ions can be strongly deflected. The ion trajectories resulting from the field of a grid are difficult to describe analytically and the loss of sensitivity can become significant when precision in the steering of the ion beam is required[138]. In figure 3.4.1.(5), calculated ion trajectories of ions transmitted through grids are shown. For this calculation, the SIMION[141,142] ion trajectory computer simulation program was used and low-energy ions are considered passing through a -3 kV grid of 0.8 mm mesh size. A collimated beam of ions starts from a 6 kV potential surface. Ions having trajectories close to the wires are strongly affected by the field.

### 3.4.2 Construction

The laser desorption/ionisation ion source was designed to be positioned in the second field-free region of the large-scale reverse-geometry double focusing mass

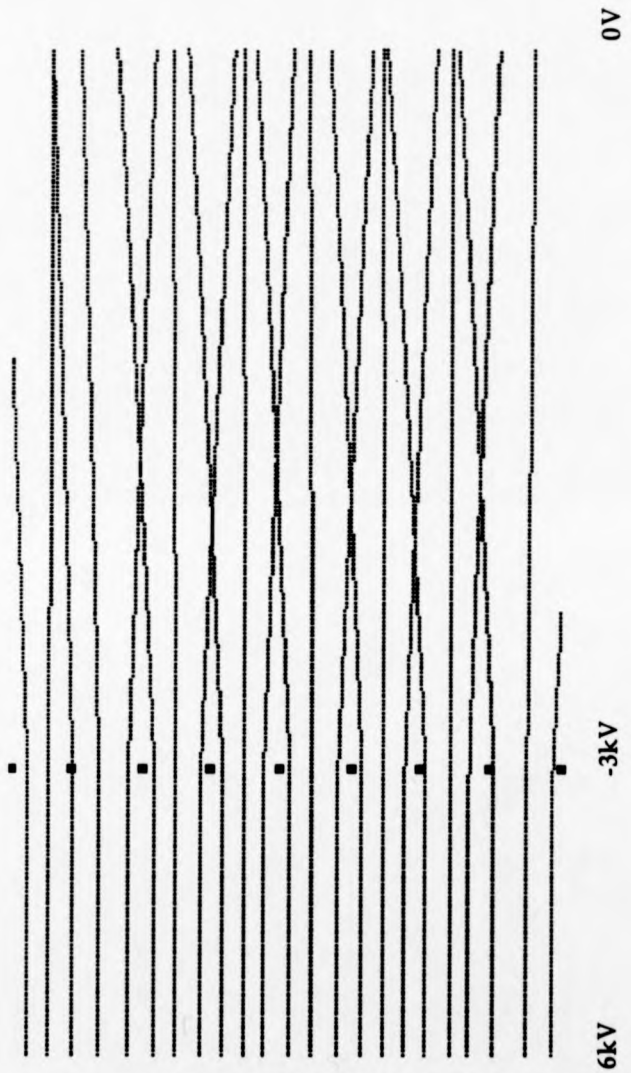


**Figure 3.4.1.(5)** Simulation of low energy ion trajectories through an arbitrary grid ( 0.8mm mesh) showing defocusing effects.

spectrometer. The housing of the source was designed in such a way that the instrument could also be operated (see figure 3.1.(1b)) as a conventional mass spectrometer. The ion source was supported from a flange by means of two rods 10 mm diameter, that allowed the ion source to be slid to a lower position when it was not used. In that way the laser desorption/ionisation ion source was out of the way of an ion beam produced at the ion source of the conventional double-focusing instrument (figure 3.1.(1b)). The supporting mechanism of the laser source is shown in figure 3.4.1.(1c) . The accelerating potential was provided to the first plate of the ion source through the sample probe. The rest of the potentials are provided via feedthroughs and flexible connections.

The sample was introduced to the ion source using a modified solid probe manufactured originally by KRATOS, which was able to hold 1μl of liquid sample. The probe tip was insulated from the rest of the probe by a "PEEK" insulator. Two chambers were employed in order to achieve short times in sample introduction. The probe was first introduced to one chamber, where an Edward's rotary pump pumped the air trapped between the O-ring isolating the sample probe from the atmosphere and the O-ring isolating the sample probe from the ball valve. When the pressure dropped below $1x10^{-1}$ mbar, the ball valve could be opened, allowing the sample probe to be inserted into the source. The plane of the probe tip was parallel to the first plate of the ion source and the probe tip locked in the middle of that plate. The pressure in the first chamber was monitored using an Edwards Pirani gauge and Pirani-11 controller[143]. The pressure in the source housing was monitored by an Edwards ionisation gauge head and an Ion-7 controller.

The laser beam entered the source chamber through a UV-grade fused silica quartz window located on the one side of the ion source, irradiating the sample at a grazing angle.

## 3.5 POST-ACCELERATION DETECTOR

### 3.5.1 Principles of Post-Acceleration Detectors (PAD's)

Ions of very high mass strike the first dynode of the electron multiplier with a much lower velocity than ions of low mass with the same translational energy. Even at a kinetic energy of 20 keV, an ion of mass 100,000 Da has a velocity of only $6x10^3$ $ms^{-1}$. Acceleration of the ions before striking the first dynode of the multiplier is meant to increase the detection sensitivity of high-mass ions. Detection sensitivity of low-mass ions having low translational energy will also be increased by post-acceleration. When large ions that have undergone post-acceleration strike the first anode of the ion multiplier, or in general any conversion dynode, a number of electrons and secondary ions are emitted. Spengler et al[144] have shown that ion-to-ion conversion processes on the dynode surface are predominant for the detection of singly charged ions of masses higher than 20 000 Da. The masses of these ions emitted from the dynode surface have been found to be independent of the nature of the incident ion and the surface itself and to have masses up to a few hundred Daltons[145,146]. Secondary ions of both positive and negative charges have been observed during the conversion process.

Two different kinds of post acceleration detectors (PAD's) were used for the experiments described below. An off-axis PAD was used in the second field-free region of the MMM mass spectrometer in order to allow the instrument to operate as a conventional magnetic sector instrument, as well as a MALDI time-of-flight instrument. In an off-axis PAD, the detector does not block the ion path of the conventional magnetic sector instrument because the ions are post-accelerated normal to the axis of the time-of-flight instrument and both conversion dynode and electron multiplier are not in the way of the ion beam. After the ions are post-accelerated, they collide with the conversion dynode of the PAD. Secondary ions and electrons are produced, which are in turn accelerated towards the electron multiplier where the signal is amplified. The off-axis PAD used in some of the experiments described below is shown in figures 3.5.1.(1a) and (1b). Off-axis PAD's suffer a loss of resolution resulting from the different trajectories the ions follow under post-acceleration. Time dispersion also results from the range of masses of secondary ions emitted from the conversion dynode. Ions of different masses spend different amounts of time flying from the conversion dynode to the electron multiplier. The main advantage of this type of PAD is that the electron multiplier does not have to be floated at a high potential. The second type of PAD, the on-axis PAD, requires that the electron multiplier be floated. With an on-axis PAD the ions are post-accelerated parallel to the axis they travel in the time-of-flight instrument and are directed to the electron multiplier without the need of a conversion dynode. The resolution on these PAD's is much better, compared to the off-axis type. The need to keep the electron multiplier floated in order to provide the post-acceleration creates technical difficulties. Insulation must be provided to the floated power supplies and related electronics. Expensive and very sensitive

**Figure 3.5.1.(1a)** Photograph of the off-axis post-acceleration detector.

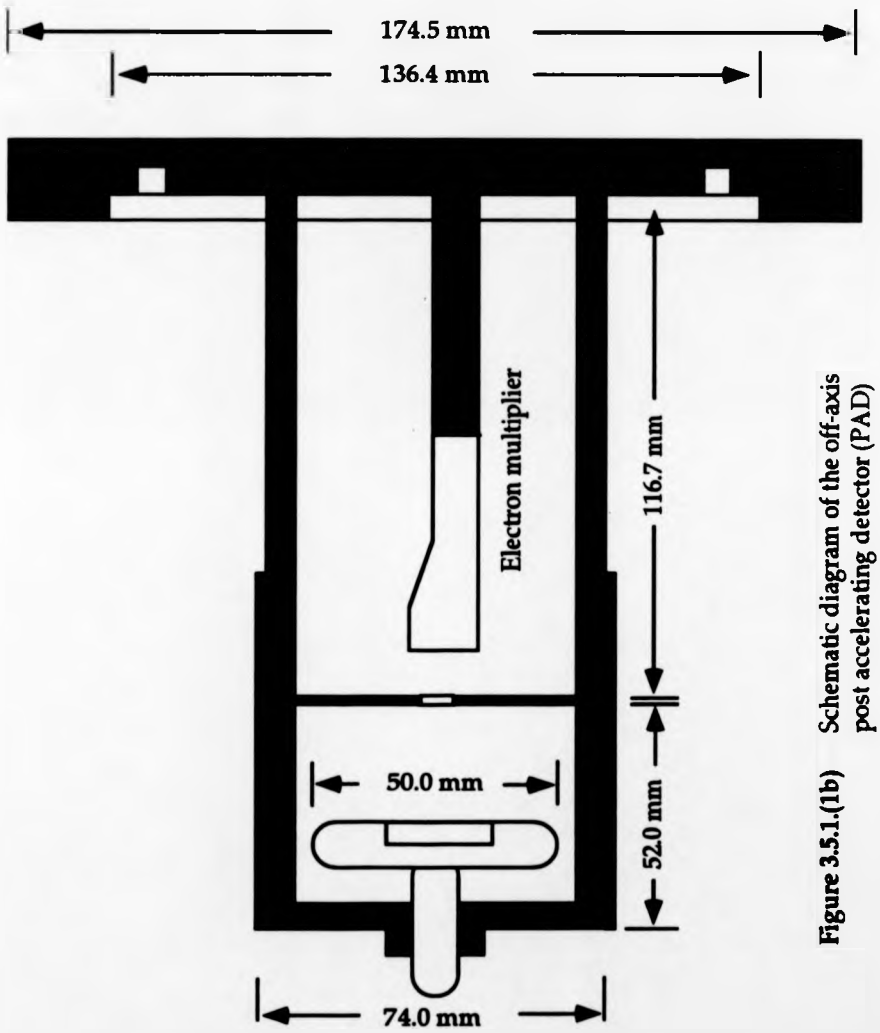


**Figure 3.5.1.(1b)** Schematic diagram of the off-axis post accelerating detector (PAD)

instruments, such as digital oscilloscopes, have to be floated unless optical signal coupling between the electron multiplier and the instrument is provided. Fiber optical links can be used efficiently only in pulse counting mode; most of the applications in this study required analog mode signal acquisition.

### 3.5.2 On-axis PAD without a floated electron multiplier

During this study, an attempt was made to develop an on-axis PAD without the need for the electron multiplier to be floated. The detector was supported in a similar way to the laser desorption/ionisation (LDI) source, allowing the conventional double focusing instrument to be operate when the LDI source was not used. The detector was tested in the second field-free region of the double focusing instrument. A series of three grids, two of high transmission and one of low transmission, were used for post-acceleration and as a conversion dynode (figure 3.5.2.(1)). The first high transmission grid was grounded and used to define the post-acceleration region and separate it from the field-free region. The low-transmission grid was the third of the grids and was used as a conversion dynode. When a negative potential was applied to this grid, positively charged ions would strike the surface of the grid and secondary ions and electrons would in turn be produced. The second high transmission grid was used to direct the electrons produced from the third low transmission grid to the electron multiplier. To examine the performance of this on-axis PAD, a mixture of CsI and KI was used. The accelerating potential was 2300 V throughout the experiments and a Nd-YAG laser was used for the desorption/ionisation. Initially, all electrodes were kept grounded providing no post-acceleration (figure 3.5.2.(2)) . The electron multiplier used to detect the secondary electrons or ions was held at -2 kV. In a second experiment, -15 kV was applied to the second high-

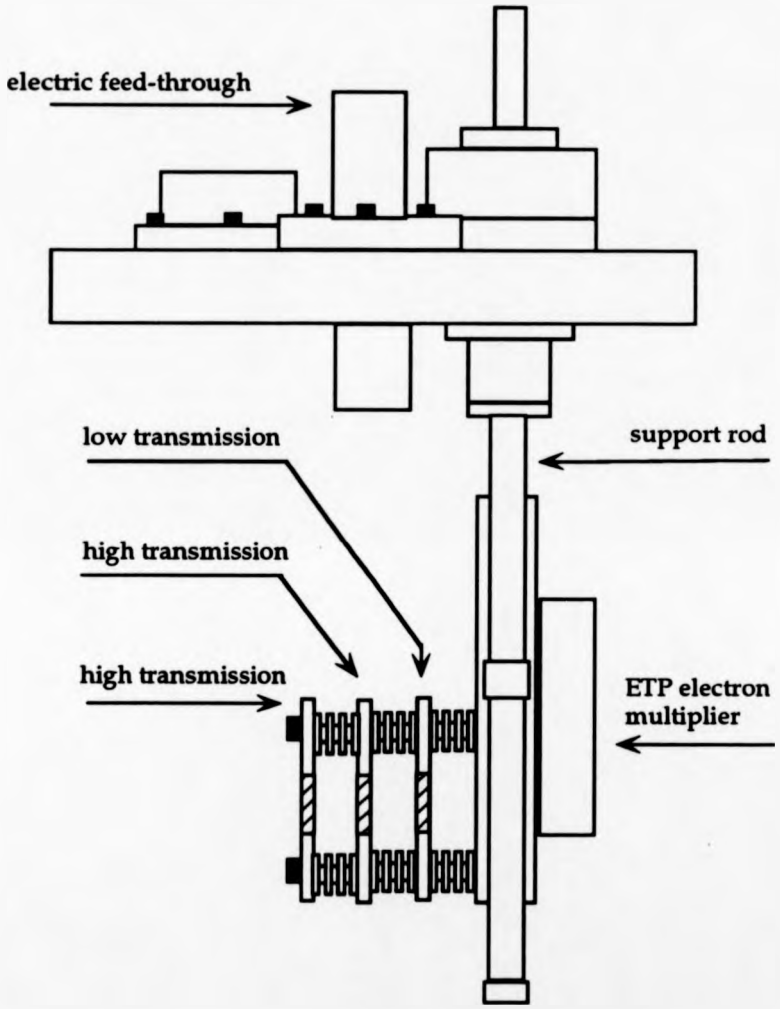


**Figure 3.5.2.(1)** Schematic diagram of the non floated on-axis post-acceleration detector (PAD).

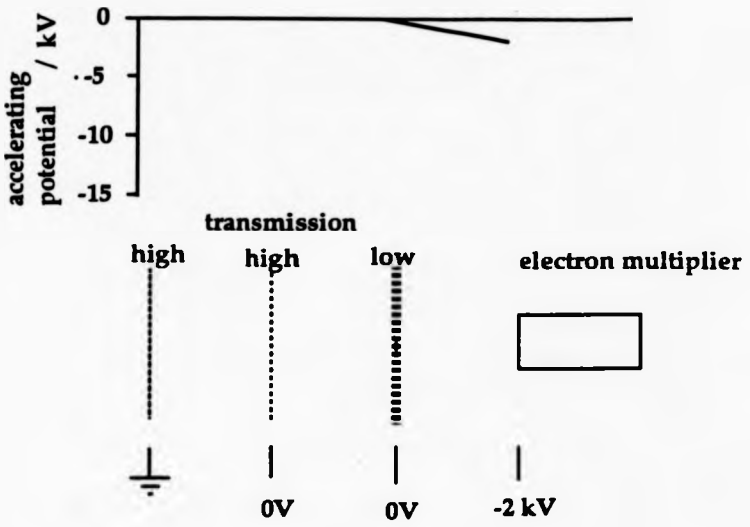
accelerating potential / kV
0
-5
-10
-15
transmission
high
high
low
electron multiplier
0V
0V
-2 kV

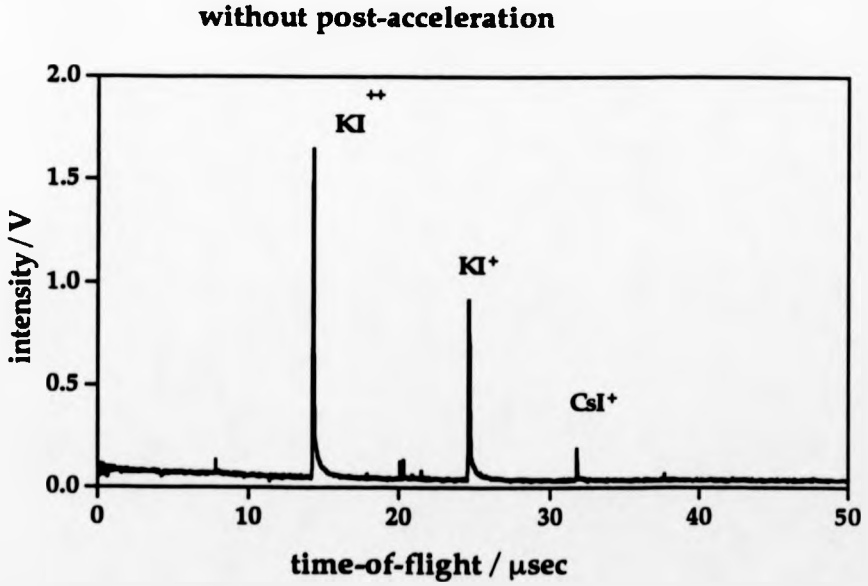
without post-acceleration
intensity / V
2.0
1.5
1.0
0.5
0.0
KI++
KI+
CsI+
0
10
20
30
40
50
time-of-flight / μsec

Figure 3.5.2.(2)

transmission grid and -5 kV was applied to the low transmission grid. The electrode configuration and spectra observed are presented in figure3.5.2.(3). Double peaks were observed for every ion detected when post-acceleration was used. A closer look at the peaks produced with and without post-acceleration is offered in figure 3.5.2.(4). One peak was produced by the ions striking directly the ion multiplier and the other by secondary electrons emitted from the low-transmission grid. The double peaks observed were comparable in amplitude because the ions used for the experiment were of relatively small molecular masses, with high efficiencies of electron production at these kinetic energies. When the masses of the ions were increased to some thousand Daltons, it was expected that the detection efficiency of the electron multiplier would drop almost to zero for ions having only 4300 V total kinetic energy (2300 V obtained from accelerating potential and -2000 V from the potential used at the electron multiplier). Under the above conditions the only contribution in electron production would be from the secondary ions produced by the low-transmission grid. The detector was tested with β-lactoglobulin and 3-nitrobenzyl alcohol as matrix. When post acceleration of 10 kV was used (figure 3.5.2.(5)), β-lactoglobulin ions were observed. When no post-acceleration was used, β-lactoglobulin ions were not observed. The peak width of the resulting signal was not as narrow as was originally expected, which indicated that a number of secondary ions were starting from the low transmission grid with vectors of velocity facing in the opposite direction to the electron multiplier. These ions would have to be decelerated and then accelerated again towards to the electron multiplier, which would give rise to a time spread. Stronger fields would be expected to result in smaller time spread.

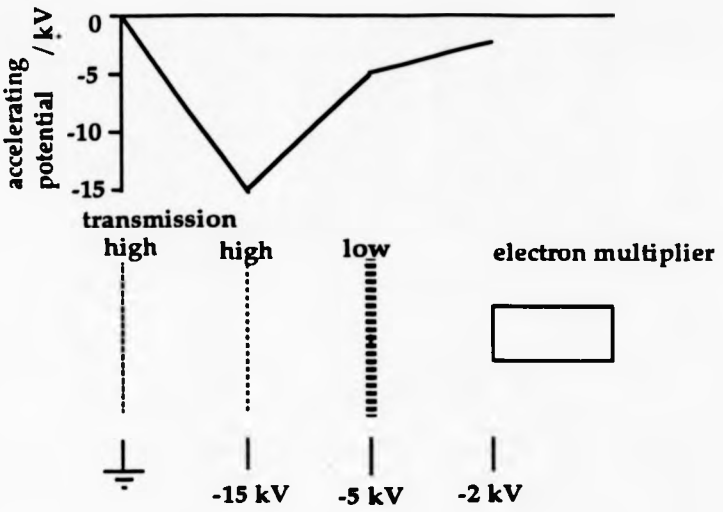


with post-acceleration

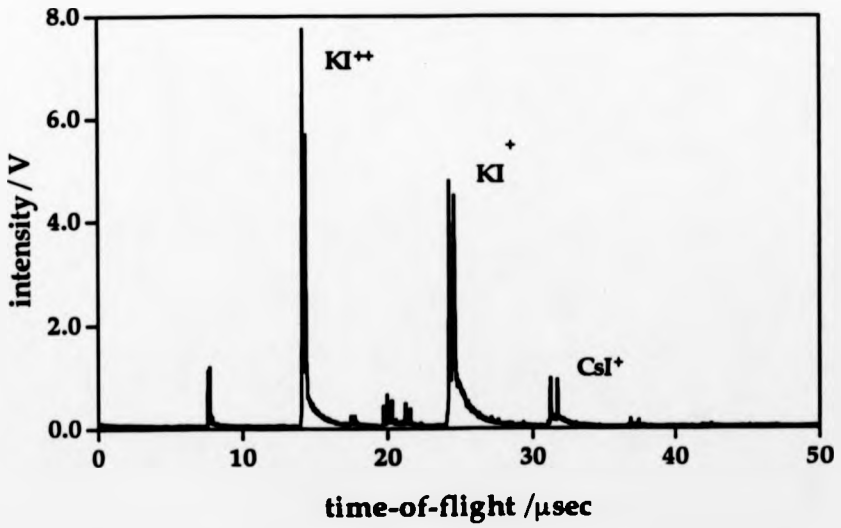


Figure 3.5.2.(3)

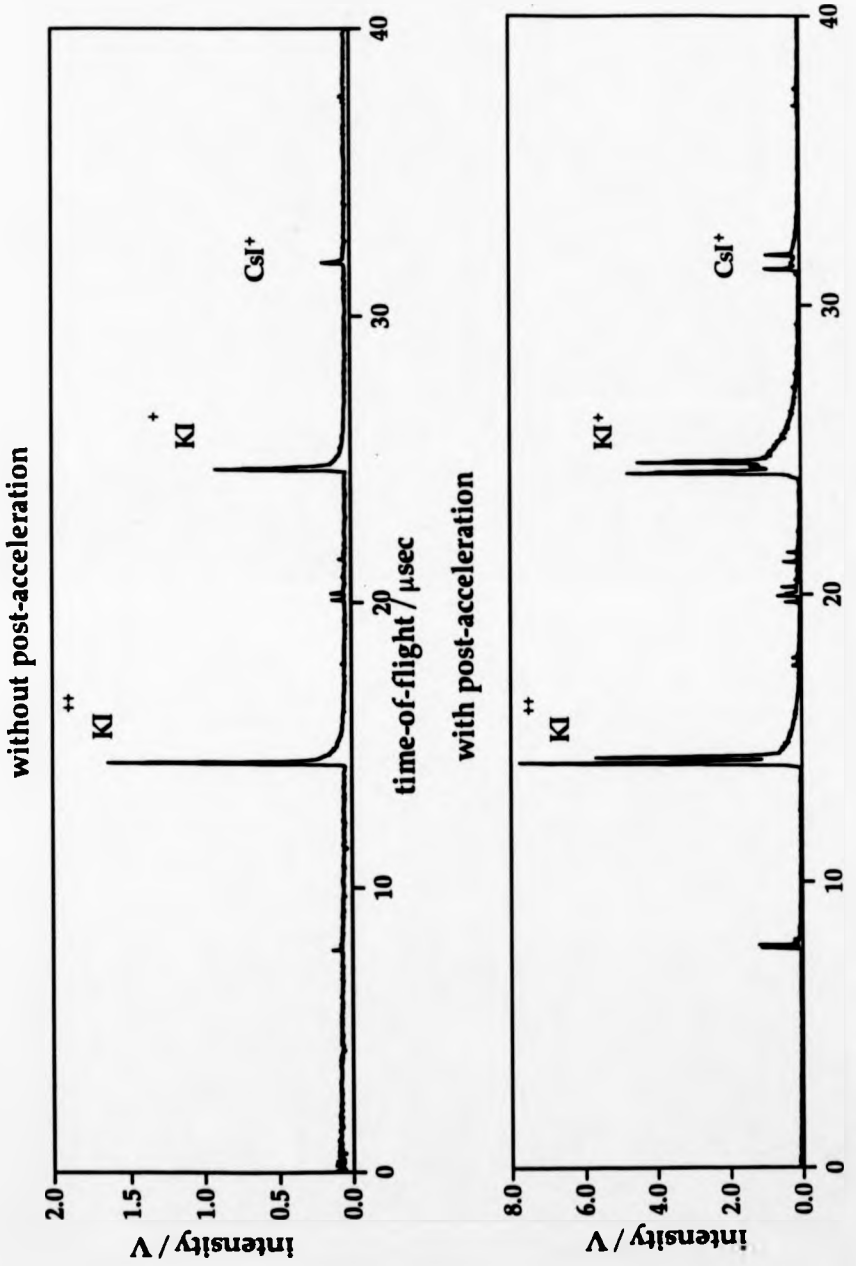
without post-acceleration
KI++
KI+
CsI+
intensity / V
time-of-flight / µsec
with post-acceleration
KI++
KI+
CsI+
intensity / V
time-of-flight /µsec

Figure 3.5.2.(4)

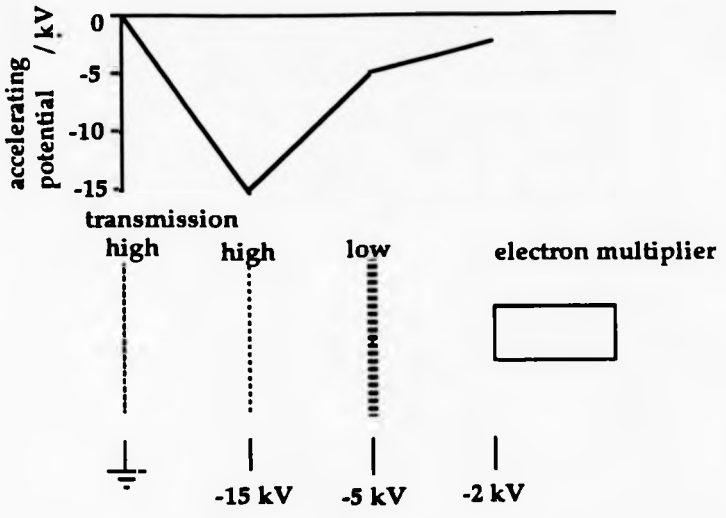


with post-acceleration

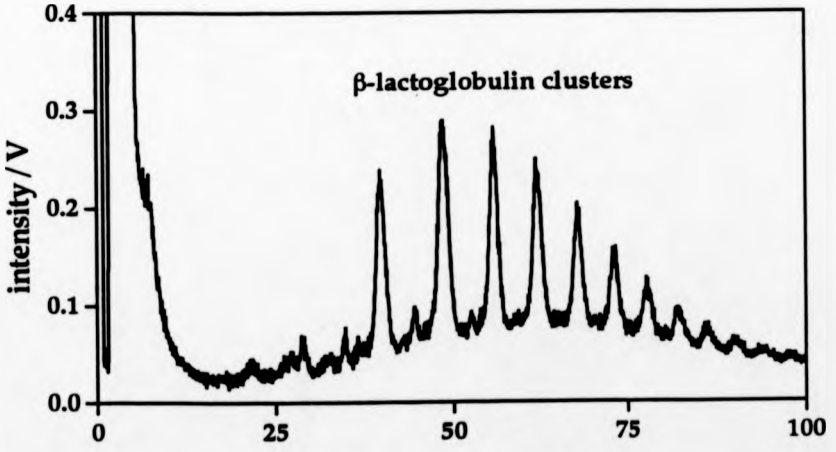


Figure 3.5.2.(5)

### 3.5.3 On-Axis PAD

The post-acceleration detector that was available at the beginning of this study consisted simply of a set of plates with circular apertures. Adjacent plates were separated from each other by a distance of 15 mm, and the plates were connected to ground via a resistor chain. The plates were mounted on three macor rods. The macor rods were grooved to hold the plates, which were kept rigid by a small delrin screw through one of the rods. All plates had well rounded edges and were highly polished to reduce the possibility of corona discharge at the high voltages employed. Trajectories of ions were calculated to examine the focusing action of the post-acceleration lens in the xz and yz planes. Both planes needed to be considered, since the beam would tend to be focused more in the vertical plane than in the horizontal plane. Also because of the rectangular shape of the beam and given that the system had circular apertures, the outermost parts of the beam would be focused more than the inner parts of the beam. Another problem that could possibly arise from the large length of the post-acceleration detector was time spread, caused by the time the ions spent in the post acceleration region. Time spread could become serious in that case when the length of the post-acceleration region was such that the residence time of the ions became comparable with the total time-of-flight of the ions.

Very fast timing applications such as time-of-flight mass spectrometry require a detector that produces very clean and fast signals. In our applications where ion counting was used for the detection of the ions, the need of fast response of the detecting device became apparent. The Galileo TOF-2003 micro-channel plate detector[147] used in the following experiments accomplishes this by means of a 50 ohm matched impedance anode/vacuum feedthrough combination, which

ensures optimum time-resolution with minimum pulse reflections. Pulse width is typically one nanosecond and the detector is bakeable up to 300° C. When a charged particle is incident at the input of a channel, secondary electrons are generated and accelerated down the channel towards the output end. When secondary ions or electrons strike the channel wall additional electrons are generated. This process is continuously repeated until a pulse of up to $10^6$ electrons is generated at the output, and, if two MCP's are used in a chevron assembly, a single input event will generate a pulse of $10^7$ or more electrons. In figure 3.5.3.(1) the operation of the MCP electron multipliers is demonstrated. The pore size of the channels is 10 μm with a centre-to-centre diameter of 12 μm and a bias angle of 12 degrees. The microchannel plate detector was housed in a Faraday cage and floated up to 25 kV to provide the required post acceleration. The post-acceleration region was much smaller than the one used in the old detector, thus providing a smaller time-dispersion. In figure 3.5.3.(2), the detector assembly is presented. The strength of the post-acceleration field could be adjusted by changing the distance of the Faraday cage to the grounded very high-transmission grid used to define the end of the field-free region. For the applications in this study, the detector was used in pulse-counting mode, where the MCP yielded a constant-amplitude output pulse regardless of input event-rate .

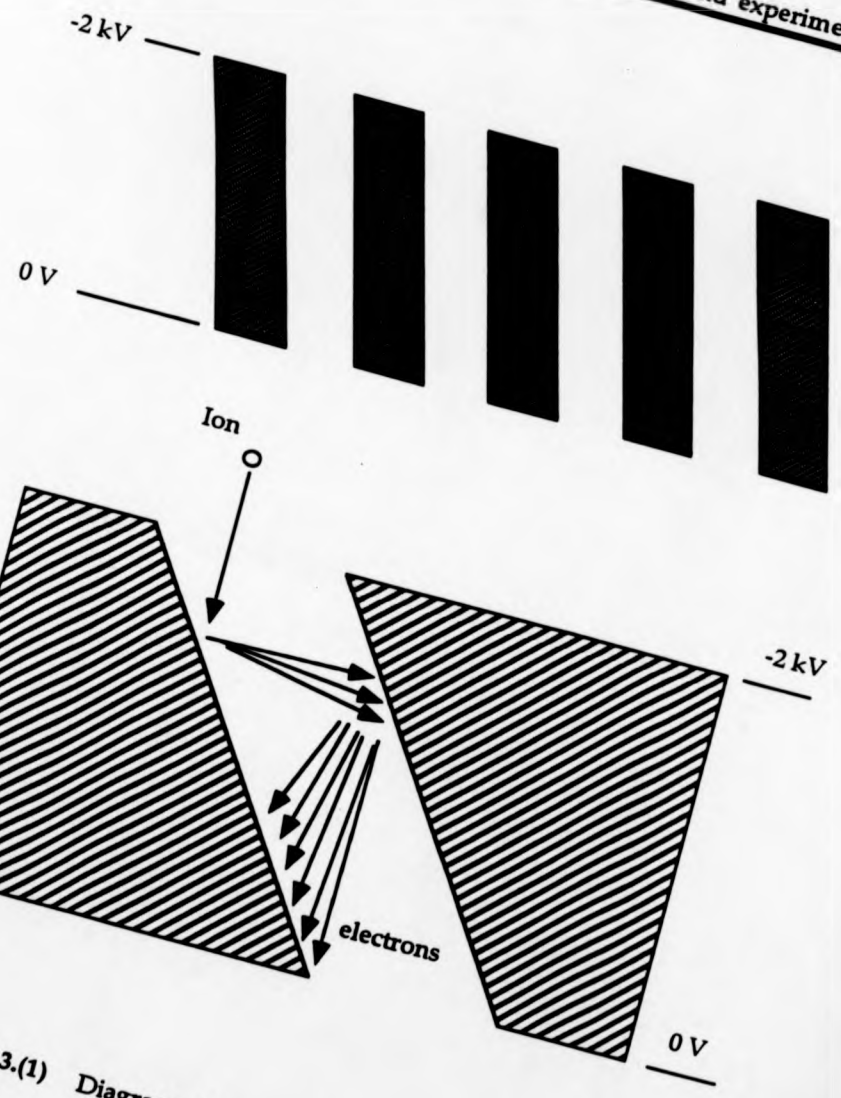


**Figure 3.5.3.(1)** Diagram of operation of the multichanel plate (MCP) electron multiplier.

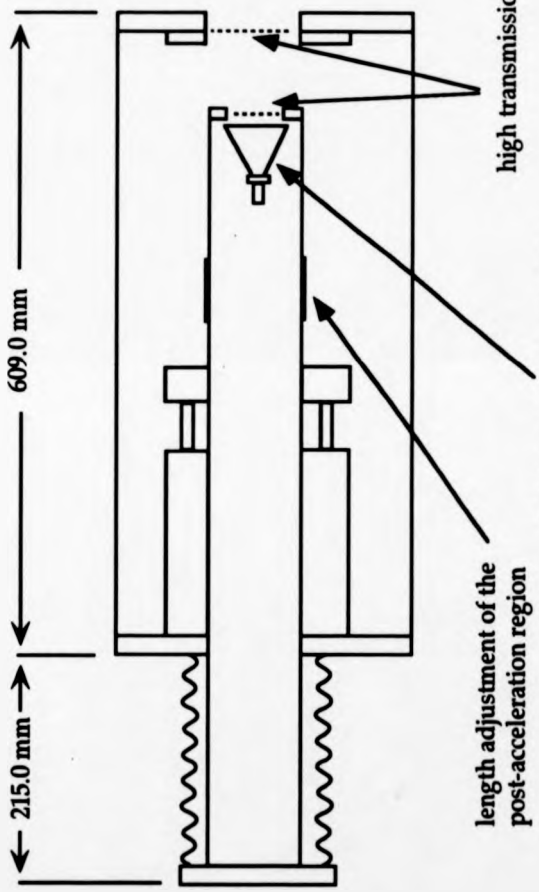


**Figure 3.5.3.(2)** On-axis post-acceleration detector positioned after the electrostatic analyser

# CHAPTER 4

## ENERGY-RESOLVED TIME-OF-FLIGHT MASS SPECTROMETRY

### 4.1 BACKGROUND

#### 4.1.1 Introduction

The application of mass spectrometry to obtain sequence information for a small peptide was first reported in 1959[148], but such measurements required chemical derivatisation to enhance the peptide's volatility. The development of methods to produce gaseous molecule-ions directly from a liquid or solid sample has allowed the derivatisation step to be avoided. In spite of these advances, it is frequently difficult to extract much structural information from the normal mass spectra afforded by methods such as fast atom bombardment (FAB) or liquid secondary-ion mass spectrometry. The peptide $[M+H]^+$ ions often exhibit little fragmentation and the fragment ions observed are difficult to distinguish from artefacts such as background ions from the matrix. These difficulties have stimulated the application of tandem mass spectrometry[149,150] to peptide analysis, using instruments of various configurations[151,152,153,154].

Time-of-flight mass spectrometry is a powerful technique for the mass spectrometric analysis of large biological molecules[155,156]. Conventional magnetic-sector instruments require very large magnetic fields in order to analyse molecules heavier than some thousands of Daltons. The need for such strong fields makes the use of conventional magnetic-sector instruments

impractical for analysis of singly charged ions with masses much above $10^4$ Da. Time-of-flight mass spectrometry overcomes this problem, providing a simple and inexpensive way to mass-analyse large biological molecules. Another great advantage of time-of-flight mass spectrometers is that they require very small amounts of sample, because the whole mass spectrum can be acquired using a single pulse of ions from the source. Magnetic-sector instruments usually require scanning of the magnetic field in order to acquire a complete spectrum. Recent developments in array detectors provide a better use of the available sample by allowing a part of the spectrum (typically <20%) to be acquired in every step of the magnetic sector. Another reason why conventional mass spectrometers require larger amounts of sample is that the ion beam is normally energy filtered to some extent. In TOF instruments, the whole-energy spectrum is collected. When ions undergo metastable decay or collision-induced dissociation in the field-free region of a TOF mass spectrometer, the resulting fragments have different kinetic energies but almost the same velocity as each other. An energy-resolved TOF mass spectrometer would make it possible to use TOF mass spectrometers for tandem mass spectrometry. The energies, at which the fragment ions appeared after the collision, would define the masses of the fragment ions. The mass of the dissociating ion could in principle be chosen by selecting the time-of-flight.

Energy-resolved time-of-flight (ER-TOF) instruments could be used in the study of the mechanism of matrix-assisted laser desorption/ionisation (MALDI) providing information about the initial kinetic energy distributions of the matrix and analyte ions. Quantities such as initial ion velocities can be calculated from the initial kinetic energy distributions. Studies in collision-induced dissociation

and metastable decay can be also carried out in the energy-resolved time-of-flight (ER-TOF) instruments, providing structural information and information about the dynamics of the molecule.

**4.1.2 The effect of electric fields above the target.**

It was discovered that, with matrix-assisted laser desorption/ionisation (MALDI), total ion kinetic energy spectra show ions produced from 3-nitrobenzyl alcohol (3-NBA) / protein samples to have keV energy spreads[138] when there is a strong electric field above the target. These total ion kinetic energy spectra were obtained by using the MALDI ion source, described in chapter 3 and located in the second field-free region of the reverse-geometry magnetic-sector mass spectrometer, and the electrostatic sector of the above instrument. **Figure 4.1.2.(1a)** shows the schematic diagram and **figure 4.1.2.(1b)** shows a photograph of the experimental apparatus. A 3-NBA/β-lactoglobulin sample was irradiated with a wavelength of 266 nm from the fourth harmonic of a Nd:YAG laser. The ions were accelerated using a 8064 V potential. After travelling through the electrostatic analyser the ions were detected by the on-axis post-acceleration detector operating at 30 kV. The electric sector was scanned and the total number of ions was collected for each electrostatic sector potential. It is evident from the MALDI kinetic energy spectrum (**figure 4.1.2.(2)**) that almost all the ions appear at energies lower than the 8064 eV, with an energy spread of about 2 kV.

By placing a grid 2 mm above the target and holding the grid at the same potential as the target, these energy spreads were reduced to some eV as evidenced by the MALDI kinetic energy spectrum (**figure 4.1.2.(3)**) measured after positioning the grid. The comparison of the energy spreads before and after introducing the grid would indicate that these energy spreads were

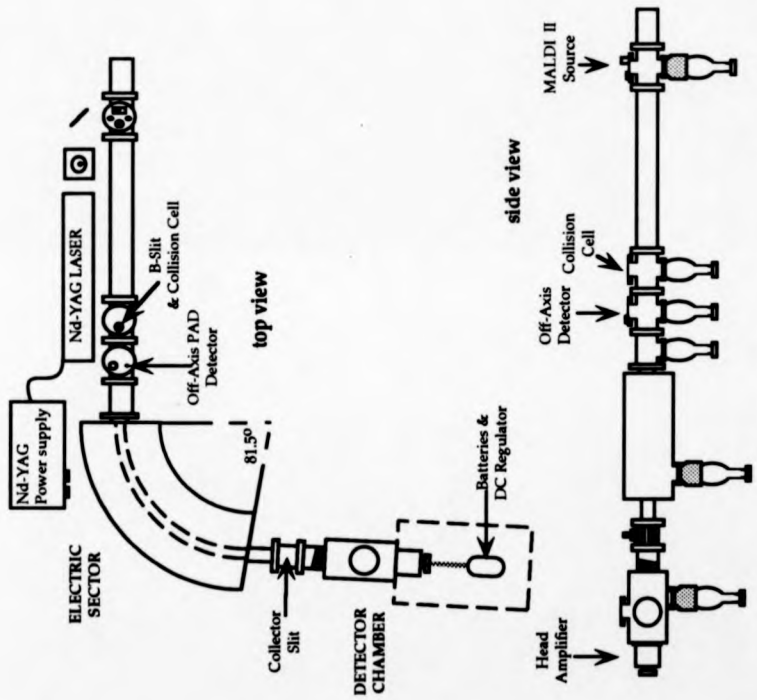


**Fiugure 4.1.2.(1a)** Diagram of the energy-resolved time-of-flight mass spectrometer (MMM)

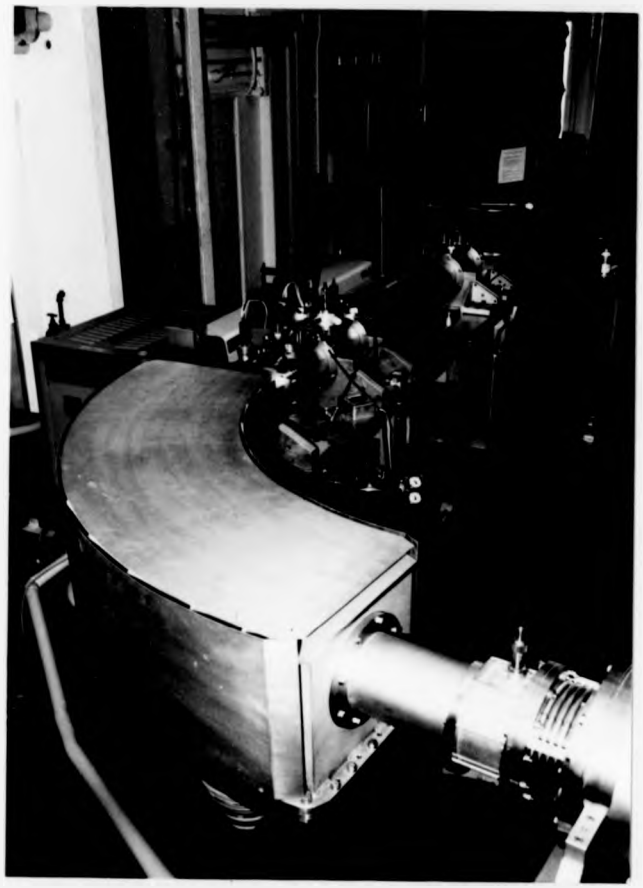

**Figure 4.1.2.(1b)** **Photograph of the experimental apparatus used for energy-resolved time-of-flight mass spectrometry experiments.**

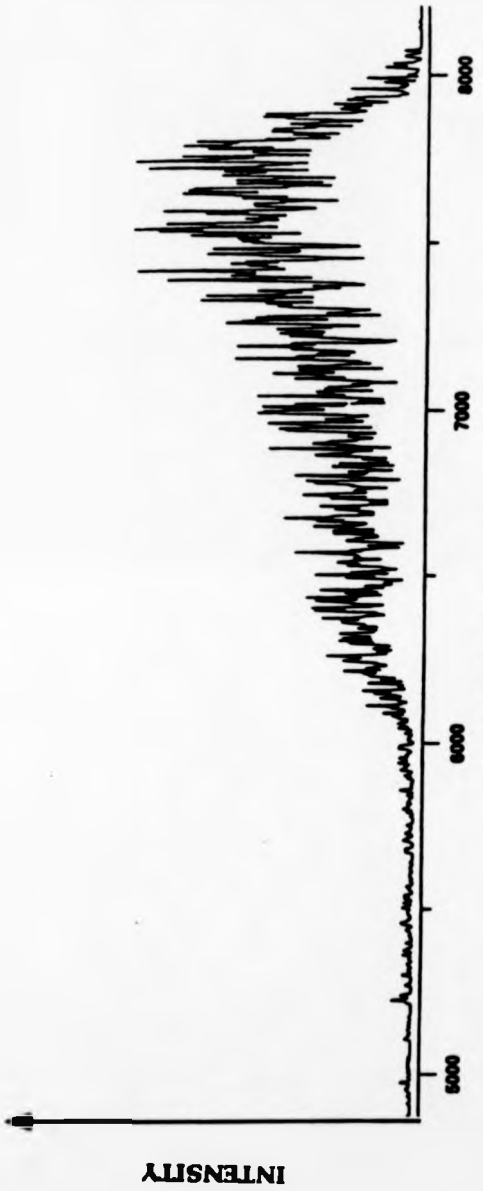


Figure 4.1.2.(2) MALDI total ion kinetic energy spectrum for 3-nitrobenzyl alcohol / β-lactoglobulin

Figure 4.1.2.(3) MALDI total ion kinetic energy spectrum for 3-nitrobenzyl alcohol / β-lactoglobulin ions were produced in a field-free region.

predominantly energy deficits arising from the combination of high electrostatic fields, the liquid nature of the matrix/analyte sample and characteristics of the desorption process. The liquid nature of the matrix/analyte sample could allow surface deformation under strong electrostatic field conditions causing ions to be formed in regions with different electrostatic potentials. The loss in time resolution, arising from the period of time the ions require to drift in this field-free region until they are accelerated, can be considered as a major drawback of placing the grid over the target. By reducing the distance of the grid from the sample, the loss in time resolution can be reduced keeping always in mind that the fringing field from the accelerating potential should not extend to the desorption-ionisation area. The closest distance to the sample at which the grid can be placed is determined by the size of the mesh and the spatial distribution of the ions during the ion formation.

### 4.1.3 Sample preparation

Liquid matrices present some advantages over solid matrices in MALDI. One of the most important criteria for MALDI is the intimate mixing of the analyte and the matrix. With solid matrices impurities can cause a considerable degree of heterogeneity in the resulting sample crystals, possibly preventing the formation of ions[157]. Also it is not uncommon for the distribution of crystals to vary widely over the entire sample probe, which can cause considerable fluctuation in mass spectra obtained from different regions of the sample. The inherent homogeneity provided by liquid matrices eliminates the problems associated with inhomogenous crystallisation. In addition, solutions provide an evenly distributed coverage of the sample over the probe surface which improves shot-

to-shot reproducibility, and, because of the combined effect of sample diffusion and liquid flow, many more laser shots can be "fired" at the same spot as compared to solid samples. These are the reasons that prompted the use of the liquid matrix 3-nitrobenzyl alcohol (NBA) as matrix for the experiments described below.

Particular care was taken with the question of the homogeneity of the sample. Initially, 1µl of $1x10^{-5}$ M aqueous analyte solution would be placed on the top of 1µl of liquid 3-nitrobenzyl alcohol (NBA) and dried (i.e. water was removed) under a stream of warm air. However, it appeared that there were strong spatial variations in the concentration of the analyte-matrix mixture, because analyte peak intensities differed strongly from sample to sample even though with any given sample shot-to-shot reproducibility was good. Energy-resolved time-of-flight (ER-TOF) spectra, obtained using this method of sample preparation and a fixed laser pulse-energy close to the threshold, clearly indicated that there was variation in the peak intensities, which was interpreted as being a variation in the surface concentration of the sample. The four spectra of bovine insulin in figure 4.1.3.(1) were obtained at the same laser irradiance with different sample loadings from the same analyte solution. Figure 4.1.3.(1) shows the energy-resolved time-of-flight (ER-TOF) spectra of bovine insulin using 3-nitrobenzyl alcohol (NBA) as matrix. For the above spectra an accelerating potential of 8064 V was used and the ions were detected using 30 kV post-acceleration. Each of the spectra represents a different sample loading and is the average of 180 laser-shots on the particular sample. A variation in the analyte peak intensity can be observed in the above spectra. The reproducibility of the ER-TOF spectra was improved with the variation in the analyte peak intensity being much smaller, when sample solutions were prepared by mixing 0.5 ml of

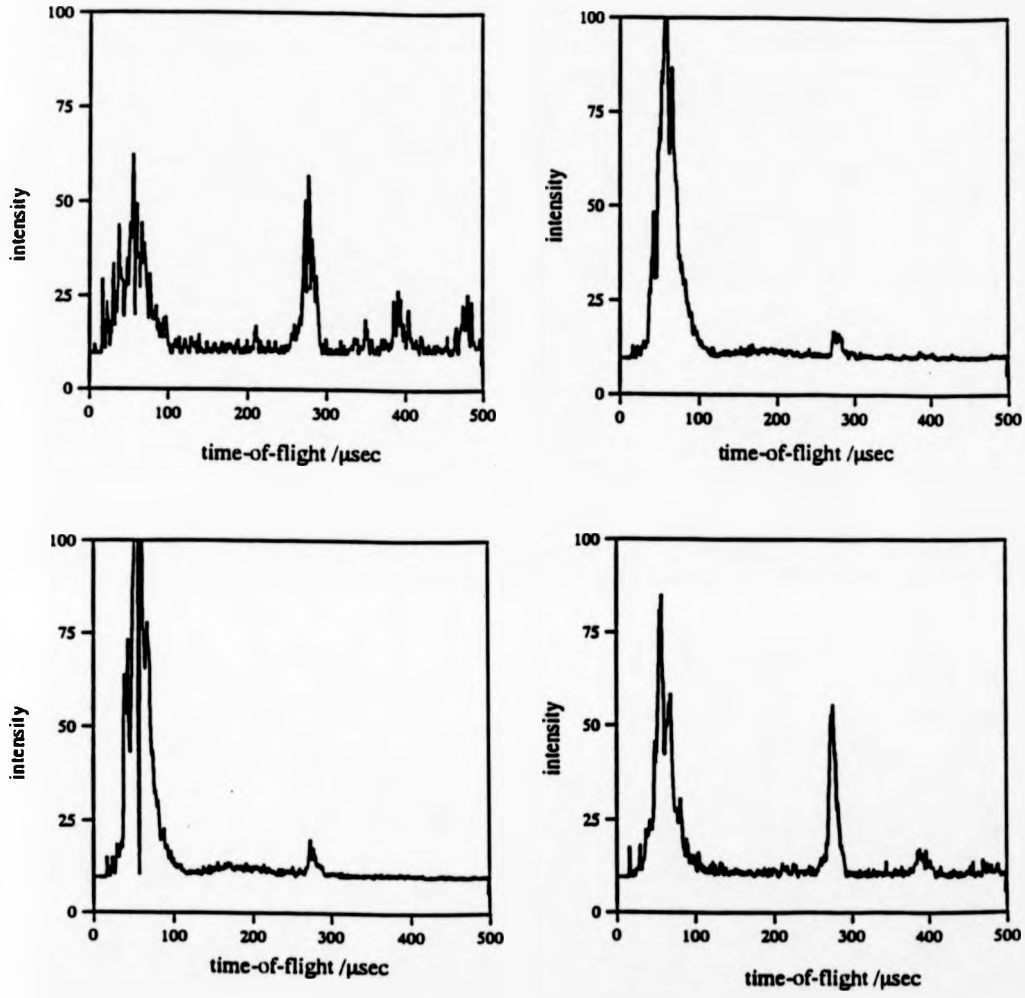


**Figure 4.1.3.(1)** Time-selected energy resolved spectra of bovine insulin. Shot-to-shot inconsistency due to sample preparation.

$1x10^{-5}$ M aqueous analyte solution with 0.5 ml of NBA and dried using a strong stream of nitrogen gas. A sample loading of 1 μl of the prepared sample solution was used. **Figure 4.1.3.(2)** shows how the variation of the analyte peak is much smaller when this method is used. For each of these four spectra, different sample loadings from the same matrix/analyte solution were used and the same laser irradiance was used for all the spectra.

## 4.2 ENERGY-RESOLVED TIME-OF-FLIGHT (ER-TOF) EXPERIMENTS WITHOUT COLLISION GAS

### 4.2.1 Experimental results

The energy-resolved time-of-flight (ER-TOF) experiments were carried out with three different molecular-mass proteins: bovine insulin (5736 Da), β-lactoglobulin (18300 Da) and bovine albumin (66500 Da). An accelerating potential of 8064 V was used throughout. A high transmission grid was placed 2 mm above the sample in order to define a field-free region and reduce the energy spread caused by strong electric fields above the target. The pressure in the ion source of the instrument was $1x10^{-6}$ mbar and in the rest of the instrument $1x10^{-7}$ mbar. The samples were prepared by mixing 0.5 ml of $1x10^{-5}$ M analyte solution with 0.5 ml of NBA and dried under a strong stream of nitrogen gas. The ions were detected using a post-acceleration potential of -30 kV on the on-axis detector located after the electric sector of the instrument. The wavelength used for desorption/ionisation was 266 nm and the intensity of the laser was in near-threshold conditions for ion production. In **figure 4.2.1.(1)**, a 3-D plot of ER-TOF spectra for 3-NBA / β-lactoglobulin is shown. The ions are all positively charged.

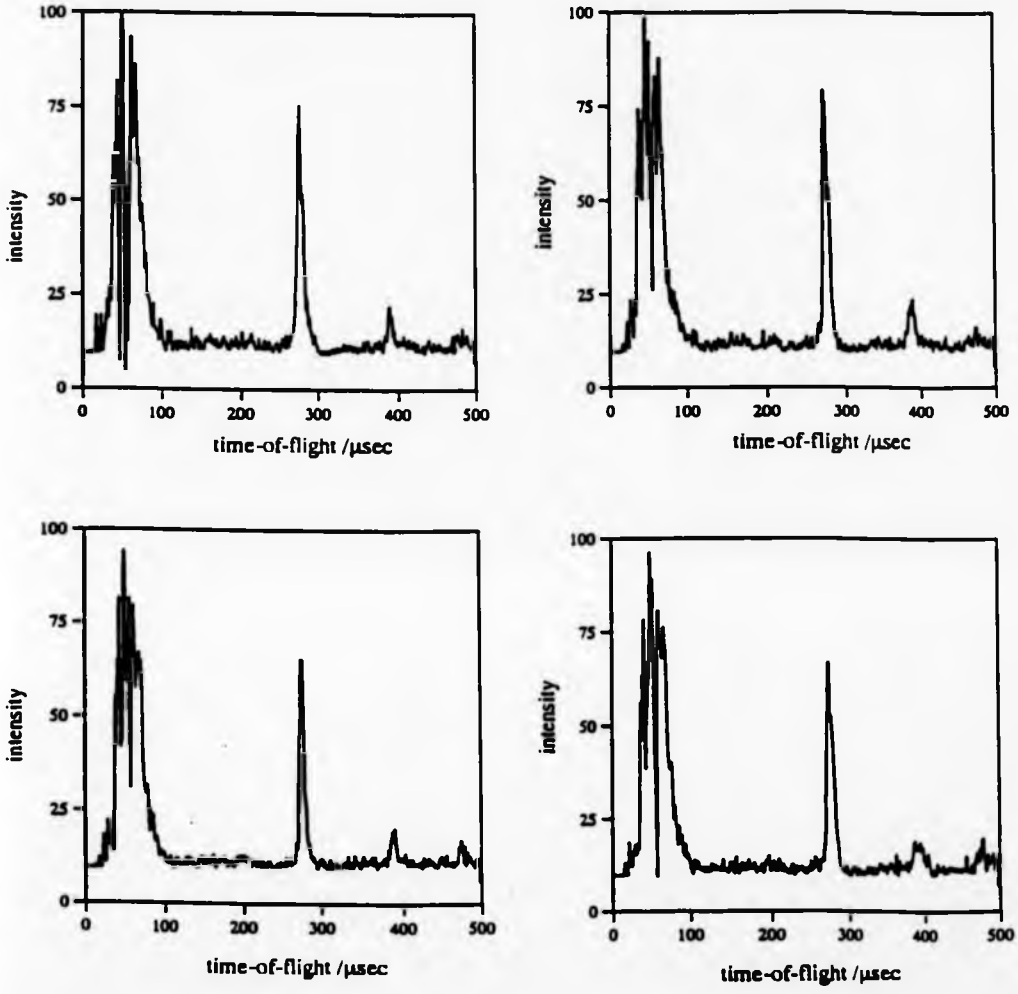


**Figure 4.1.3.(2)** Time-selected energy-resolved spectra of bovine albumin. Improved sample preparation method.

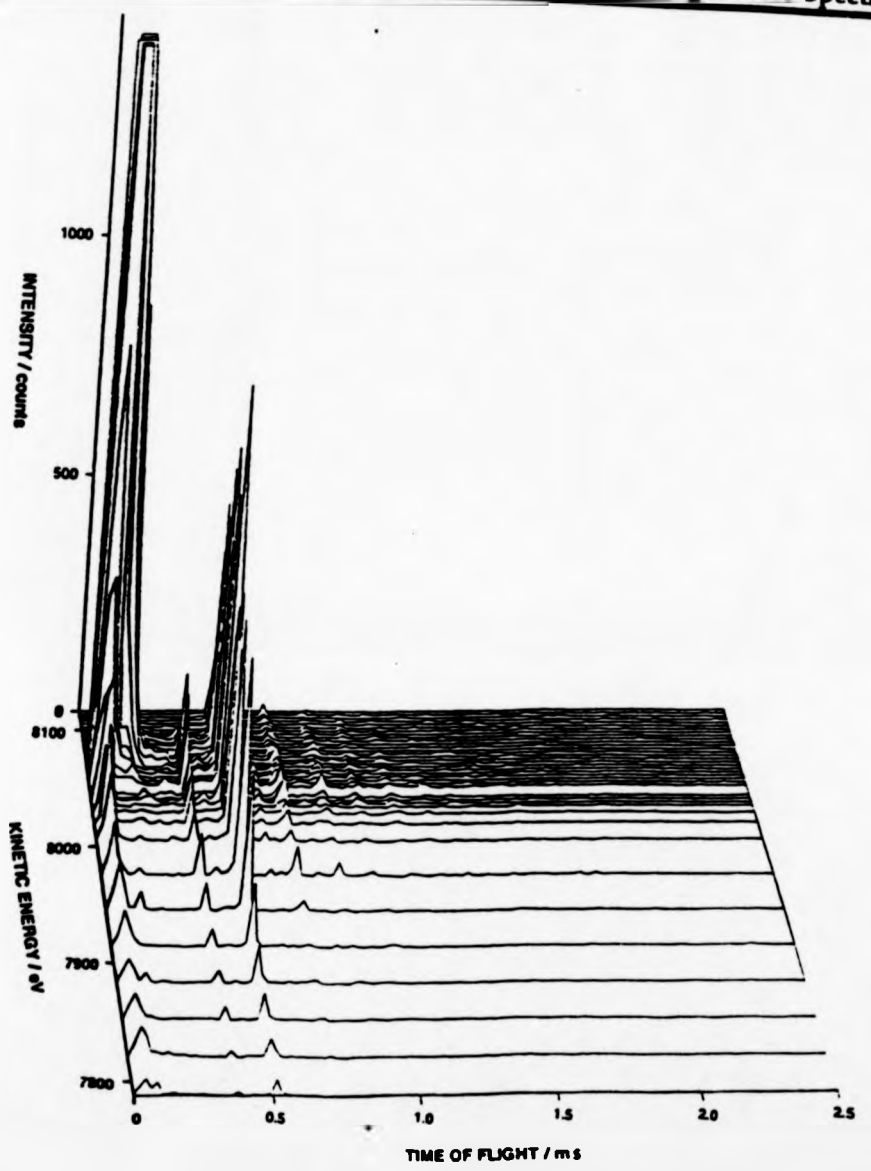


**Figure 4.2.1.(1)** 3-D plot of energy-resolved time-of-flight spectra for 3-NBA / β-lactoglobulin at 8064 V accelerating potential.

Kinetic energy in eV is plotted on the x-axis, time-of-flight of the ions is plotted on the y-axis and intensity of ion peaks in term of ion counts is plotted on the z-axis. Slicing through various zy planes, time-of-flight information for ions of specific kinetic energy is provided. The zx planes provide kinetic energy information for specific times-of-flight. The intensity of the singly charged 3-NBA molecule-ion peak is shown partly saturated on the plot to allow the observation of the smaller peaks such as the dimer, trimer and the doubly charged β-lactoglobulin molecule-ions.

Figures 4.2.1.(2) (a) and (b) show the time-selected energy-resolved (TSER) spectrum of the positively charged molecule-ion of bovine insulin and the TSER spectra of dimer and trimer ions. In figure 4.2.1.(3a), the TSER spectrum of the molecule-ion region of β-lactoglobulin is shown. Doubly and triply charged ions, as well as the dimer of the β-lactoglobulin molecule, were also observed (figure 4.2.1.(3b)). The TSER spectra of bovine albumin are shown in figures 4.2.1.(4) (a), (b) and (c). In addition to the singly charged molecule-ion, doubly, triply, quadruply and pentaply charged ions as well as a singly charged dimer, were observed.

### 4.2.2 DISCUSSION

The velocity of the bovine insulin ions can be calculated from figure 4.2.1.(2a). The time-selected energy-resolved (TSER) spectrum (figure 4.2.1.(2a)) of bovine insulin shows that the energy peak of the molecule ion of bovine insulin is shifted 14 eV towards high energies. The 14 eV initial energy can be interpreted as an initial velocity of 700 m/sec for an ion of 5736 Da. The above velocity is close to the findings of other workers about the velocity of the porcine insulin

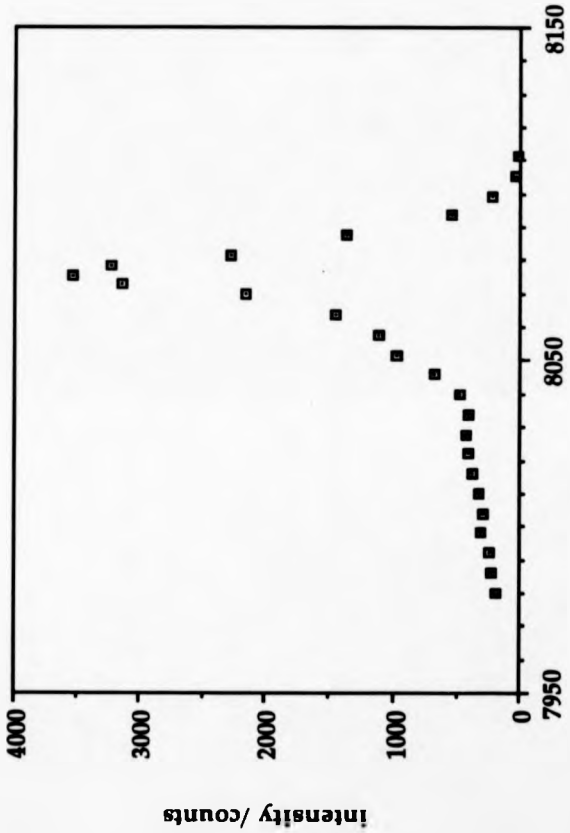


**Figure 4.2.1.(2a)** Time-selected energy-resolved (TSER) spectrum of bovine insulin (singly positively charged molecule-ion)

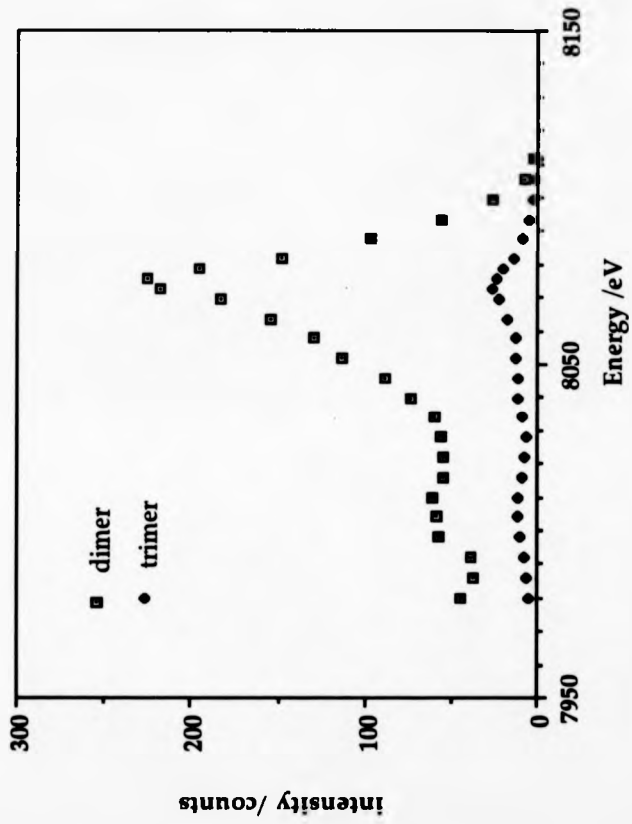


**Figure 4.2.1.(2b)** Time-selected energy resolved (TSER) spectrum of bovine insulin (singly charged dimer and trimer)

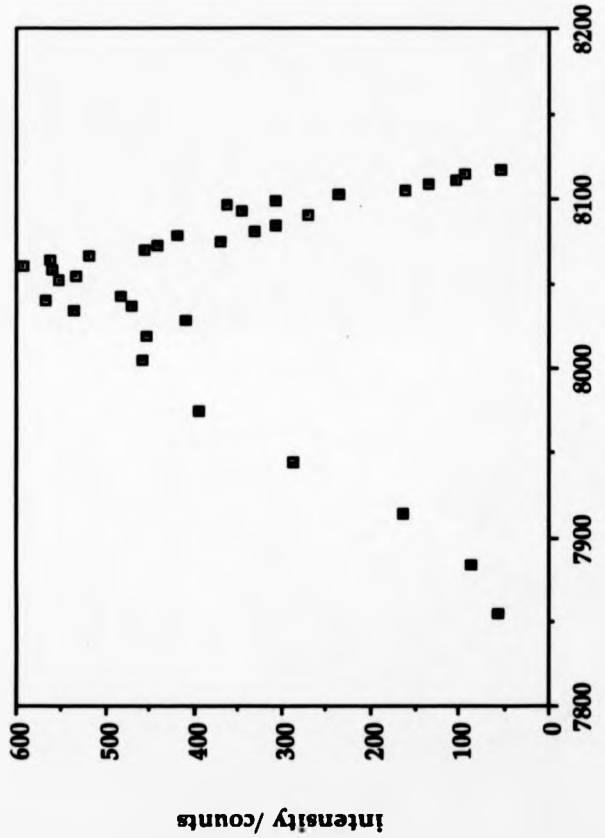


**Figure 4.2.1.(3a)** Time-selected energy-resolved (TSER) spectrum of β -lactoglobulin (singly positively charged molecule-ion).

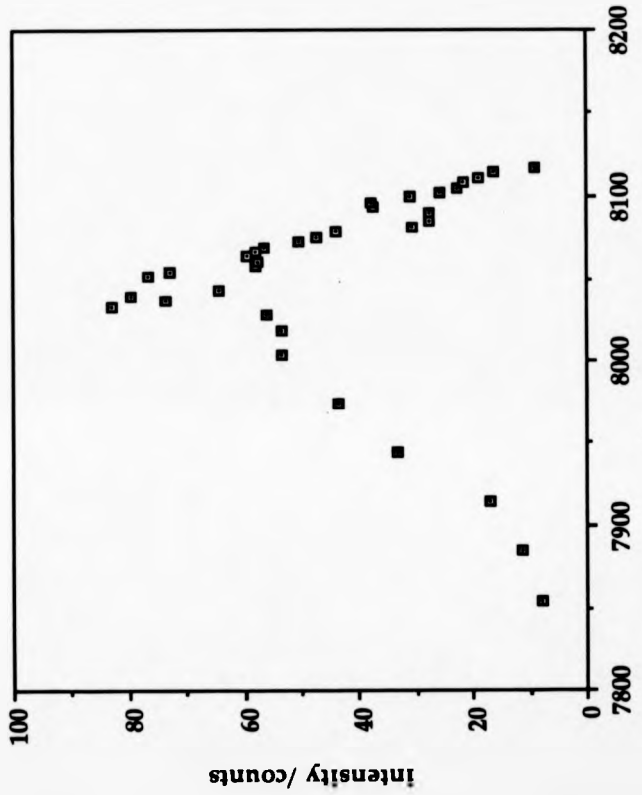


**Figure 4.2.1.(3b)** Time-selected energy resolved (TSER) spectrum of β -lactoglobulin (dimer).

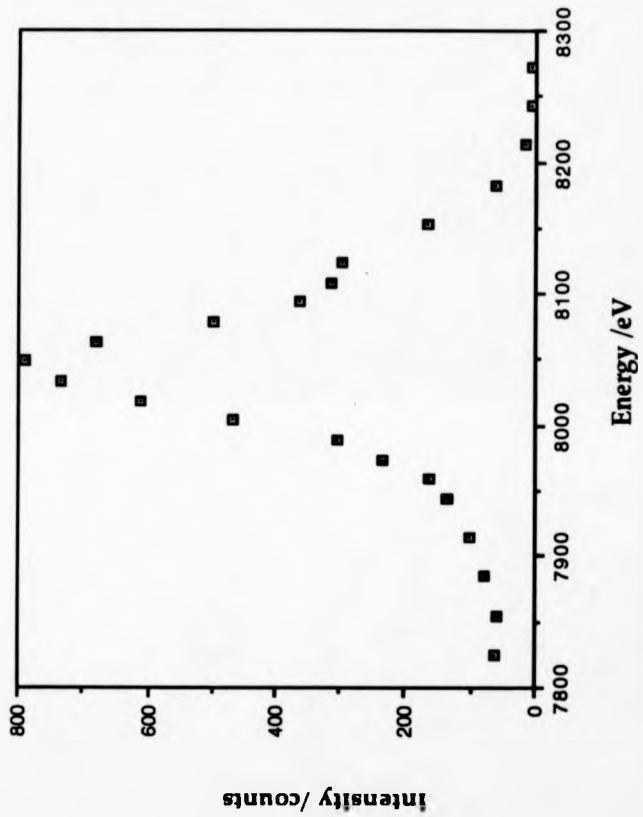


**Figure 4.2.1.(4a)** Time-selected energy resolved (TSER) spectrum of bovine albumin (singly positively charged molecule-ion).

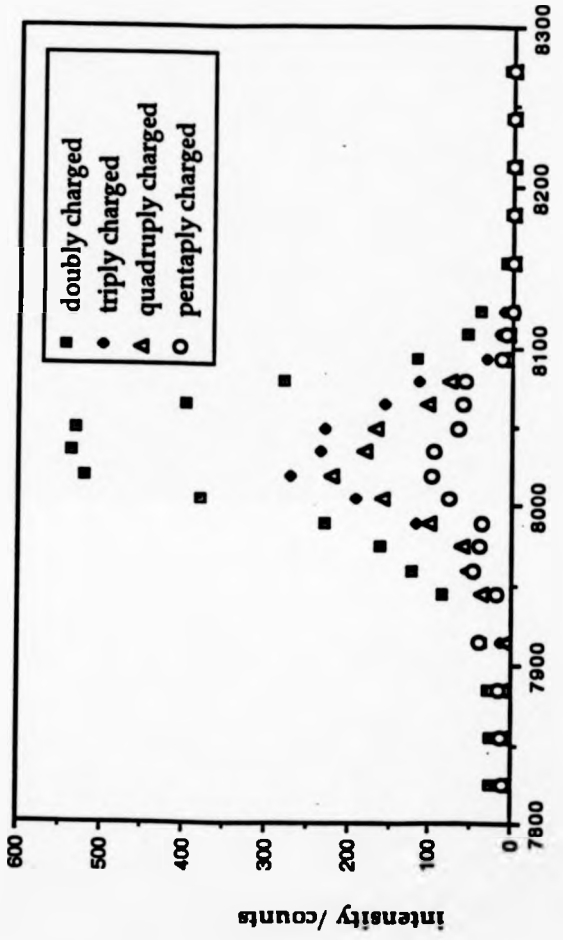


Figure 4.2.1.(4b) Time-selected energy resolved (TSER) spectrum of bovine albumin (doubly, triply, quadruply and pentaply charged ions)

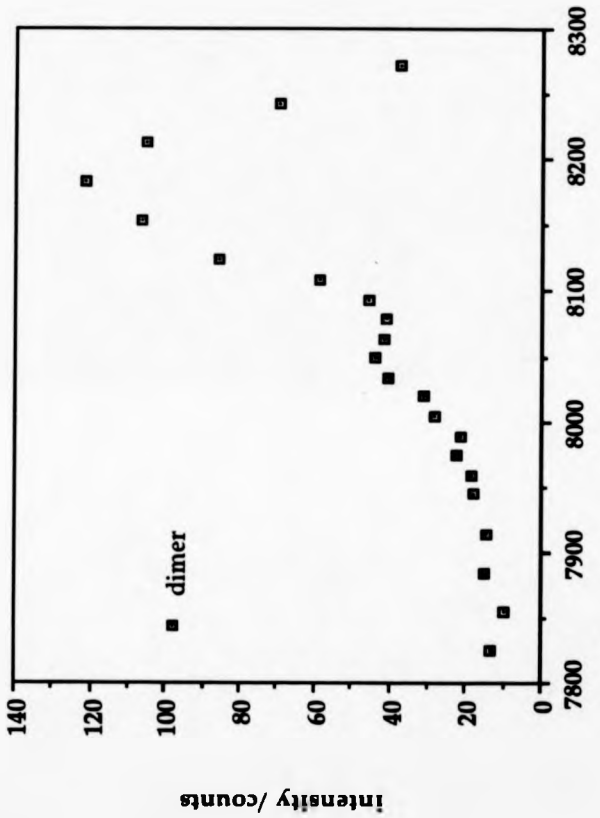


**Figure 4.2.1.(4c)** Time-selected energy resolved (TSER) spectrum of bovine albumin (dimer)

ion (5730 Da), where an average velocity of 750 m/sec was measured[158] with a velocity resolution of approximately 1% and using sinapic acid as matrix.
Mass spectra of proteins reported in the literature in the very high mass region have degraded mass resolutions. With time-of-flight instruments, resolutions are very often not higher than 50 in the range above 100 000 Da. Considering the TSER spectra reported here, there is some additional energy broadening of the molecule-ion peak in the TSER spectrum of bovine albumin (**figure 4.2.1.(4a)**) compared to the molecule-ion peak of bovine insulin (**figure 4.2.1.(2a)**). The energy broadening is interpreted in terms of fragmentation of the molecule ions. This small spread in energy is sufficient to give rise to time dispersion and reduce the mass resolution of a linear time-of-flight mass spectrometer.

The TSER spectra (**Figures 4.2.1.(3)-4.2.1.(4)**), all show apparent broadening of the molecule-ion peaks. Moreover, the magnitude of this apparent broadening increases with molecule-ion mass. This may be understood as a mass-dependent instability in the molecule-ion that gives rise to increasing levels of fragmentation during flight through the spectrometer. In other words a mass-dependent metastability is observed. The molecule-ions of β-lactoglobulin and bovine albumin (**figures 4.2.1.(3a) and 4.2.1.(4a)**) seem to have undergone extensive fragmentation. This effect was apparent even under threshold conditions in the MALDI process, although fragment ions produced during the desorption-ionisation process were not observed. This finding is in agreement with Spengler et al[159], who have reported similar effects in a range of substances of lower mass (1100 - 13000 Da) using a two-stage reflectron TOF instrument. The cause of the decay is not clear. One possibility is collisionless unimolecular dissociation[160] on a time-scale comparable with the ion's time-of-flight. The

energy necessary for the unimolecular dissociation could be possibly obtained by direct absorption of the ultraviolet photons by the analyte ions, thermal energy transferred from the matrix solution to the analyte molecule during desorption or collisions with matrix molecules at the high-pressure desorption region. Alternatively, there may be collisional activation of the ion by residual gas in the instrument[161,162].

## 4.3 ENERGY RESOLVED TIME-OF-FLIGHT (ER-TOF) COLLISION EXPERIMENTS

### 4.3.1 Experimental results

The energy-resolved time-of-flight (ER-TOF) experiments reported below were carried out with bovine insulin (5736 Da) as analyte and 3-NBA as matrix. Xenon, argon and helium were used as collision gases. An accelerating potential of 8064 V was used throughout. The flux of the collision gas was controlled via a variable leak valve (series 203 Granville-Phillips Co.) and the pressure in the collision cell was constant throughout the experiment. The pressure readings from the ion gauge were corrected for each collision gas; all collision experiments were carried out under the same pressure in the collision cell ( $4.7 \times 10^{-5}$ mbar ). The conversion factor for the collision gases used in this experiment are presented in the following table

| collision gas | conversion factor |
|---|---|
| HELIUM | 0.18 |
| ARGON | 1.4 |
| XENON | 2.7 |

The pressure was corrected according to the formula :

*(corrected pressure) = (indicated pressure) / (conversion factor)*

Figure 4.3.1.(1) shows the time-selected energy resolved (TSER) time-of-flight mass spectrum of the molecule ion of bovine insulin without collision gas. The pressure was $1x10^{-6}$ mbar in the ion source and $1x10^{-7}$ mbar in the rest of the instrument. Figure 4.3.1.(2) shows the TSER spectrum of the molecule ion of bovine insulin with helium collision gas. Figure 4.3.1.(3) shows the TSER spectrum of the molecule ion of bovine insulin with argon collision gas and figure 4.3.1.(4) shows the TSER spectrum of bovine insulin with xenon collision gas. For the experiments with collision gases, a liquid nitrogen trap was used in order to ensure low pressure at the flight tube. The pressure during these experiments was $4x10^{-7}$ mbar in the ion source and $4x10^{-8}$ mbar in the rest of the instrument. The spectra with helium, argon and xenon collision gas represent approximately 40% transmission of the molecule ion in each case.

### 4.3.2 Discussion

An important consideration in interpreting the results is the number of collisions the protein ion has undergone. In previous work Neumann et al.[163] and Kim[164] have used the Poisson distribution to calculate the probability of different number of collisions occurring between the ion and the collision gas. The probability P of x number of collisions occurring can be described using Poisson distribution function

$$P(x) = [ \lambda^x e^{-\lambda} ] / x!$$

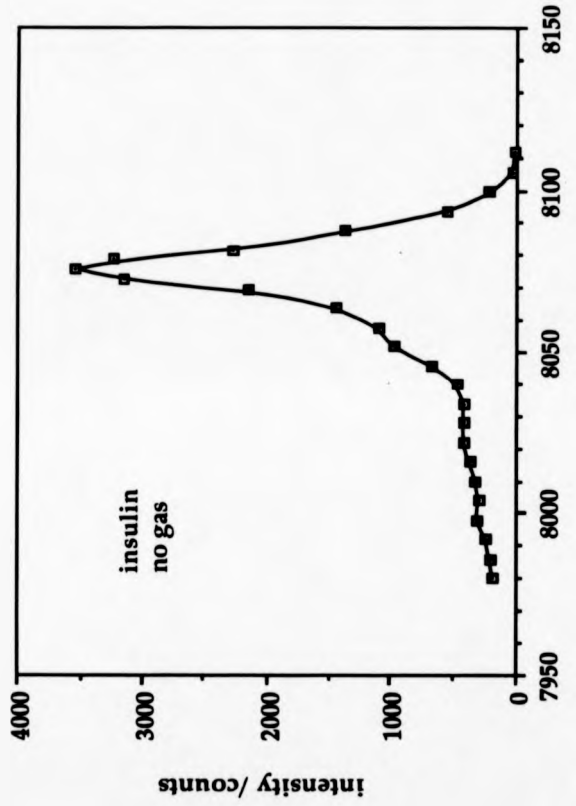


**Figure 4.3.1.(1)** Time-selected energy resolved (TSER) spectrum of bovine insulin (singly positively charged molecule ion) without collision gas.

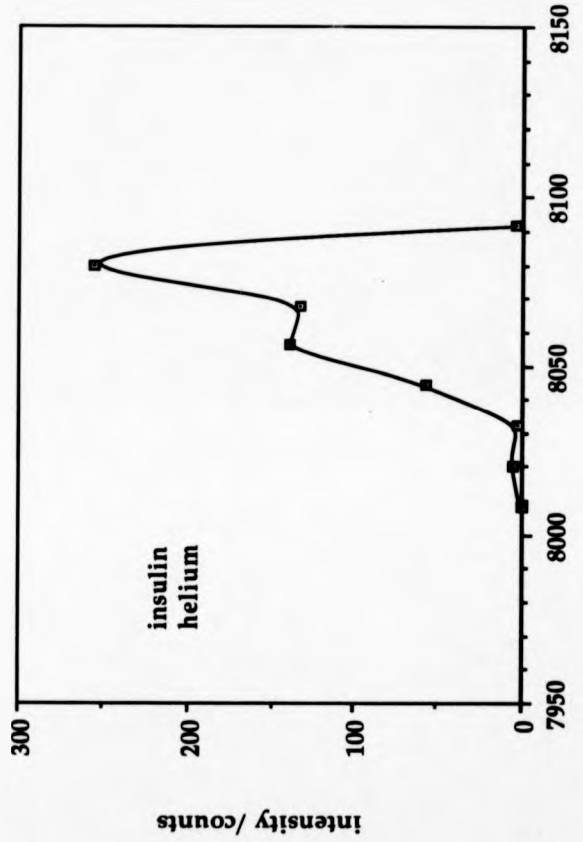


**Figure 4.3.1.(2)** Time-selected energy resolved (TSER) spectrum of bovine insulin with helium collision gas

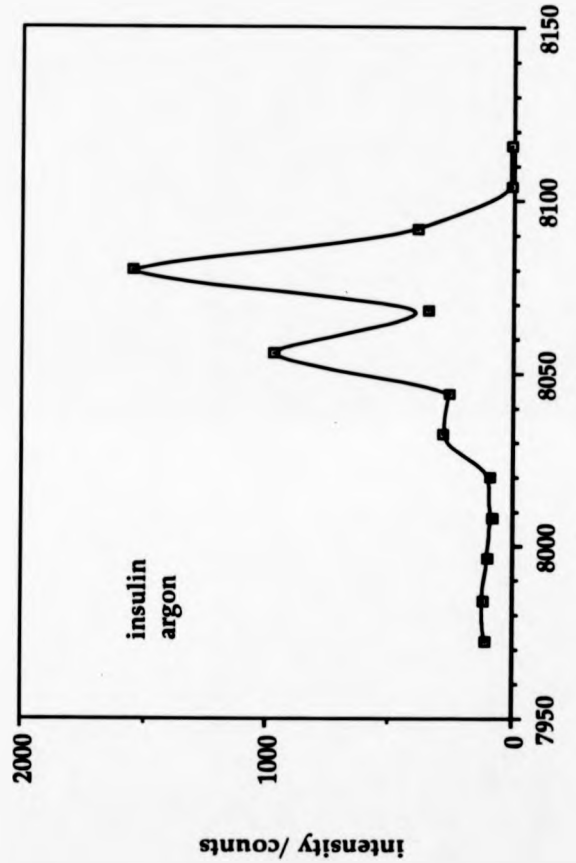


**Figure 4.3.1.(3)** Time-selected energy resolved (TSER) spectrum of bovine insulin with argon collision gas.

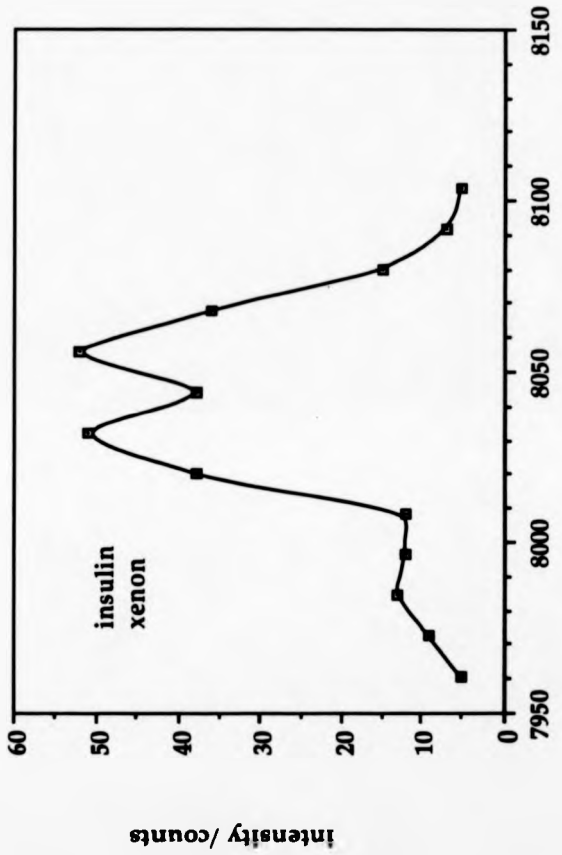


**Figure 4.3.1.(4)** Time-selected energy resolved (TSER) spectrum of bovine insulin with xenon collision gas.

where λ is the mean number of collisions occurring for a given transmission. The values of λ for transmissions of 0.1 to 0.9 are given in figure 4.3.2.(1).

In order to have another means of probing the question of the number of collisions, the physical dimensions of the bovine insulin molecule were evaluated from crystallographic data. A collision cross section was roughly estimated using the physical dimensions of the bovine insulin ion and the collision gas. A three dimensional representation of the bovine insulin and 3-NBA molecules is presented in figure 4.3.2.(2). The mean free paths were calculated assuming that the collision gas atoms have velocities which are relatively small compared with the velocity of the ions. The formula used to calculate the mean free path[165] was

$$L = \frac{1}{\sqrt{2}\pi\sigma^2 N}$$

where $L$ is the average distance between collisions, $N$ is the number of molecules per unit volume and $\sigma$ is the cross section. When one molecule is of diameter $\sigma_1$ and the other molecule of diameter $\sigma_2$, a cross section can be calculated as $\sigma = (\sigma_1 + \sigma_2)/2$.

The bovine insulin molecule is a molecule of an average diameter of 30 Å. The diameters of helium, argon and xenon atom are 2.44 Å, 3.82 Å and 4.36 Å respectively[166].

At the collision-gas pressure at which the experiments were carried out ( $4.7 \times 10^{-5}$ mbar), the calculated mean free path for the bovine insulin ion is 75 mm with helium, 69 mm with argon and 67 mm with xenon collision gas. If an interaction distance of 10 Å is taken into account, the mean free path for the bovine insulin ion becomes 28.7 mm for helium, 27 mm for argon and 26 mm for xenon collision gas. The length of the collision cell was 10 mm.

| Transmission | Mean number of collisions , λ |
|---|---|
| 0.04 | 3.21 |
| 0.1 | 2.30 |
| 0.2 | 1.61 |
| 0.3 | 1.20 |
| 0.4 | 0.91 |
| 0.5 | 0.69 |
| 0.6 | 0.51 |
| 0.7 | 0.36 |
| 0.8 | 0.22 |
| 0.9 | 0.10 |

**Figure 4.3.2.(1)** Average number of collisions occuring at a given transmission calculated using the Poisson function.

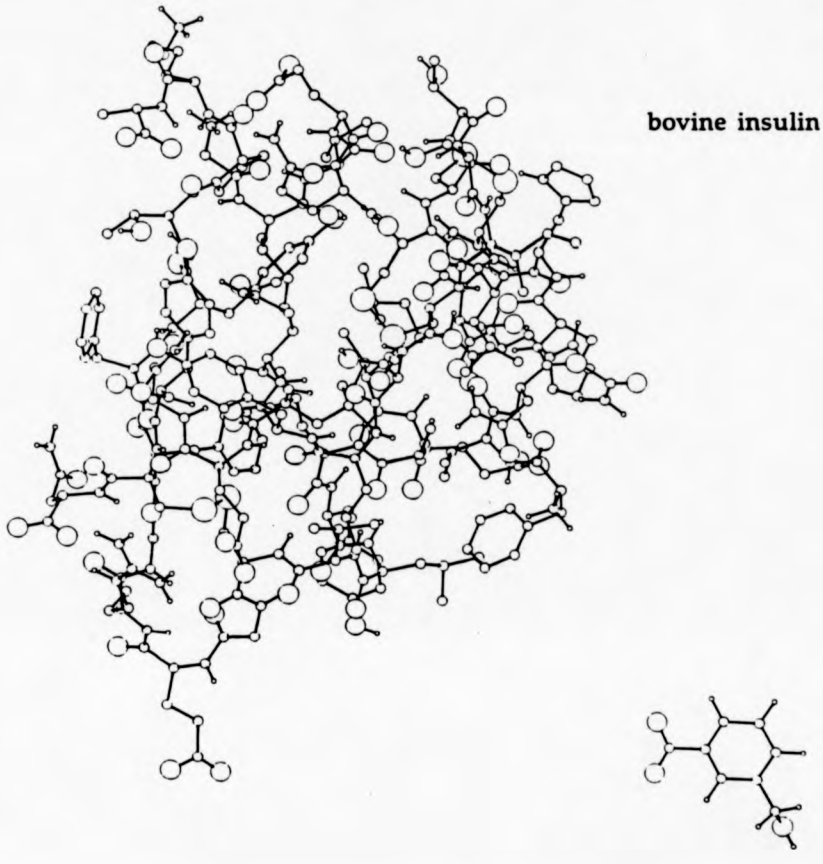


**Figure 4.3.2.(2)** **A three dimensional representation of the bovine insulin and the 3-nitrobenzyl alcohol molecules.**

The TSER spectra of bovine insulin when collision gases are used show additional broadening, when compared with the TSER spectrum without collision gas. The TSER spectrum with xenon collision gas is broader than the TSER spectrum with argon collision gas, and the TSER spectrum with argon collision gas is broader than the TSER spectrum with helium collision gas. In the cases of xenon and argon collision gas, another peak at lower energy appears in the TSER spectra when collision gas is used. In the case with helium a shoulder at lower energy appears in the TSER spectrum In each case the additional peak is 24 eV lower in energy than the main peak and would correspond to loss of a small fragment.

### 4.4 Conclusion

It has been shown, by the time-selected energy resolved (TSER) time-of-flight spectra of β-lactoglobulin and bovine albumin, that there is a source of peak broadening in a time-of-flight instrument resulting from the lack of stability of high-mass ions during their flight through the time-of-flight mass spectrometer. It has been shown that a substantial number of ions decay after acceleration and prior to detection, even under threshold conditions of laser irradiation. Two factors may contribute to some extent to the observed fragmentation: (a) high internal energy of protein ions formed by MALDI with the more massive ions possessing higher energies, (b) collisional activation of the massive ions by the background gases[163]. It has been shown that insulin ions exhibit additional peak broadening as a result of collision with helium, argon and xenon.

# CHAPTER 5

## CHARGE EXCHANGE IN LARGE IONS

### 5.1 INSTRUMENTATION

The time-of-flight system used for these experiments was located in the second field-free region of the large-scale reverse geometry double focusing mass spectrometer (figure 5.1.(1)). Within the ion source, the ions after being accelerated were focused and steered by an einzel lens and an astigmatic lens system. Astigmatic focusing was required in order to achieve maximum transmission through the 2 mm wide and 8 mm high slits of the collision cell. Between the source and the collision cell there was an 1.8 m field-free region.. Having passed through the collision cell, the ions were accelerated through a further 25 kV with an off-axis post-acceleration detector (PAD). The ions struck the conversion dynode of the post-acceleration detector (PAD), producing electrons which in turn were detected with an ETP electron multiplier operating at 2 kV. The 90° off-axis position of the post-acceleration detector (PAD) ensured that only positively charged species struck the conversion dynode and produced electrons (figure 5.1.(2)). The signal produced was recorded with a LeCroy 7200A digital oscilloscope. The flux of the collision gas was controlled via a variable leak valve (series 203 Granville-Phillips Co.) and the pressure maintained constant throughout the experiment. The pressure gauge readings were corrected for each collision gas employed, and all collision experiments were carried out

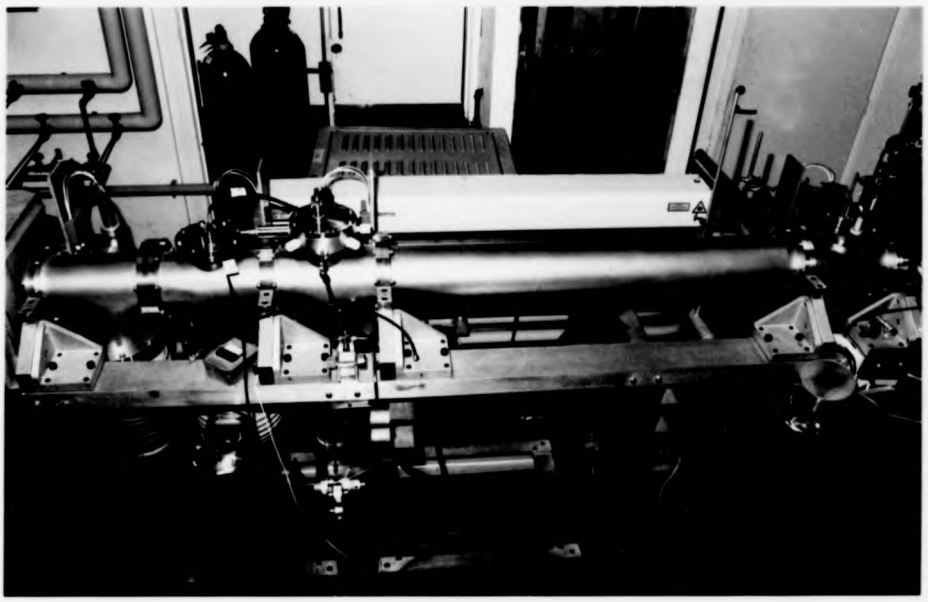

**Figure 5.1.(1)** Photograph of the time-of-flight instrument located in the second field-free region of the large-scale reverse geometry mass spectrometer.

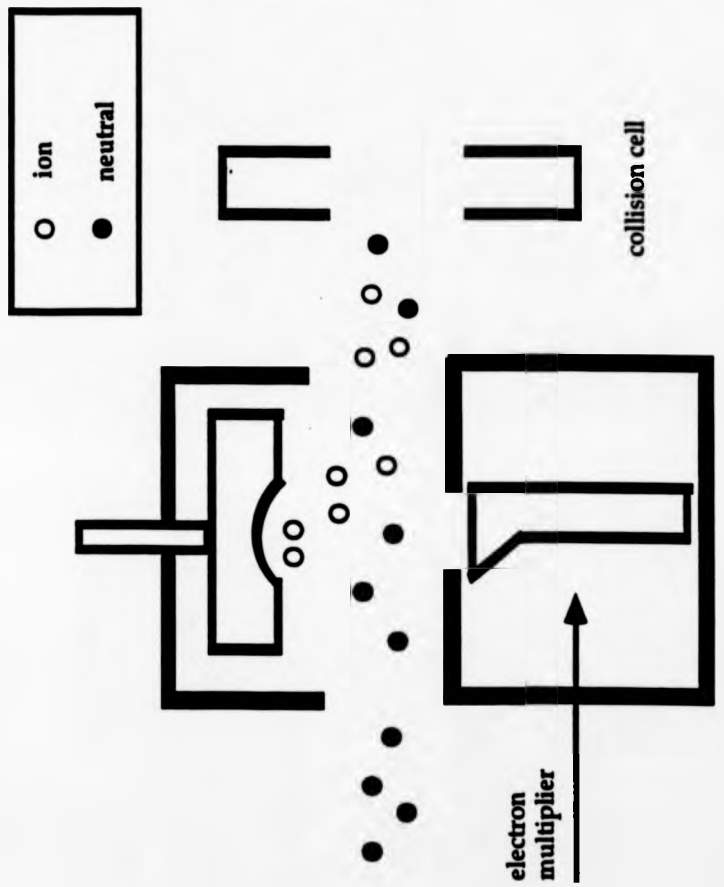


**Figure 5.1.(2)** Post-acceleration detector for the charge exchange experiment

under the same pressure ( 4.7 x $10^{-5}$ mbar). The conversion factors for the collision gases used in this experiment are presented in the following table:

| collision gas | conversion factor |
|---|---|
| He | 0.18 |
| NO | 1.4 |
| Ar | 1.4 |
| Xe | 2.7 |

The pressure was corrected according to the formula :

*(corrected pressure) =(indicated pressure) / (conversion factor)*

The conversion factors for helium, argon and xenon were obtained from Edwards[167] and were used previously by Sheil[168]. The value for nitric oxide was provided by Dr J. C. Traeger[169].

A frequency quadrupled Nd-YAG laser operating at 266 nm, focused by a 30 cm focal length spectrasil lens, was used to irradiate the sample at a grazing angle. Liquid 3-nitrobenzyl alcohol (NBA) was used as matrix in order to provide the necessary shot-to-shot reproducibility, long sample lifetime and fast and simple sample preparation. Particular care was taken to ensure the homogeneity of the sample. For the experiments reported below, samples were prepared by

mixing 0.5 ml of $1x10^{-5}$ M analyte solution with 0.5 ml of 3-nitrobenzyl alcohol. The water/methanol mixture used in the analyte solution was removed using a strong stream of nitrogen gas. For each sample loading 1μl of sample was used.

## 5.2 RESULTS

The experiments were carried out using three different molecular-mass molecules: insulin chain B (3496 Da), bovine insulin (5736 Da) and β-lactoglobulin (18300 Da). Xenon, argon, helium and nitric oxide were used as collision gases. Only positive ions have been studied. The kinetic energies of the matrix and analyte ions were in the range between 8060 eV and 3060 eV. For each analyte molecule at a given kinetic energy and for a given collision gas, six spectra were acquired. The mean value and standard deviation of the ratio of the matrix-to-analyte peak intensities were calculated from the six spectra. Each of those six spectra represented the average of 50 laser shots, thus reducing the influence of the fluctuation of the laser energy on the peak heights of the matrix and analyte ion signals. The error bars plotted in the following figures are the standard deviations of the mean values. For each collision gas, a comparison of the ratios of matrix to analyte peaks, for kinetic energies ranging from 8060 eV to 3060 eV, without collision gas to those with collision gas is presented. The ratios of the matrix to analyte peaks for β-lactoglobulin and different collision gases are shown in **figure 5.2.(1a)**, **figure 5.2.(1b)** and **figure 5.2.(1c)**. In **figure 5.2.(1a)** the two different sets of points represent the ratio of matrix to analyte without collision gas and the ratio of matrix to analyte with argon collision gas. In **figure 5.2.(1b)** one set of points represents the ratio of matrix to analyte without collision gas and the other the ratio of matrix to analyte with nitric oxide as the collision gas.

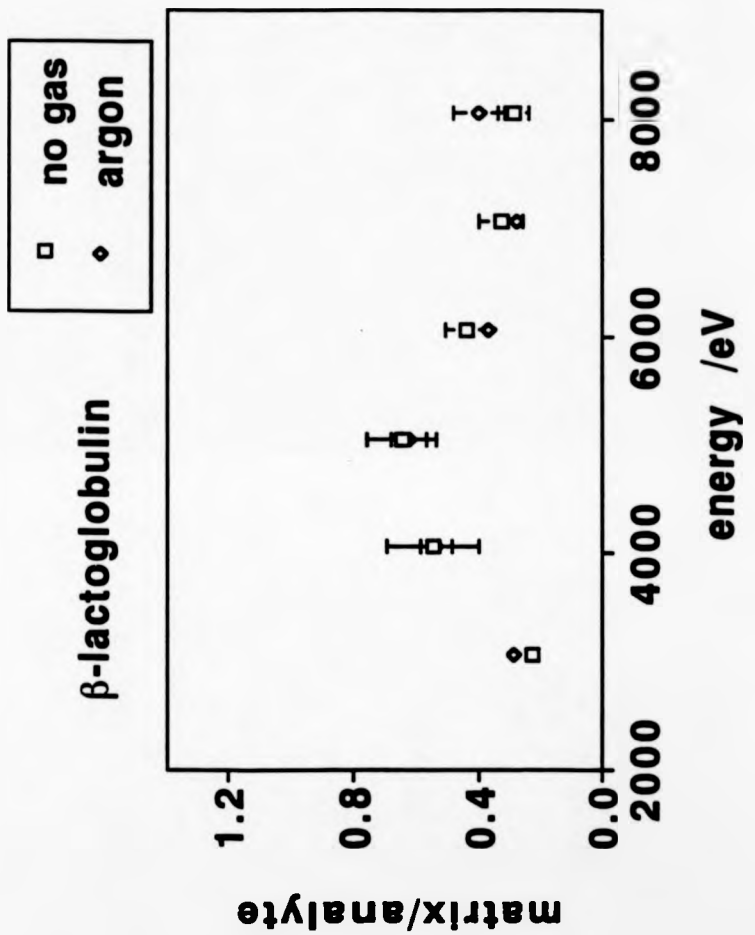
β-lactoglobulin
no gas
argon
matrix/analyte
1.2
0.8
0.4
0.0
2000
4000
6000
8000
energy /eV

Figure5.2.(1a)

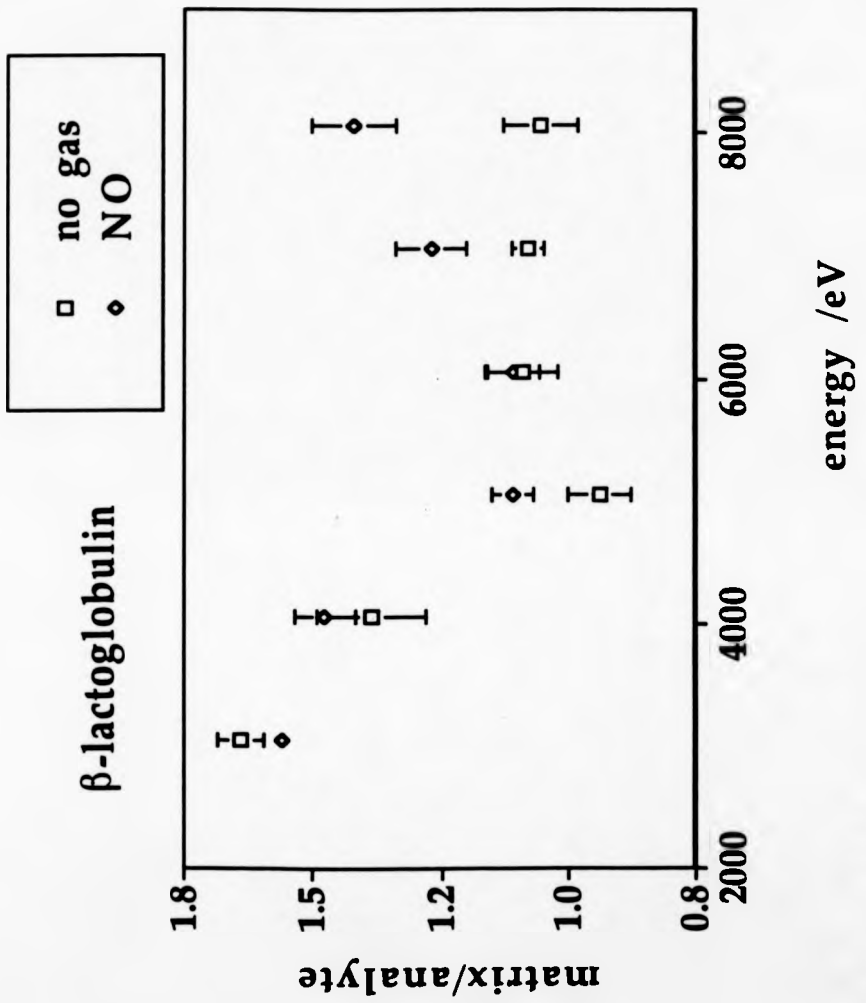
β-lactoglobulin
no gas
NO
matrix/analyte
1.8
1.5
1.2
1.0
0.8
2000
4000
6000
8000
energy /eV

Figure 5.2.(1b)

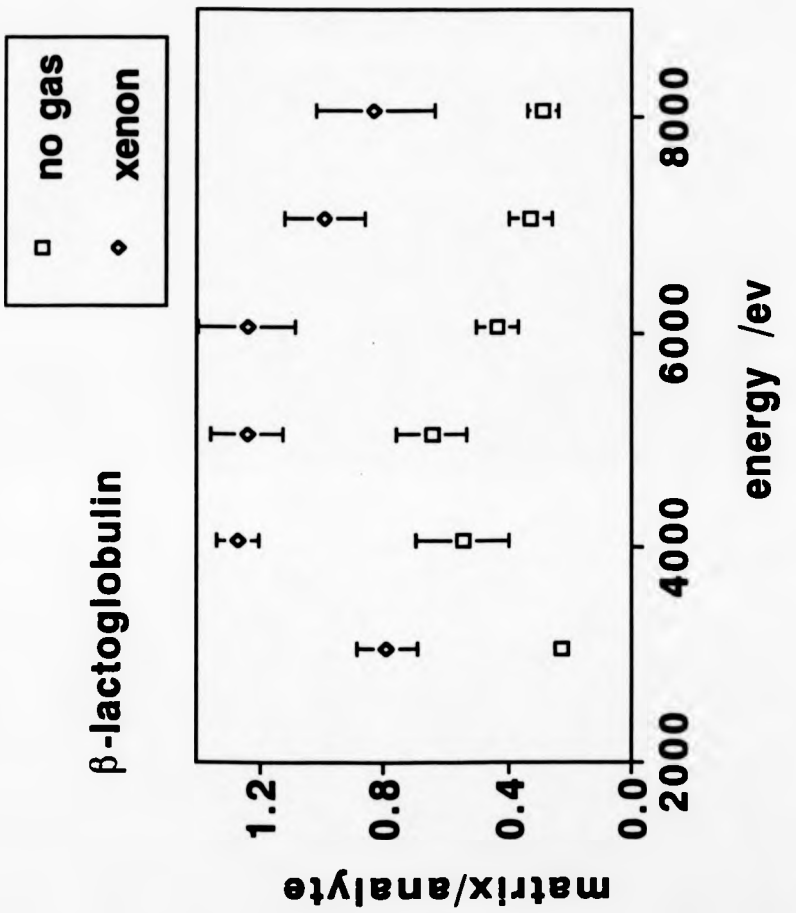
β-lactoglobulin
no gas
xenon
matrix/analyte
0.0
0.4
0.8
1.2
2000
4000
6000
8000
energy /ev

Figure 5.2.(1c)

In figure 5.2.(1c) one set of points represents the ratio of matrix to analyte without collision gas and the other the ratio of matrix to analyte with xenon as the collision gas. Similar diagrams with matrix to analyte ratios for bovine insulin with the collision gases helium (figure 5.2.(2a)), nitric oxide (figure 5.2.(2b)) and argon (figure 5.2.(2c)) are presented . In figures 5.2.(3a) and (3b) the ratios of matrix to analyte for insulin chain B with helium and argon collision gases are presented.

The above results show a decrease in the intensity of the β-lactoglobulin signal with respect to the matrix signal, when xenon was used as collision gas. When argon was used as collision gas, no change in the intensity of the analyte signal relative to that of the matrix was observed. When nitric oxide was used as collision gas, a decrease in the β-lactoglobulin signal with respect to that of the matrix signal was observed only at the high-energy end of the range of laboratory frame kinetic energies. Only at accelerating potential higher than 7 kV was the β-lactoglobulin signal clearly lower relative to the matrix signal.

When bovine insulin was used, a change in the intensity of the analyte signal relative to that of the matrix was observed when argon was used as collision gas. In the case of helium as collision gas, no change could be observed in the intensity of the analyte signal relative to that of the matrix signal. A change could be observed when nitric oxide was used as collision gas.

With insulin chain B as analyte, there was a change in the intensity of the analyte signal relative to that of the matrix when argon was used as collision gases. Helium as collision gas showed no reduction in the intensity of the analyte signal relative to the matrix signal.

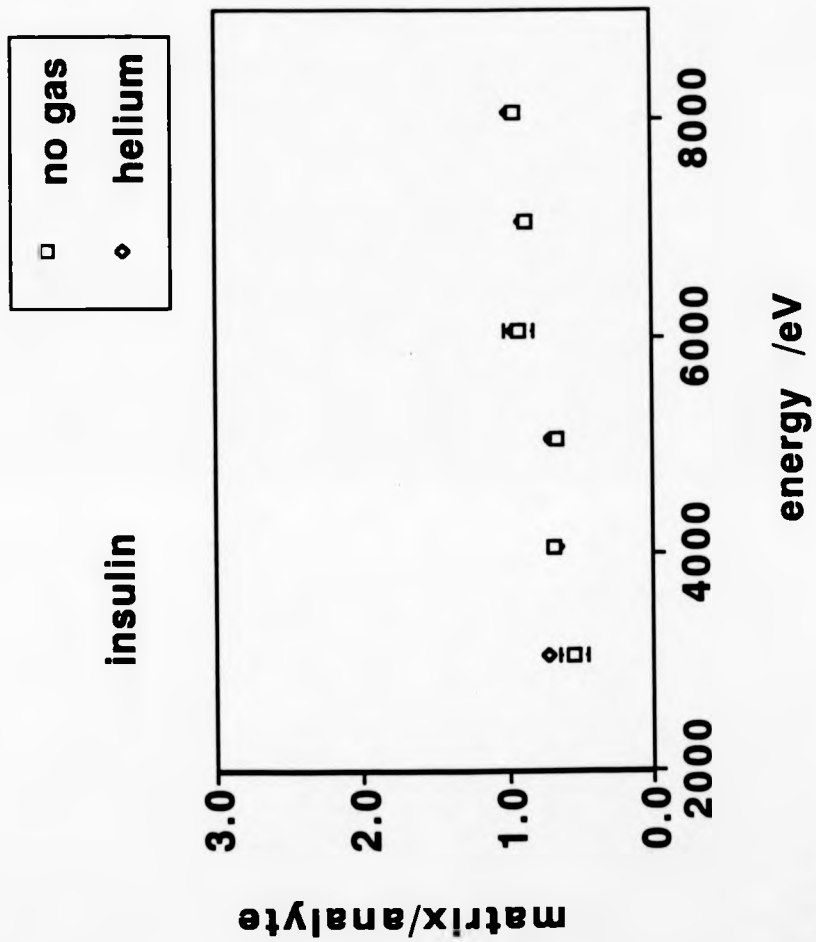
no gas
helium
insulin
matrix/analyte
3.0
2.0
1.0
0.0
2000
4000
6000
8000
energy /eV

Figure 5.2.(2a)

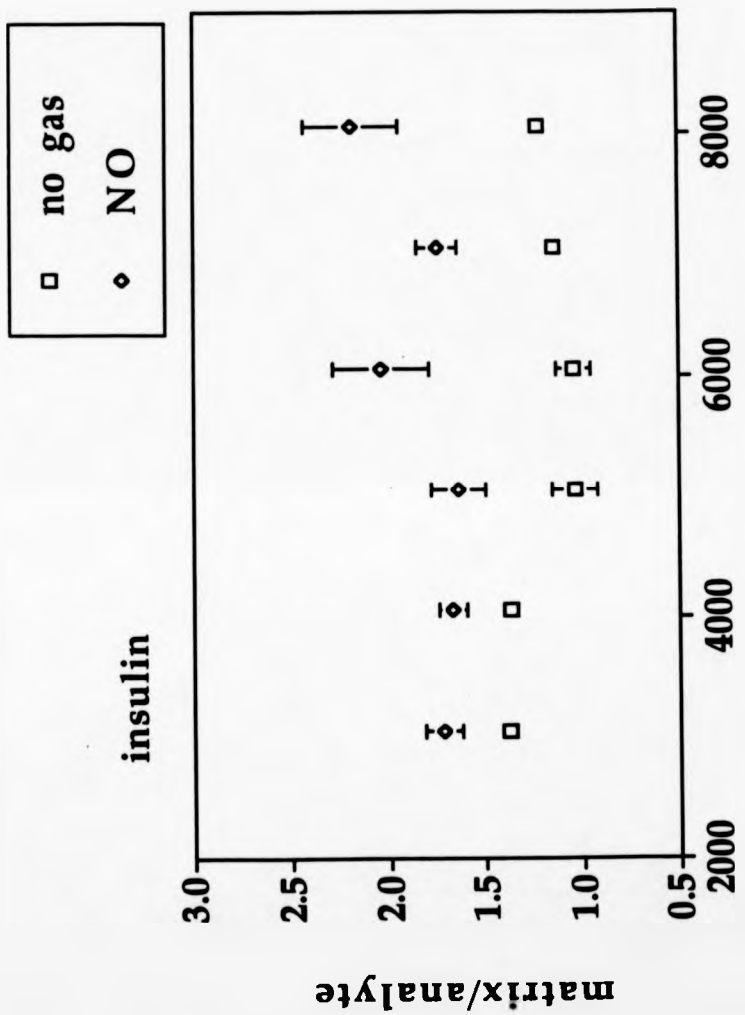
no gas
NO
insulin
matrix/analyte
3.0
2.5
2.0
1.5
1.0
0.5
2000
4000
6000
8000
energy /eV

Figure 5.2.(2b)

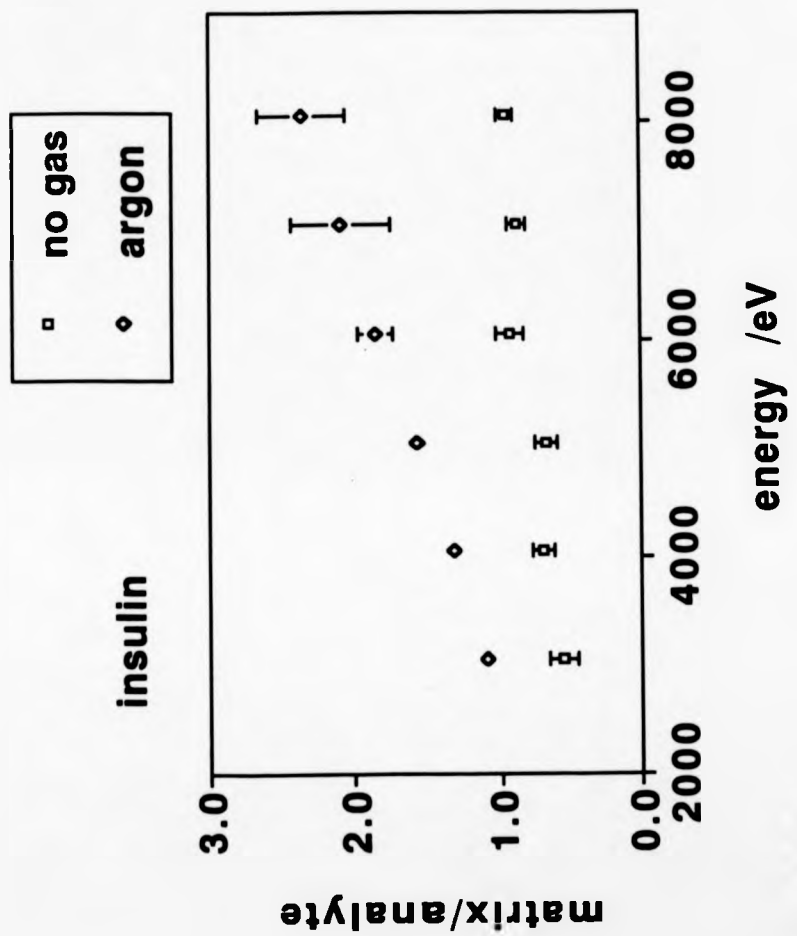
insulin
no gas
argon
matrix/analyte
3.0
2.0
1.0
0.0
2000
4000
6000
8000
energy /eV

Figure 5.2.(2c)

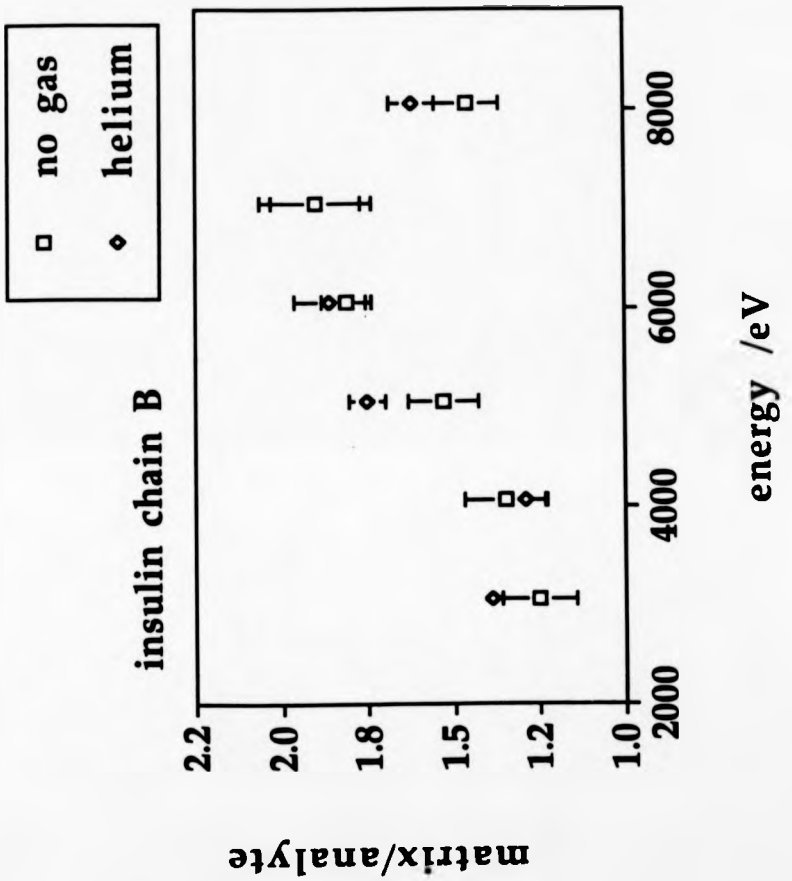
no gas
helium
insulin chain B
matrix/analyte
2.2
2.0
1.8
1.5
1.2
1.0
2000
4000
6000
8000
energy /eV

Figure 5.2.(3a)

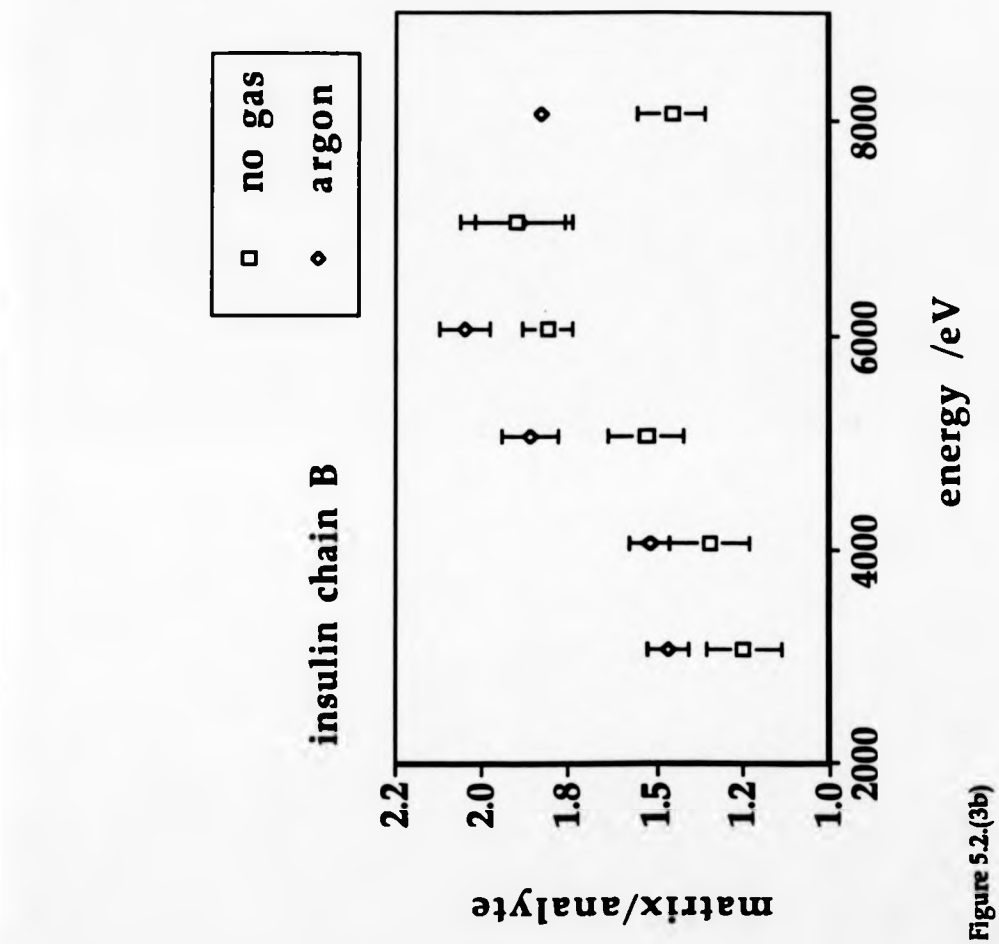
no gas
argon
insulin chain B
matrix/analyte
2.2
2.0
1.8
1.5
1.2
1.0
2000
4000
6000
8000
energy /eV

Figure 5.2.(3b)

In order to establish that the results were not due to ion optical discrimination during the post acceleration or ion scattering after the collision, a number of calculations were carried out. In **figure 5.2.(4)**, the off-axis post-acceleration detector is modelled using the SIMION ion optical simulation program. A number of trajectories were traced for ions with kinetic energies ranging from 3 kV to 10 kV. The potential used for post-acceleration in these calculations was -25 kV. The results suggest that the conversion dynode collects efficiently ions with a kinetic energy ranging from 3 kV to 10 kV, indicating that there should have been no energy discrimination during the post acceleration of the ions.

In order to calculate the scattering angle of the ions after collision with the collision gas, the model of the impulsive collision transfer (ICT) theory[170] was used. The impulsive collision transfer theory assumes that the energy and momentum transfer takes place in a collision between the gas atom and a single atom of the ion. Let $m_a$ be the mass of that particular atom, $m_g$ the mass of the collision gas and $m_{ion}$ the mass of the ion, then the highest scattering angle is given by

$$\theta_{high} = \arcsin(\mu - 1)$$

where $$\mu = \frac{1}{1 - \frac{m_a m_g}{\left[m_{ion}\left(m_a + m_g\right)\right]}}$$

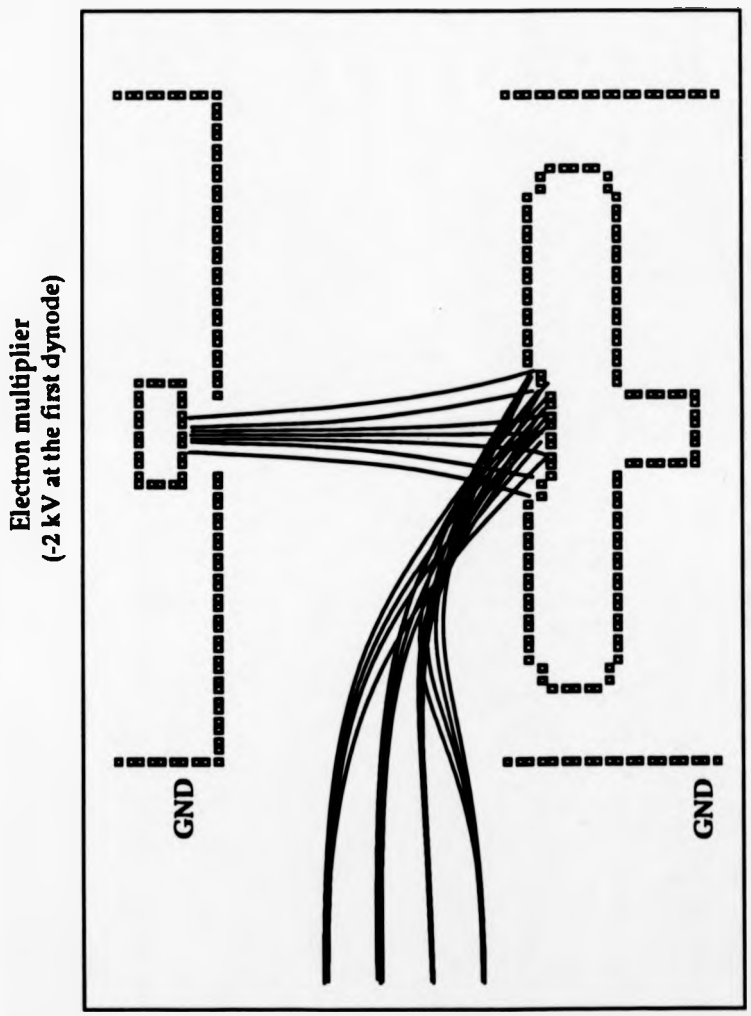


**Figure 5.2.4** Ion trajectory simulations of the off-axis post-acceleration detector (incident ion energy 3-10 kV)

The theory requires knowledge of the mass $m_a$ of the atom hit by the gas atom. Because the ion consists of atoms with different masses, a representative mass or distribution of masses has to be used. As representative masses for $m_a$, the masses of H and C were used. The calculations were carried out for helium (4 Da) argon (40 Da) and xenon (131 Da) collision gases. The resulting scattering angles for 3-nitrobenzyl alcohol (153.14 Da), insulin chain B (3496 Da), bovine insulin (5736 Da) and β-lactoglobulin (18300 Da) are given in figure 5.2.(5). According to the dimensions of the collision cell and the width of the slit used at the exit of the collision cell, ions with scattering angles as large as 6° could be detected. The calculated scattering angles resulting from the collision of the molecule ions with the collision gases were much lower than the maximum acceptance angle with the matrix molecules being scattered more than the analyte molecules.

The centre-of-mass collision energy (CMCE) for β-lactoglobulin has been calculated for xenon, nitric oxide and argon target gas, for the range of laboratory frame kinetic energies used in the experiments (8060 eV - 3060 eV). These centre-of-mass collision energies are presented in figure 5.2.(6). In figure 5.2.(7) the centre-of-mass collision energies (CMCE) for bovine insulin with argon, nitric oxide and helium target gas for the same laboratory frame energy range are shown. In figure 5.2.(8) the centre-of-mass collision energies (CMCE) for insulin chain B and argon and helium collision gases are given. In figures 5.2.(6), (7) and (8), the horizontal axes represent the laboratory frame kinetic energy, while the vertical axes represent the centre-of-mass collision energy. It can be seen that the centre-of-mass collision energy becomes small for a given laboratory frame kinetic energy, when the mass of the analyte ion increases. Heavier collision

| ion | collision gas | $m_a$ | $\theta_{high}$ |
|---|---|---|---|
| NBA | Xenon | H | 0.374074 |
| | | C | 4.439807 |
| | Argon | H | 0.367696 |
| | | C | 3.681234 |
| | Helium | H | 0.301162 |
| | | C | 1.145992 |
| Insulin chain B | Xenon | H | 0.016269 |
| | | C | 0.180732 |
| | Argon | H | 0.015994 |
| | | C | 0.151683 |
| | Helium | H | 0.013114 |
| | | C | 0.049209 |
| Bovine insulin | Xenon | H | 0.009977 |
| | | C | 0.110700 |
| | Argon | H | 0.009881 |
| | | C | 0.092937 |
| | Helium | H | 0.008043 |
| | | C | 0.030171 |
| β-lacto globulin | Xenon | H | 0.003107 |
| | | C | 0.034439 |
| | Argon | H | 0.003055 |
| | | C | 0.028915 |
| | Helium | H | 0.002505 |
| | | C | 0.009394 |

**Figure 5.2.(5)**

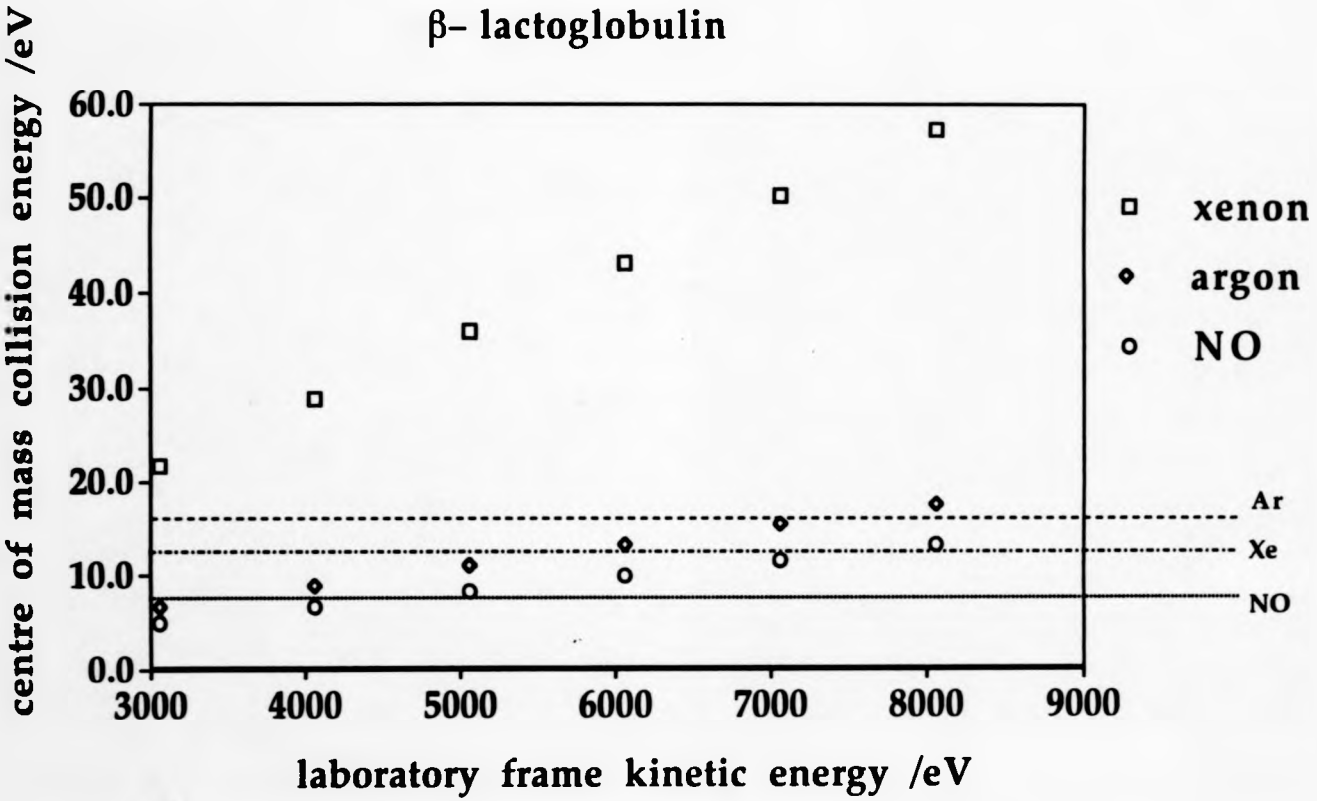
β– lactoglobulin
centre of mass collision energy /eV
60.0
50.0
40.0
30.0
20.0
10.0
0.0
3000
4000
5000
6000
7000
8000
9000
laboratory frame kinetic energy /eV
xenon
argon
NO
Ar
Xe
NO

Figure 5.2.(6)

insulin
NO
argon
helium
He
Ar
NO
centre of mass collision energy /eV
laboratory frame kinetic energy /eV
60.0
50.0
40.0
30.0
20.0
10.0
0.0
3000
4000
5000
6000
7000
8000
9000

Figure 5.2.(7)

insulin chain B
argon
helium
He
Ar
centre of mass collision energy /eV
laboratory frame kinetic energy /eV
100
90
80
70
60
50
40
30
20
10
0
3000
4000
5000
6000
7000
8000
9000

Figure 5.2.(8)

gases are needed in order to obtain high centre-of-mass collision energies. Horizontal lines represent the ionisation energies of the collision gases used in the experiments.

The ionisation energies for the collision gases used are shown in the table below:

| collision gas | ionisation energy /V |
|---|---|
| He | 24.59 |
| Ar | 15.75 |
| Xe | 12.1 |
| NO | 9.25 |

The centre-of-mass collision energy exceeded the ionisation energy, when β-lactoglobulin was used as analyte ion and xenon as collision gas, when bovine insulin was used as analyte ion and argon as collision gas and when insulin chain B was used as analyte ion and argon as a collision gas. The centre-of-mass collision energy also exceeded the ionisation energy, when nitric oxide was used as collision gas and bovine insulin as analyte ion and when nitric oxide was used as collision gas and β-lactoglobulin as analyte ion with laboratory frame kinetic energy higher than 5 kV. The intensity of the analyte peak relative to that of the matrix peak was reduced, when xenon and nitric oxide (for nitric oxide at the high end of the kinetic energy range) were used as collision gases for β-lactoglobulin and when argon and nitric oxide were used as collision gases for bovine insulin. The intensity of the analyte peak relative to that of the matrix peak was also reduced, but to a smaller degree when argon was used as collision

gas for insulin chain B. The intensity of the analyte peak relative to that of the matrix peak remained unaffected, when argon was used as collision gas with β-lactoglobulin as analyte ion, when helium was used as collision gas with insulin as analyte ion and when helium was used as collision gas with insulin chain B as analyte ion. In all three cases, the centre-of-mass collision energy was lower than the ionisation energy of the collision gas.

## 5.3 DISCUSSION

Results in accord with our findings have been reported by Russell et al[171] in a tandem mass spectrometry time-of-flight experiment with small peptides. In this experiment, a Kratos MS-50 double-focussing mass spectrometer was used as the first mass spectrometer (MS-I) in the tandem mass spectrometry experiment and a reflectron of 2 m flight path and 0° reflection angle as the second mass spectrometer (MS-II). Neutrals, formed in the region between MS-I and MS-II by metastable ion dissociation and collision-induced dissociation reactions of $[M+H]^+$ ions, were detected by a microchannel plate detector positioned behind the reflectron (detector 1). Ions were detected by a microchannel plate detector (with a 6 mm diameter central hole) positioned at the entrance of the reflectron instrument (detector 2). The signal observed in the neutral-ion correlation experiment is the result of both a neutral fragment and a fragment ion striking the appropriate detector within a specified time interval. A reduction in the signal to noise ratio was observed in the collision-induced dissociation experiment which was attributed to a significant number of uncorrelated neutrals, i.e. neutrals were formed as a result of collision without detectable ions being formed in the same event. It is however, important to bear in mind that

the results of Russell et al concerned peptides ( M~ 1000 Da), whereas the results presented here are for proteins.

Three different explanations could be possibly put forward to interpret the experimental results concerning collisions of proteins. There is a dynamic explanation, where the collision gas immediately breaks a part of the protonated[172,173] analyte molecule forming a small charged fragment and a large neutral fragment, with the charged fragment possessing a higher scattering angle after the collision and as a result remaining inside the collision cell. The essential feature is that three species (the fragments and collision gas) result from collision, so that larger scattering angles are possible. Second, there is a proton transfer explanation where the reaction $[M+H]^+ + A \rightarrow M + [A+H]^+$ takes place and a third possibility is a charge exchange reaction such as $[M+H]^+ + A \rightarrow [M+H]+A^+$ . Charge exchange requires that the centre of mass collision energy exceed the ionisation energy of the target gas. In both of the cases M is the analyte ion and A the collision gas.

According to the dynamic model, where the collision gas induces immediate fragmentation of the protonated analyte molecule forming a small charged fragment and a large neutral fragment, the more massive the collision gas is, the higher the efficiency of breaking a part of the molecule ion. Nitric oxide, when used as collision gas, should not according to the dynamic model, affect the intensity of the β-lactoglobulin molecule ion, because the mass of nitric oxide is smaller than the mass of argon. No difference was observed in the intensity of the β-lactoglobulin molecule ion when argon was used as collision gas, but when nitric oxide was used as collision gas there was a difference

observed in the analyte ion intensity. The nitric oxide was chosen for the above experiment because it offers a lower ionisation energy than argon (ionisation energy of NO is 9.25 eV and that of Ar is 15.75 eV). The nitric oxide experiments showed that there was a reduction in the intensity of the β-lactoglobulin molecule ion signal for high centre of mass collision energies, thus these results are not favourable for the dynamic model.

It is important to consider the time available for the possible processes. In figure 5.3.(1), the velocities of the ions for different accelerating potentials are given indicating that there is a significant difference in the velocities of the lightest (insulin chain B) and the heaviest (β-lactoglobulin) of the ions used in the experiments described in this chapter. The heavier is the ion the slower it travels for a given kinetic energy, thus allowing more time for interaction between the molecule ion and the target gas. The time available for interaction for an interaction length of 10 Å is shown in figure 5.3.(2) for β-lactoglobulin, bovine insulin, insulin chain B and 3-nitrobenzyl alcohol for different kinetic energies. The time for interaction is in the order of $10^{-13}$ to $10^{-14}$ sec for the analyte molecules with the longest time being $1.8 \times 10^{-13}$ sec for β-lactoglobulin at 3060 V accelerating potential and the shortest time $4.7 \times 10^{-14}$ sec for insulin chain B at 8060 V accelerating potential. The time available for interaction for the 3-nitrobenzyl alcohol matrix molecule is $9.9 \times 10^{-15}$ sec for 8060 V accelerating potential and $1.61 \times 10^{-14}$ sec for 3060 V accelerating potential. Proton transfer reactions tend to occur on the order of $10^{-13}$ to $10^{-14}$ sec, whereas charge exchange[174,175] tends to be at the order of $10^{-15}$ to $10^{-16}$ sec. According to these reaction times, proton transfer and charge exchange would both seem to be possible processes.

ion velocities for different kinetic energies
β-lactoglobulin
insulin
insulin chain B
velocity /(ms⁻¹)
25000
20000
15000
10000
5000
3000
4000
5000
6000
7000
8000
9000
energy /eV

Figure 5.3.(1)

interaction time for 10 Å interaction distance
β-lactoglobulin
insulin
insulin chain B
NBA
2.0E-13
1.5E-13
1.0E-13
5.0E-14
0.0E+00
3000
4000
5000
6000
7000
8000
9000
time of interaction / s
energy /eV

Figure 5.3.(2)

In general the proton affinities of the reactant and the product and the kinetic energy available in the centre of mass collision frame define how probable is a proton transfer reaction. Proton affinity order and proton affinity values for aminoacids have been measured by various groups[176,177,178]. **Figure 5.3.(3)** contains the proton affinity order and proton affinity values for aminoacids as were reported by Lias et al[178].

The lower limit of the dissociation energy of $ArH^+$ could be as high as 2.67 eV according to Chupka et al.[179]. Centre of mass collision energies higher than 10 eV should provide sufficient energy for proton transfer from a protein to argon. The centre of mass collision energy in the experiments with β-lactoglobulin and argon as collision gas was higher than 10 eV for ions with laboratory frame kinetic energy higher than 4.5 keV. Results with β-lactoglobulin as analyte and argon as collision gas showed that there was no difference in the intensity of the analyte signal relative to that of the matrix over the kinetic energy range used in the experiment (3060 V to 8060 V). If proton transfer from a protein to the collision gas is the reaction that takes place in the experiments described in this chapter, a reduction in the intensity of the β-lactoglobulin analyte signal might have been expected when argon was used as collision gas and the laboratory frame kinetic energy exceeded 4.5 keV.

In the experiments where β-lactoglobulin was the analyte ion and xenon the collision gas and in those where insulin was used as analyte ion and argon and nitric oxide as collision gases, there was a considerable reduction in the analyte ion peak compared with the analyte ion peak without collision gas. The

| aminoacid | PA(kJ mol$^{-1}$) | PA (eV) |
|---|---|---|
| Gly | 885.3 | 9.17 |
| Cys | 896.6 | 9.29 |
| Ala | 898.7 | 9.31 |
| Glu | 905.8 | 9.39 |
| Asp | 906.7 | 9.40 |
| Ser | 907.1 | 9.40 |
| Val | 909.6 | 9.42 |
| Leu | 912.5 | 9.46 |
| Gln | 913.8 | 9.47 |
| Thr | 914.6 | 9.48 |
| Phe | 914.6 | 9.48 |
| Asn | 919.6 | 9.53 |
| Met | 926.3 | 9.60 |
| Pro | 928.8 | 9.63 |
| Tyr | 930.1 | 9.64 |
| Lys | 963.6 | 9.99 |
| His | 970.3 | 10.06 |
| Ile | * | |
| Trp | * | |
| Arg | * | |

* Proton affinities were not given.

**Figure 5.3.(3)** Proton affinity and proton affinity values for aminoacids as were reported by Lias et al[178].

reduction in the analyte ion peak signal when collision gas is used, compared with the analyte ion peak without collision gas, shows that the charge of some of the ions remained inside the collision cell. The same behaviour occurred with β-lactoglobulin and nitric oxide at kinetic energies higher than 7 kV laboratory frame kinetic energy. In the case of insulin chain B, which is the lightest of the analyte ions used in the above study, there is a reduction in the analyte ion signal compared with the analyte signal without collision gas when argon collision gas is used. In all the experiments described above there is a difference in the intensity of the analyte signal relative to that of the matrix when the centre of mass collision energy exceeds the ionisation energy of the target gas, which would support the proposal of charge exchange taking place between the target gas and the analyte ion. In figure 5.3.(4) two spectra of β-lactoglobulin with 3-nitrobenzyl alcohol matrix are shown, one without collision gas and the other with xenon collision gas at $4.7 \times 10^{-5}$ mbar collision cell pressure. The peak intensity of the 3-nitrobenzyl alcohol matrix molecule showed no reduction when collision gas was used, indicating that a charge transfer process between the matrix and the collision gas either did not take place or occurred to a much lesser extent. Two spectra of β-lactoglobulin with 3-nitrobenzyl alcohol matrix are shown in figure 5.3.(5), one without collision gas and the other with argon collision gas at $4.7 \times 10^{-5}$ mbar collision cell pressure. The peak of the 3-nitrobenzyl alcohol matrix showed also no reduction when argon collision gas was used, indicating that a charge transfer process between the matrix and the collision gas did not take place. The interaction time of 3-nitrobenzyl alcohol for an interaction distance of 10 Å and for kinetic energies ranging from 3 to 8 kV is shorter than the interaction time for the massive analyte molecules.

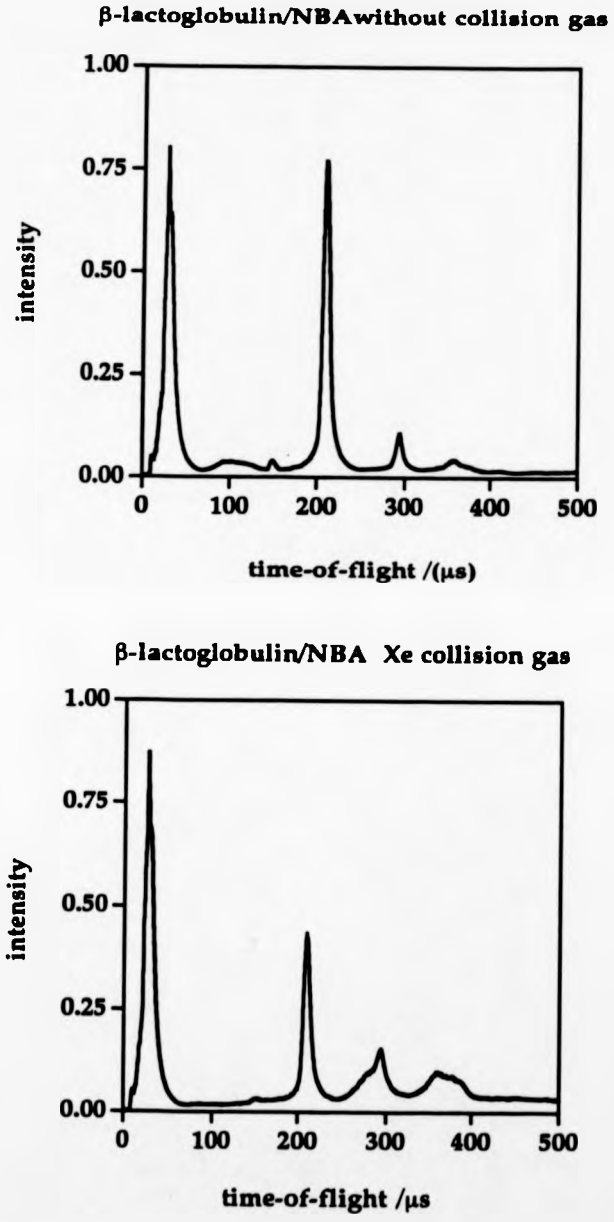
β-lactoglobulin/NBAwithout collision gas
1.00
0.75
0.50
0.25
0.00
intensity
0
100
200
300
400
500
time-of-flight /(μs)
β-lactoglobulin/NBA Xe collision gas
1.00
0.75
0.50
0.25
0.00
intensity
0
100
200
300
400
500
time-of-flight /μs

**Figure 5.3.(4)**

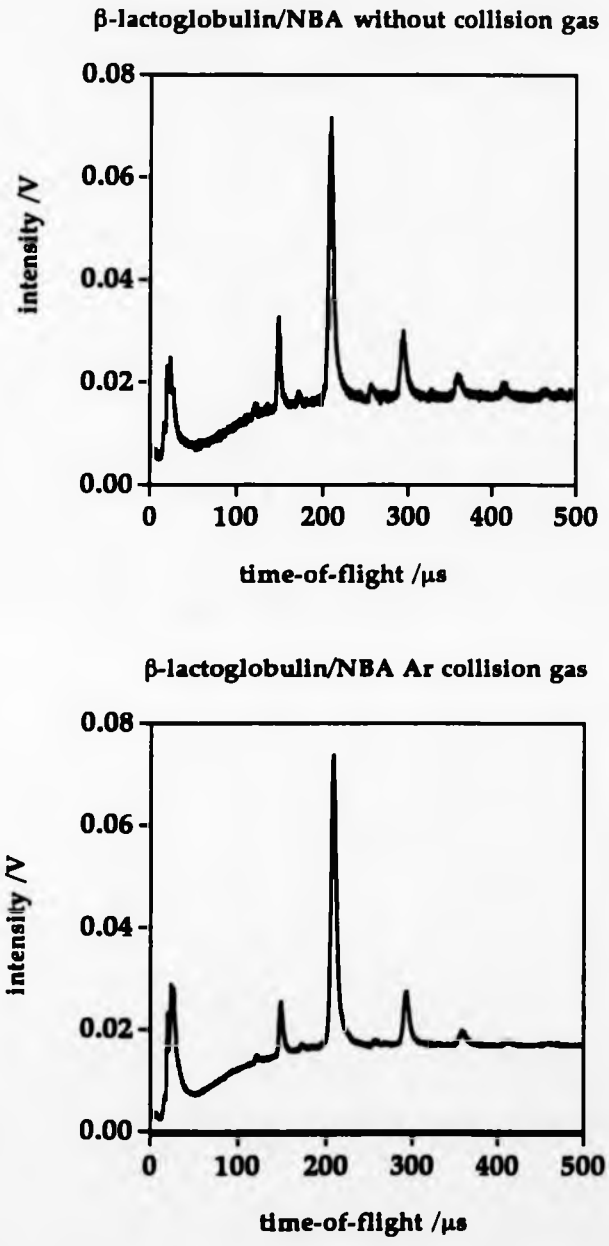
β-lactoglobulin/NBA without collision gas
intensity /V
0.08
0.06
0.04
0.02
0.00
0
100
200
300
400
500
time-of-flight /μs
β-lactoglobulin/NBA Ar collision gas
intensity /V
0.08
0.06
0.04
0.02
0.00
0
100
200
300
400
500
time-of-flight /μs

**Figure 5.3.(5)**

From the experimental results described above, charge exchange between the target gas and the analyte ion is considered to be the most probable explanations for the diminution of analyte ion signals on collision with certain gases. What is not clear is why charge exchange would occur with analyte ions but not with the matrix ions. The interaction times are longer in the case of the analyte ions, and conceivably the proposed presumably endoergic charge exchange is favoured by large interaction times.

# CHAPTER 6

## CONCLUSIONS

During this study, it has been shown that in matrix-assisted laser desorption/ionisation of proteins a substantial number of ions decay after acceleration and prior to detection. The energy-resolved time-of-flight spectra show that there is a source of peak broadening in time-of-flight instruments resulting from the lack of stability of high-mass ions during their flight through the instrument. Two factors may contribute to some extent to the observed fragmentation: (a) high internal energy of protein ions formed by MALDI with the more massive ions possessing higher energies, (b) collisional activation of the massive ions by the background gases.

When collision gas is used, the kinetic energy broadening in the time-selected energy-resolved (TSER) spectrum of the molecule ion increases compared with the time-selected energy resolved-spectrum of the molecule ion in the absence of the collision gas, indicating that fragmentation of the molecule ion occurs as a result of the collision with the target gas. Metastable decay[180,181] and collision-induced dissociation could be the bases of possibly very important methods for structural analysis of biopolymers, which do not show useful fragmentation in normal MALDI mass spectra. Collision-induced dissociation of very large multiply charged proteins (bovine albumin 66300 Da) has been shown to be effective in electrospray[182] ionisation mass spectrometry and spontaneous

slow fragmentation of singly charged proteins following plasma desorption[183,184] is well characterised.

Collision experiments, with different molecular-mass proteins (3496 Da to 18300 Da) and different collision gases, showed a decrease in the analyte signal with respect to the matrix signal for specific collision gases and collision energies. The ions were collected with an off-axis post-acceleration detector. The decrease in the analyte signal with respect to the matrix signal is interpreted as loss of the charge possessed by the protein ions before the collision. The interaction times could be as long as $10^{-14}$ seconds. The results suggest that charge exchange occurs between the collision gas and the analyte ion, leaving the analyte as a neutral after the collision. In a reaction scheme such as the following:

$$[M+H]^+ + A \rightarrow M + H^+ + A \rightarrow M + H + A^+$$

an energy equal to the proton affinity of the analyte is required for the first step and an energy equal to the difference of ionisation energies of H and the target gas is required for the next step of the reaction. The proton affinity of the analyte is in the order of 10 eV and the ionisation energy of H is 13.6 eV. By having the proton affinity of the analyte and the ionisation energy of H the same for different molecular mass analyte ions the whole process depends on the ionisation energy of the target gas and the centre of mass kinetic energy of the analyte ion.

The observed fragmentation of high mass proteins formed by MALDI, with the more massive ones undergoing greater fragmentation than the smaller ones, could be explained in the following way. Massive proteins possess a higher number of degrees of freedom than the less massive ones, thus being able to accumulate more internal energy than the smaller proteins. The very long time (up to 1000 μs) available for ion decay in the time-of-flight experiments

presumably also plays an important role in the fragmentation of the large molecules, by allowing enough time for energy redistribution. Internal energy could be acquired during the desorption/ionisation as thermal energy, by absorption of photons or through collisions of the analyte ions with the matrix-derived particles during the initial plume expansion. When collision gas was used, further fragmentation was observed. Even with helium collision gas, there was some fragmentation of the bovine insulin molecule ion. Neumann et al[163] with field desorption experiments, suggested that at masses higher than that of bombesin (1620 Da) the internal energy taken up by an ion in a collision with helium would fall as the collision energy dropped. According to the above argument, little or no fragmentation might be expected when helium is used as collision gas with bovine insulin. Metastable decay is not usually observed in field desorption experiments, while in matrix-assisted laser/desorption ionisation metastable fragmentation of large proteins was observed indicating that the protein ions produced by MALDI can already possess high internal energy. The explanation put forward for the observed fragmentation of the protein ions after collision with the target gas is that these collisions add a little energy to already highly excited ions, there by causing fragmentation.

Knowledge concerning the construction of energy-resolved time-of-flight mass spectrometers has been gained. Examining the effect of electrostatic analysers on the times-of-flight of ions through energy-resolved time-of-flight mass spectrometers, it was shown that small energy spreads in the ion packet do not affect seriously the time-of-flight. On the other hand, the initial angle of an ion upon entering the electrostatic sector affects considerably the times-of-flight of the ion. Ions of a particular mass and energy following trajectories of different

initial angles suffer differences in time-of-flight, which are sufficient to reduce dramatically the time resolution of the energy-resolved time-of-flight instrument. An overriding objective in energy-resolved time-of-flight mass spectrometry should therefore be to design the ion source so as to provide ion beams with little angular dispersion. During this study, a solution of two electrostatic analysers in a C shape-configuration has been proposed, and investigated theoretically. With this configuration, initial angular divergence of the ion packet would not limit the time-resolution, thus permitting the use of wider angles of entrance and consequently increased ion transmission.

An attempt was made to produce a practical on-axis post acceleration detector which would not require the electron multiplier to be "floated", through the use of a series of low- and high-transmission grids. The detector was not effective, in as much as multiple peaks were obtained for single-mass ions striking the surface of the low transmission grids. This experience does illustrate how great care needs to be taken in the design of ion sources, detectors and reflectrons, because fragment ions may result from combinations of high accelerating potentials and grids. A new on-axis post-acceleration detector, in which the electron multiplier floated at 30 kV, was designed for the energy-resolved time-of-flight mass spectrometer, in order to improve time resolution. Ion detectors for time-of-flight mass spectrometry of high-mass molecules require fast responses (pulse width of one nanosecond or better and rise time of less than one nanosecond) and post-acceleration regions, which are short compared with the total flight path of the ions, in order to ensure that the time spread during ion detection is kept to a minimum.

The design of an ion source of the energy-resolved time-of-flight mass spectrometer has been another consideration. A laser desorption ion source,

which gives a well-collimated beam in the vertical plane of the energy-resolved time-of-flight instrument and focusing in the horizontal plane to ensure high transmission through the electrostatic analyser, was designed and constructed. The study of the effect of the electrostatic analyser on the times-of-flight of the ions in energy-resolved time-of-flight mass spectrometry showed that the resolution of the instrument would increase, if a system of lenses were used before the entrance slits of the electrostatic analyser in order to collimate the ion beam in the horizontal plane. The combination of the lens system of the ion source and the lens system before the entrance slits would act as a telescope, producing after the entrance slits of the electrostatic analyser a narrow collimated beam in the horizontal and vertical plane and thus ensuring high transmission and improved resolution. The lens system before the entrance slits of the electrostatic analyser would not be necessary when the two-electric sector system in C configuration proposed in chapter 2, was used.

Total ion kinetic energy time-of-flight mass spectra from liquid 3-nitrobenzyl alcohol/ protein samples showed that there are energy spreads of kilo-electronvolts in matrix-assisted laser desorption/ionisation mass spectrometry when there is a strong field above the target. When the field was reduced to zero by placing a grid 2 mm above the target at the same potential as the target, these energy spreads were reduced to some electron volts. The broad energy spreads were explained as being predominantly energy deficits arising from the combination of the high electrostatic field, the liquid nature of the matrix/analyte sample and the inherent characteristics of the desorption / ionisation process. The success in producing ions under zero-field conditions does shows that the desorption/ionisation process in MALDI does not require an

electrostatic field above the target and that the ions are not simply drawn out of the matrix/analyte mixture by electrostatic fields above the target.

The liquid matrix 3-nitrobenzyl alcohol was shown to provide good shot-to-shot reproducibility within the same loading and within different sample loadings from the same solution. The sample-loading procedure adopted was to take 1 μl from a solution of 0.5 ml of analyte solution mixed with 0.5 ml of 3-nitrobenzyl alcohol and to remove solvent under a strong stream of nitrogen gas.

1 H. Staudinger and J. Fritschi, *Helv. Chim. Acta.*, **5**, 785 (1922).

2 J. B. Sumner, *J. Biolog. Chem.*, **69**, 435 (1926).

3 J. H. Northrop, *J. Gen. Physiol.*, **13**, 739 (1930).

4 M. S. B. Munson and F. H. Field, *J. Am. Chem. Soc.*, **88**, 2621 (1966).

5 M. S. B. Munson, *Anal. Chem.*, **49**, 722A (1977).

6 M. G. Ingram and R. J. Gomer, *J. Chem. Phys.*, **22**, 1279 (1954).

7 P. L. Robert and H. R. Schulten, *Anal. Chem.*, **61**, 61 (1989).

8 R. G. Bray, R. M. Hochstrassee and J. E. Wessel, *Chem. Phys. Lett.*, **27**, 167 (1974).

9 E. W. Schlag and H. J. Neusser, *Am. Chem. Soc.*, **16**, 16 (1983).

10 H. D. Beckey, *Int. J. Mass Spectrom. Ion Phys.*, **2**, 500 (1969).

11 L. Prokai(ed.), Field Desorption Mass Spectrometry, Marcel Dekker, New York (1990).

12 M. L. Vestal, *Int. J. Mass Spectrom. Ion Phys.*, **46**, 193 (1983).

13 K. L. Busch and R. G. Cooks, *Science*, **218**, 247 (1982).

14 F. Lafortune, R. Beavis, X. Tang, G. Stanging and B. T. Chait, *Rapid Comm. Mass Spectrom.*, **1**, 114 (1987).

15 M. Barber, R. S. Bordoli, G. J. Elliot, R. D. Sedgwick and A. N. Tyler, *J. Chem. Soc. Chem. Commun.*, **7**, 325 (1981).

16 C. J. McNeal and R. D. Macfarlane, *J. Am. Chem. Soc.*, **103**, 1609 (1981).

17 M. Barber, R. S. Bordoli, G. J. Elliot, R. D. Sedgwick and A. N. Tyler, *Anal. Chem.*, **54**, 645A (1982).

18 M. Barber, R. S. Bordoli, G. J. Elliot, R. D. Sedgwick, A. N. Tyler, B. N. Green, V. C. Parr and J. L. Gower, *Biomedical Mass Spectrom.*, **9**, 11 (1982).

19 R. D. Macfarlane and D. F. Torgerson, *Science*, **191**, 920 (1976).

20 C. J. MacNeal, *Anal. Chem.*, **54**, 43A (1982).

21 M. Yamashita and J. B. Fenn, *J. Phys. Chem.*, **88**, 4451 (1984).

22 J. Fenn, M. Mann, C. K. Meng and S. F. Wong, *Mass Spectrom. Rev.*, **9**, 37 (1990).

23 M. Karas and F. Hillenkamp, A. Benninghoven (ed.) Ion Formation from Organic Solids, Springer series in Chemical Physics., 25, Springer-Verlag New York (1983).

24 M. A. Posthumus, P. G. Kistemaker, H. L. C. Meuzelaar, M. C. Ten Noever de Brauw, *Anal. Chem.*, **50**, 985 (1978).

25 D. F. Hunt in F. W. McLafferty Ed.,"Tandem Mass Spectrometry", John Willey & Sons (1983).

26 R.D. Macfarlane in H. R. Morris, Ed., "Soft Ionisation Biological Mass Spectrometry",Heyden: London (1981) pp 110-119.

27 M. Dole, L. L. Mach, R. L. Hines, R. C. Mobley, L. P. Ferguson and M. B. Alice, *J. Chem. Phys.* ,**49**, 2240 (1968).

28 R. D. Smith, J. A. Loo, C. G. Edmonds, C. J. Barinaga and H. R. Udseth, *Anal. Chem.* **62**, 882 (1990).

29 E. C. Huang, T. Wachs, J. J. Conboy and J. D. Henion, *Anal. Chem.*, **62**, 713A (1990).

30 M. Mann, *Org. Mass Spec.*, **25**, 575 (1990).

31 J. V. Iribarne and B. A. Thomson, *J. Chem. Phys* ., **64** , 2287 (1976).

32 J. W. S. Rayleigh, *Philos. Mag* ., **14**, 184 (1882).

33 G. Schemelzeisen-Redeker, L. Butering and F. W. Rollgen, *Int. J. Mass Spectrom. Ion Proc* ., **90**, 139 (1989).

34 J. B. Fenn, M. Mann, C. K. Meng, S. F. Wong and C. M. Whitehouse, *Mass Spectrom. Rev .*, **9**. 37 (1990).

35 P. M. Johnston, M. R. Bergman and D. Zakheim, *J. Chem. Phys .*, **62**, 2500 (1975).

36 P. Esherick, J. A. Armstrong, R. W. Dreyfus and J. J. Wyne, *Phys. Rev. Lett .*, **36**, 1296 (1976).

37 K. Tanaka, H. Waki, Y. Ido, S. Akita, Y. Yoshida and T. Yoshida, *Rapid Commun. Mass Spectrom .*, **2**, 151 (1988).

38 M. Karas, D. Bachmann and F. Hillenkamp, *Anal. Chem .*, **57**, 2935 (1985).

39 M. Karas, D. Bachmann, U. Bahr and F. Hillenkamp, *Int. J. Mass Spectrom. Ion Processes* , **78**, 53 (1987).

40 M. Karas and F. Hillenkamp, *Anal. Chem .*, **60**, 2299 (1988).

41 R. C Beavis and B. T. Chait, *Rapid. Commun. Mass Spectrom .*, **92**, 231 (1989).

42 M. Karas, A. Ingendoh, U. Bahr and F. Hillenkamp, *Biomed. Envir. Mass Spectrom .*, **18**, 841 (1989).

43 F. Hillenkamp, M. Karas, A. Ingendoh and B. Stahl; in A. L. Burlingame and J. A. McCloskey (Eds.), Biological Mass Spectrometry, Elsvier, Amstrdam, **49** (1990).

44 R. C. Beavis and B. T. Chait, *Rapid. Commun. Mass Spectrom .*, **3**, 233 (1989).

45 T-W. D. Chan, A. W. Colburn and P. J. Derrick, *Org. Mass Spectrom .*, **26**, 342 (1991).

46 T-W. D. Chan, A. W. Colburn and P. J. Derrick, *Org. Mass Spectrom .*, **27**, 188 (1992).

47 K. Strupat, M. Karas and F. Hillenkamp, *Int. J. Mass Spectrom. Ion Processes*, **111**, 89 (1991).

48 P. Juhasz and K. Biemann, *Proceedings of the 40th ASMS Conference on Mass Spectrometry and Allied Topics*, Washington, DC, May 31-June 5, 53 (1992).

49 R. C. Beavis, *Org. Mass Spectrom .*, **27**, 653 (1992).

50 R. C. Beavis and B. T. Chait, *Rapid Commun. Mass Spectrom .*, **3**, 432 (1989).

51 B. Stahl, M. Steup, M. Karas and F. Hillenkamp, *Anal. Chem .*, **63**, 1463 (1991).

52 H. Egge, J. Peter-Katalinic, M. Karas and B. Stahl, *Pure Appl.Chem .*, **63**, 491 (1991).

53 P. Juhasz, I. A. Papayannopoulos, C-H.Zeng, V. Papov and K. Biemann, *Proceedings of the 40th ASMS Conference on Mass Spectrometry and Allied Topics*, Washington, DC, May 31-June 5, 1913 (1992).

54 A. Overberg, M. Karas U. Bahr, R. Kaufmann and F. Hillenkamp, *Rapid Commun. Mass Spectrom .*, **4**, 293 (1990).

55 A. Overberg, M. Karas and F. Hillenkamp, *Rapid Commun. Mass Spectrom.*, **5**, 128 (1991).

56 M. Karas, F. Hillenkamp, R. C. Beavis and B. T. Chait, *Anal. Chem.*, **63**, 1193a (1991).

57 R. C. Beavis, T. Chaudhary and B. T. Chait, *Org. Mass Spectrom .*, **27**, 156 (1992).

58 S.J. Doktycz, P. J. Savickas and D. A. Krueger, *Rapid Commun. Mass Spectrom.*, **5** , 145 (1991).

59 M. Karas, E. Nordhoff, B. Stahl, K. Stupat and F. Hillenkamp, *Proceedings of the 40th ASMS Conference on Mass Spectrometry and Allied Topics*, Washington, DC, May 13-June 5, 368 (1992).

60 D. S. Cornett, M. A. Duncan and I. J. Amster, *Org. Mass Spectrom .*, **27**, 831 (1992).

61 H. E. Duckworth and S. N. Ghoshal in C. A. McDowell Ed., " Mass Spectrometry", Mc Graw-Hill Book Company Inc. (1963).

62 R. T. McIver, Jr and W. D. Bowers in F. W. McLafferty Ed.,"Tandem Mass Spectrometry", John Willey & Sons (1983).

63 M. B. Comisarow and A. G. Marshall, *Chem. Phys. Lett .*, **25**, 282 (1974)

64 A. G. Marshall, B. M. Comisarow and G. Parison, *J. Chem. Phys .*, **71**, 4434 (1979).

65 T. A. Lehman and M. M. Bursey, "Ion Cyclotron Resonance Spectrometry", John Wiley: New York (1976)

66 W. Paul H. Reinhard and V. von Zahn, *Z. Physik* , **156**, 1 (1959)

67 R. D. Macfarlane and D. F. Torgerson, *Science* , **191**, 920 (1976).

68 W. C. Wiley and I. H. McLaren, *Rev. Sci. Instrum .*, **26**, 1150 (1955,).

69 J. L. Franklin, P. M. Hierl and D. A. Whan, *J. Chem. Phys .*, **47**, 3148 (1967).

70 J. A. Browder, R. L. Miller, W. A. Thomas and G. Sanzone, *Int. J. Mass Spectrom. Ion Phys.*, **37**, 99 (1981).

71 G. R. Kinsel and M. V. Johnston, *Int. J. Mass Spectrom. Ion Processes*, **91**, 157 (1989).

72 G. R. Kinsel, C. D. Mowry, P. J. McKeown and M. V. Johnton, *Int. J. Mass Spectrom. Ion Processes* , **104**, 35 (1991).

73 W. P. Poschenrieder, *Int. J. Mass Spectrom. Ion Phys .*, **6**, 413 (1971).

74 W. P. Poschenrieder, *Int. J. Mass Spectrom. Ion Phys .*, **9**, 357 (1972).

75 E. W. Muller and S. V. Krishnaswamy, *Rev. Sci. Instrum .*, **45**, 1053 (1974).

76 B. A. Mamyrin, V. I. Karataev, D. V. Shmikk and V. A. Zagulin, *Sov. Phys . -JETP* (Engl. Transl.), **37**, 45 (1973).

77 R. B. Boesl, H. J. Neusser, R. Weinkauf and E. W. Schlag, *J. Phys. Chem.*, **86**, 4857 (1982).

78 W. Gohl, R. Kutscher, H.-J. Laue and H. Wollnik, *Int. J. Mass Spectrom. Ion Phys .*, **48** , 411 (1983).

79 R. Grix, U. Gruner, G. Li, H. Stroh and H. Wollnik, *Int. J. Mass Spectrom. Ion Proc .*, **93**, 323 (1989).

80 H. Wollnik, *Mass Spectrom. Rev.*, **12**, 89 (1993).

81 R. C. Beavis and B. T. Chait, *Chem. Phys. Lett .*, **81**, 479 (1991).

82 R. C. Beavis and B. T. Chait, *Rapid. Commun. Mass Spectrom .*, **3**, 432 (1989).

83 B. Spengler, D. Kirsch, R. Kaufmann, M. Karas, F. Hillenkamp and U. Giessmann, *Rapid Commun. Mass Spectrom .*, **4**, 301 (1990).

84 R. Kaufmann, D. Kirsch, H-A Rood and B. Spengler, *Rapid Commun. Mass Spectrom .*, **6**, 98 (1992).

85 E. Lindholm in J. L. Franklin, Ed., "Ion-Molecule Reactions", Plenum Press: New York (1972) p 457.

86 D. L. Smith and J. H. Futrell, *Int. J. Mass Spectrom. Ion Phys .*, **14**, 171 (1974).

87 R. B. Bernstein and R. D. Levine, " Molecular Reaction Dynamics", Clarendon Press: Oxford (1974).

88 K.R. Jennings and R. S. Mason in F. W. McLafferty Ed.,"Tandem Mass Spectrometry", John Wiley & Sons (1983).

89 G. M. Neumann and P. J. Derrick, *Org. Mass Spectrom.*,**19**, 165, (1984).

90 M. M. Sheil and P. J. Derrick, *Org. Mass Spectrom.*,**23** ,429 (1988).

91 C. D. Bradley and P. J. Derrick, *Org. Mass Spectrom.*, **26**,395 (1991).

92 M. L. Gross and D. H. Russell in F. W. McLafferty Ed.,"Tandem Mass Spectrometry", John Wiley & Sons (1983).

93 F. H. Strobel, L. M. Preston, K. S. Washburn and D. H. Russell, Anal. Chem. , **64**, 754 (1992).

94 R. Kaufmann, D. Kirsch and B. Spengler, *Int. J. Mass Spectrom. Ion Processes*, 131, 355 (1994).

95 L. J. Waller, T. L. Uhlenbrock, F. H. Strobel and D. H. Russell, *Proceedings of the 39 th ASMS Conference on Mass Spectrometry and Allied Topics*, Nashville, TN, May 19-24, 362 (1991).

96 D. R. Jardine, D. S. Alderdice and P. J. Derrick, *Org. Mass Spectrom .*, 26, 915 (1991).

97 K. Schey, R. G. Cooks, R. Grix and H. Wollnik, *Int. J. Mass Spectrom. Ion Processes .*, 77, 49 (1987).

98 F. A. Lindermann, *Trans. Faraday Soc* . 17, 598 (1922).

99 O. K. Rice and H. C. Ramsperger, *J. Am. Chem. Soc.*, 49, 1616 (1927).

100 L. S. Kassel, *J. Phys. Chem.*, 32, 225 (1928).

101 R. A. Marcus, *J. Chem. Phys.*, 20, 359 (1952).

102 "Unimolecular Reactions", P. J. Robinson and K. A. Holbrook, Wiley-Interscience, Wiley and Sons Ltd,London (1972).

103 D. W. Oxtoby and S. A. Rice, *J. Chem. Phys .*, 65, 1676 (1976).

104 J. Ford, *Adv. Chem. Phys .*, 24, 155 (1973).

105 M. V. Kuzmin and A. A. Stuchebrukhov, *Chem. Phys. Letters* , 119 , 556 (1985).

106 M. V. Kuzmin, I. V. Nemov, A. A. Stuchebruchov, V. N. Bargatashvili and V. S. Letokov, *Chem. Phys .*, 124 , 522 (1986).

107 C. Jaffe and P. Brumer, *J. Chem. Phys* . ,73, 5646 (1980).

108 "Theory of Unimolecular Reactions", N. B. Slater, Cornell University Press, Ithaka, N. Y. (1959).

109 N. B. Slater, *Proc. Roy. Soc. Edinburgh*, 64 , 161 (1955).

110 E. K. Gill and K. J. Laidler, *Proc. Roy. Soc.* (London) , A250, 121 (1959).

111 "Theories of Chemical Reacttion Rates', K. J. Laidler, Mc graw-Hill Book Company, New York (1969).

112 E. W. Schlag, R. D. Levine, *Chem. Phys. Letters* ., **163**, 523 (1989).

113 A. L. Burlingame, D. S. Millington, D. L. Norwood and D. H. Russel, *Anal. Chem* ., **62**, 268R, (1990).

114 R. E. Tacklenburg Jr., L. Sellers-Hann and D. H. Russell, *Int. J. Mass Spectrom. Ion Processes* ., **87**, 111, (1989).

115 H. Wollnik, *Mass Spectrom. Rev.*, **12**, 89, (1993).

116 R. E. Jr.Tecklenburg and D. H. Russell, *Mass Spectrom. Rev* ., **9**, 405, (1990).

117 "Mass Spectrometry", C. A. McDowell editor, Mc Graw-Hill, New York (1963).

118 G.-H Oetjen and W. P. Poschenrieder, *Int. J. Mass Spectrom. Ion Phys* ., **16**, 353 (1975).

119 W. P. Poschenrieder, *Int. J. Mass Spectrom. Ion Phys* ., **9**, 357 (1972).

120 D. E. Rogers, Ph. D thesis, La Trobe University, Victoria, Australia (1980).

121 G. M. Neumann, Ph. D thesis, La Trobe University, Victoria, Australia (1983).

122 R. Herzog, *Z. Phys* ., **97**, 596 (1935).

123 H. Matsuda, *Nucl. Instrum. Methods* , **91**, 637 (1971).

124 H. Matsuda, *Int.J. Mass Spectrom. Ion Phys* ., **22**, 259 (1976).

125 P.G. Cullis, Ph. D thesis, University of New South Wales, Australia (1987).

126 John Fluke Manufacturing Corporation, P. O. Box 43210, Mountlake Terrace, Washington 98043, U.S.A. Model No 415B

127 R. P. Morgan, J. H. Beynon, R. H. Bateman and B. N. Green, *Int. J. Mass Spectrom. Ion Phys .*, **28**, 171 (1978).

128 H. McReynolds and M.Anbar, *Int. J. Mass Spectrom. Ion Phys .*, **24**, 37 (1977).

129 J. H. Beynon, R. G. Cooks and T. Keough, *Int. J. Mass Spectrom. Ion Phys .*, **14**, 437 (1974).

130 P. W. Geno and R. D. Macfarlane, *Int J. Mass Spectrom. Ion Phys .*, **92**, 195 (1989).

131 Spellman High Voltage Electronics Corporation, Plainview, NY 11803

132 Spectron Laser Systems, 21 Paynes Lane Rugby, Warwickshire CV2 2UH.

133 Orazio Svelto, "Principles of lasers", second edition, Plenum Press , London (1982).

134 S. C. Davis, Ph.D thesis, University of South Wales, Australia (1988).

135 NAg, Numerical Algorithms Group, Oxford, OX2 7DE, U.K.

136 K. J. Binns and P. J. Lawrenson, "Analysis and computation of electric and magnetic field programs", 2nd edn., Oxford, Pergamon (1973).

137 P. J. Derrick, PhD thesis, University of London (1969)

138 A. E. Giannakopulos, D. J. Reynolds, T-W. D Chan, A.W. Colburn and P. J. Derrick, *Int. J. Mass Spectrom. Ion Proc .*, **131**, 67 (1994).

139 P. J. O'Connor, George E. Leroi, and J. Allison, *J. Am. Soc. Mass Spectrom .*, **2**, 322 (1991).

140 K. Quian, A. Shukla and J. Futrell, *Anal. Chem .*, **62**, 1547 (1990).

141 "SIMION", D. A. Dahl and J. E. Delmore, Idaho National Engineering Laboratory, EG&G Idaho Inc. , P. O. Box 1625, Idaho Falls, ID 83415. U.S.A

142 "MacSimion", D. C. McGilvery and R. J. S. Morrison, Centre for High Resolution and Opto-electronic Technology, Department of Chemistry, Clayton, Victoria 3168, Australia.

143 Edwards High Vacuum, West Sussex RH102LW, England.

144 B. Spengler, D. Kirsch, R. Kaufmann, M. Karas, F. Hillenkamp and U. Giessmann, Rapid Commun. Mass Spectrom., **4**, 301, (1990).

145 R. Kaufmann, D. Kirsch, H-A Rood and B. Spengler, *Rapid Commun. Mass Spectrom .*, **6**, 98 (1992).

146 J. Martens, W. Ens, K. G. Standing and A. Verentchikov, *Rapid Commun. Mass Spectrom .*, **6**, 147 (1992).

147 Galileo Electro-Optics Corporation, Galileo Park P. O. BOX 550, Sturbridge, MA 01566, Massachusetts, USA.

148 K. Biemann, F. Gapp and J. Seibl, *J. Am. Chem. Soc .*, **81**, 2274 (1959).

149 Tandem Mass Spectrometry, Ed. by F. W. McLafferty, John Wiley & Sons, New York, USA (1983).

150 K. L. Bush, G. L. Glish and S. A. McLuckey, Mass Spectrometry/Mass spectrometry, VCH Publishers, New York, USA (1988).

151 K. Biemann and S. A. Martin, *Mass Spectrom. Rev .*,**6**, 1 (1987).

152 S. J. Gaskell, M. H. Reilly and C. J. Porter, *Rapid. Commun. Mass Spectrom .*, **2**, 142 (1988).

153 A. J. Alexander and R. K. Boyd, *Int. J. Mass Spectrom. Ion. Proc .*, **90**, 189 (1989).

154 D. F. Hunt, J. R. Yates, J. Shabanowitz, S. Winston and C. R. Hauer, *Proc. Natl. Acad. Sci .*, (USA), **83**, 6233 (1986).

155 M. Karas, D. Bachmann and F. Hillenkamp, *Anal. Chem .*, **57**, 2935 (1985).

156 R. C. Beavis and B. T. Chait, *Anal. Chem .*, **62**, 1836 (1990).

157 R. C. Beavis, *Proceedings of the ASMS Conference in Mass Spectrometry and Allied Topics*, Washington, DC, May 31-June 5, 5 (1992).

158 R. C. Beavis and B. T. Chait, *Chem. Phys. Lett.*, **81**, 479 (1991).

159 B. Spengler, D. Kirsch and R. Kaufmann, *J. Phys. Chem .*, **96**, 9678 (1992).

160 X. Tang, W. Ens, F. Mayer and K. G. Standing, J. B. Westmore, *Rapid Com. Mass Spectrom .*, **3**, **12**, 443 (1989).

161 B. Spengler, D. Kirsch and R. Kaufmann, *Rapid Commun. Mass Spectrom .*,**5**, 198 (1991).

162 B. Spengler, D. Kirsch, and R. Kaufmann, *J. Phys. Chem .*, **96**, 9678 (1992).

163 G. M. Neumann, M. M. Sheil and P. J. Derrick, *Z. Naturforsch* , **39a**, 584 (1984).

164 M S. Kim, *Int. J. Mass Spectrom Ion Phys .*, **50**, 189 (1983).

165 "The Kinetic Theory of Gases", L. B. Loeb, Dover Publications, inc., New York (1961).

166 "Lange's Handbook of Chemistry", J. A. Dean, Eleventh EditionMc Graw-Hill Book Company (1973).

167 Edwards High Vacuum, Manor Royal, Crawley, West Sussex, RH10 2LW, England.

168 M. M. Sheil, Ph. D. thesis, University of New South Wales, Australia (1987).

169 Private communication, Dr J. C. Traeger, La Trobe University, Bundoora, Australia (1994).

170 E. Uggerud and P. J. Derrick, *J. Phys. Chem .*, **95**, **3**, 1431 (1991).

171 F. H. Strobel, L. M. Preston, K. S. Washburn, and D. H. Russell, *Anal. Chem .*, **64**, 754 ( 1992).

172 M. E. Simon, L. M. Preston, T. Soluki, M. A. White and D. H. Russell, *Org. Mass Spectrom.*, **27**, 827 (1992).

173 D. S. Cornet, M. A. Duncan and I. J. Amster, *Org. Mass Spectrom.*, **27**, 831 (1992).

174 K. Levsen, "Fundamental Aspects of Organic Mass Spectrometry", Vol. 4, Verlag Chemie, Weinheim, New York (1978).

175 "The Encyclopedia of Spectroscopy", ed. G. L. Clark, Reinhold Publishing Corporation, New York (1960).

176 K. Isa, T. Omote and M. Amaya, *Org. Mass Spectrom .*, **25**, 620 (1990).

177 G. Bojesen, *J. Am. Chem. Soc .*, **109**, 5557 (1987).

178 S. G. Lias, J. F. Liebman and R. D. Levin, *J. Phys. Chem. Ref. Data* , **13**, 695 (1984).

179 W. A. Chupka and M. E. Russell, *J. Chem. Phys .*, **49**, 5426 (1968).

180 S. Della-Negra and Y. Le Beyec, *Anal. Chem .*, **57**, 2035 (1985).

181 R. Kaufmann, B. Spengler and F. Lutzenkirchen, *Rapid, Commun. Mass Spectrom.*, **7**, 902 (1993).

182 J. A. Loo, C. G. Edmonds and R. D. Smith, *Anal. Chem .*, **63**, 2488 (1991).

183 P. Demirev, J. K. Olthoff, C. Fenselau and R. J. Cotter, *Anal. Chem .*, **59**, 1951 (1987).

184 B. T. Chait and F. H. Field, *Int. J. Mass Spectrom. Ion Processes* , **65**, 169 (1985).